Master's thesis

NTNU
Norwegian University of Science and Technology
Faculty of Engineering
Department of Structural Engineering

Jørgen Sørbøl

Performance of perforated aluminium plates subjected to blast loading

Master's thesis in Mechanical Engineering
Supervisor: Vegard Aune, Lars Edvard Blystad Dæhli
June 2020

NTNU
Norwegian University of
Science and Technology

Jørgen Sørbøl

Performance of perforated aluminium plates subjected to blast loading

Master’s thesis in Mechanical Engineering
Supervisor: Vegard Aune, Lars Edvard Blystad Dæhli
June 2020

Norwegian University of Science and Technology
Faculty of Engineering
Department of Structural Engineering

NTNU
Norwegian University of
Science and Technology

Department of Structural Engineering
Faculty of Engineering
NTNU – Norwegian University of Science and Technology

ACCESSIBILITY

Open

MASTER THESIS 2020

SUBJECT AREA: Computational Mechanics	DATE: June 10th 2020	NO. OF PAGES: 67

TITLE:

Performance of perforated aluminium plates subjected to blast loading

Ytelsen til perforerte aluminiumsplater utsatt for eksplosjonslast

BY:

Jørgen Sørbøl

SUMMARY:

This thesis investigates the behavior of thin deformable aluminum plates, with and without perforated holes, exposed to blast loading. The work consists of an extensive experimental investigation on the performance of different perforated configurations, that were either pre-cut or generated by ballistic impacts. Numerical simulations are carried out to investigate to what extent the behavior can be predicted by computational tools. The SIMLab Shock Tube Facility (SSTF) at the Norwegian University of Science and Technology was used to perform experiments in controlled, laboratory environments. The tested plates were made from 2 mm thick AA6082 aluminum tempered to peak strength T6 with a 300 mm x 300 mm blast-exposed area. The perforated configurations consisted of circular holes in varying numbers and spatial distributions. In total four configurations were used with one, three or seven pre-cut holes. The SIMLab Gas Gun was used to generate perforated holes from ballistic impacts with different projectile noses, blunt and ogival, respectively. The purpose of including holes in the plates, pre-cut or from ballistic impact, was to study the influence of holes regarding the plates performance and crack propagation. The experimental results in the SSFT were documented using two high-speed cameras, 3D digital image correlation (3D-DIC), laser scanning of deformed plates, and high-frequency pressure measurements.

A total number of fifteen uniaxial tension tests were conducted to investigate material properties for the aluminum alloy. From these tests, a constitutive relation and failure criterion were calibrated by inverse modelling. This material model was used in the numerical investigations of plates exposed to blast loading.

In total 21 tests were conducted in the shock tube experiments. A preliminary study was carried out to obtain two firing overpressures, one close to the capacity limit and one resulting in failure. The results were very interesting as unique crack patterns developed for each of the four configurations.

The numerical simulations of the plates were all carried out in Abaqus/Explicit. Pure Lagrangian models were established for all configurations, and the blast load was imposed through idealized pressure-time curves obtained from previous work. The numerical simulations were able to reproduce many of the experimental observations. The numerical study provided a deeper understanding of how the plate responded to the blast loading. It was found that cracks initiate in holes closest to the clamped corners, and propagate toward them. If a hole is positioned with equal distance to multiple corners, a crack will form towards each of the corresponding corners. In configurations with multiple holes, the study revealed that localization of stress and plastic strains concentrate between the holes. Consequently, cracks were more frequently observed between the holes. Also, the cracks seemed to form more frequently between the holes which to a greater extent aligned with yield lines produced in square plates exposed to blast loading.

RESPONSIBLE TEACHER: Vegard Aune

SUPERVISOR(S): Vegard Aune and Lars Edvard Blystad Dæhli

CARRIED OUT AT: Department of Structural Engineering, NTNU

Institutt for konstruksjonsteknikk
Fakultet for ingeniørvitenskap
NTNU – Norges teknisk-naturvitenskapelige universitet

TILGJENGELIGHET Åpen

MASTEROPPGAVE 2020

FAGOMRÅDE: Beregningsmekanikk	DATO: 10. juni 2020	ANTALL SIDER: 67

TITTEL:

Ytelse til perforerte aluminiumsplater utsatt for eksplosjonslast

Performance of perforated aluminium plates subjected to blast loading

UTFØRT AV:

Jørgen Sørbøl

SAMMENDRAG:

Hovedmålet med denne oppgave er å undersøke oppførselen til tynne deformerbare aluminiumsplater, med og uten perforerte hull, utsatt for eksplosjonslast. Arbeidet består av en omfattende eksperimentell undersøkelse av ytelsen til forskjellige perforerte konfigurasjoner, som enten ble forhåndsskåret eller generert av beskytning. Numeriske simuleringer ble utført for å undersøke i hvilken grad atferden kan forutses av beregningsverktøy. SIMLab Shock Tube Facility (SSTF) ved Norges teknisk-naturvitenskapelige universitet ble brukt til å utføre alle eksperimenter. Platene var laget av 2 mm tykt AA6082 aluminium og varmebehandlet til graderingen T6 og hadde et lastutsatt område på 300 mm x 300 mm. De perforerte konfigurasjonene besto av sirkulære hull i varierende antall og romlige fordelinger. Totalt ble fire konfigurasjoner brukt med ett, tre eller syv forhåndsskjærte hull. SIMLab Gas Gun ble brukt til å generere perforerte hull gjennom beskytning med stumpe og ogivale prosjektiler. Hensikten med å inkludere hull i platene, forhåndsskåret eller fra beskytning, var å studere virkningen av hull angående platenes ytelse og sprekkpropagering. De eksperimentelle resultatene i SSFT ble dokumentert ved bruk av to høyhastighetskameraer, 3D digital bildekorrelasjon (3D-DIC), laserskanning av deformerte plater og høyfrekvente trykkmålinger

Totalt ble det utført femten strekktester for å undersøke materialegenskapene for aluminiumslegeringen. Fra disse testene ble en materialmodell og bruddkriterium kalibrert gjennom invers modellering. Denne materialmodellen ble brukt i numeriske simuleringer av platene utsatt for eksplosjonslast.

Totalt ble 21 tester utført i sjokkrøreksperimentene. Et forstudie ble utført for å oppnå to overtrykk, en nær platens kapasitets og en som resulterete i kollaps. Resultatene var veldig interessante da unike sprekkmønstre ble utviklet for hver av de fire konfigurasjonene.

De numeriske simuleringene av platene ble alle utført i Abaqus/Explicit. Ikke-kobla modeller ble lagd for alle konfigurasjoner, og eksplosjonslasten ble påført gjennom idealiserte trykk-tidskurver hentet fra tidligere arbeid. De numeriske simuleringene var i stand til å reprodusere mange av de eksperimentelle observasjonene. Den numeriske studien ga en dypere forståelse av hvordan platen reagerte når de ble utsatt for eksplosjonslast. Det viste seg at sprekker initierer i hull nærmest de fastklemte hjørnene og forplanter seg mot dem. Hvis et hull er plassert med lik avstand til flere hjørner, vil det oppstå en sprekk mot hvert av de tilsvarende hjørnene. I konfigurasjoner med flere hull viste studien at lokalisering av stress og plastiske tøyninger konsentrerte seg mellom hullene. Derfor ble det ofte observert sprekker mellom hullene i disse konfigurasjonene. Tilsynelatende virket det som om sprekkene som ble dannet mellom hullene i større grad sammenfalt med flytelinjer produsert i firkantede plater utsatt for eksplosjonslast.

Department of Structural Engineering
FACULTY OF ENGINEERING SCIENCE AND TECHNOLOGY
NTNU – Norwegian University of Science and Technology

MASTER'S THESIS 2020

for

Jørgen Sørbøl

Performance of perforated aluminium plates subjected to blast loading

1. INTRODUCTION

Protection of engineering structures against blast loading has received a lot of attention in recent years. During the last decades, aluminium alloys have become increasingly more attractive for structural applications, particularly due to its relatively high strength to weight ratio. Aluminium is also considered an architectural and environmentally friendly material with potential for cost-effective designs to increase performance through a combination of safety and low weight. Since plated structures are frequently being used in engineering applications, it has become necessary to predict the structural response of such components exposed to blast loading. Moreover, plated structures are often perforated (e.g. for design purposes or by fragments accelerated by the blast and impacting the target plate prior to the blast pressure). This introduces the need to consider the influence of such perforations on the overall performance of plated structures. Computational methods are now available to predict both the loading and structural response in these extreme loading situations, and experimental validation of such methods is necessary in the development of safe and cost-effective protective structures. In this study blast experiments will be performed, and the data will be used for validation and verification of some frequently used computational methods involving blast loading.

2. OBJECTIVES

The main objective of the research project is to determine how perforated aluminium plates behave under blast loading, and to validate to which extent this can be predicted using computational tools. Special focus is placed on the influence of the number and spatial distribution of holes on the performance of the plates.

3. A SHORT DESCRIPTION OF THE RESEARCH PROJECT

The main topics in the research project will be as follows;

1. A comprehensive literature review should be conducted to understand the blast load phenomenon, shock tube facilities, constitutive and failure modeling of aluminium plates exposed to extreme loadings, and explicit finite element methods.
2. The aluminium plates are manufactured from cold-rolled sheets of type AA6082-T6. Material tests will be carried out to obtain the mechanical properties of these materials and used to calibrate relevant constitutive relations.
3. The SIMLab Shock Tube Facility will be used to expose perforated aluminium plates to blast loading, as an alternative to explosive detonations. The experiments will be used to investigate typical dynamic responses and failure modes of perforated plates exposed to blast loading, and to study the influence of pre-formed holes on the pressure build-up in front of the plates.
4. Digital Image Correlation (DIC) and laser scanning will be used to measure the 3D transverse displacement fields of the plates in the shock tube experiments.
5. Non-linear FE numerical simulations of the shock tube experiments will be performed, and the numerical results shall be compared and discussed based on the experimental findings.

Supervisors: Vegard Aune (NTNU), Lars Edvard Blystad Dæhli (NTNU)

The thesis must be written according to current requirements and submitted to the Department of Structural Engineering, NTNU, no later than June 10th, 2020.

NTNU, January 15th, 2020

Vegard Aune

Vegard Aune
Associate Professor

Abstract

This thesis investigates the behavior of thin deformable aluminum plates, with and without perforated holes, exposed to blast loading. The work consists of an extensive experimental investigation on the performance of different perforated configurations, that were either pre-cut or generated by ballistic impacts. Numerical simulations are carried out to investigate to what extent the behavior can be predicted by computational tools. The SIMLab Shock Tube Facility (SSTF) at the Norwegian University of Science and Technology was used to perform experiments in controlled, laboratory environments. The tested plates were made from 2 mm thick AA6082 aluminum tempered to peak strength T6 with a 300 mm x 300 mm blast-exposed area. The perforated configurations consisted of circular holes in varying numbers and spatial distributions. In total four configurations were used with one, three or seven pre-cut holes. The SIMLab Gas Gun was used to generate perforated holes from ballistic impacts with different projectile noses, blunt and ogival, respectively. The purpose of including holes in the plates, pre-cut or from ballistic impact, was to study the influence of holes regarding the plates performance and crack propagation. The experimental results in the SSFT were documented using two high-speed cameras, 3D digital image correlation (3D-DIC), laser scanning of deformed plates, and high-frequency pressure measurements.

A total number of fifteen uniaxial tension tests were conducted to investigate material properties for the aluminum alloy. From these tests, a constitutive relation and failure criterion were calibrated by inverse modelling. This material model was used in the numerical investigations of plates exposed to blast loading.

In total 21 tests were conducted in the shock tube experiments. A preliminary study was carried out to obtain two firing overpressures, one close to the capacity limit and one resulting in failure. The results were very interesting as unique crack patterns developed for each of the four configurations.

The numerical simulations of the plates were all carried out in Abaqus/Explicit. Pure Lagrangian models were established for all configurations, and the blast load was imposed through idealized pressure-time curves obtained from previous work. The numerical simulations were able to reproduce many of the experimental observations. The numerical study provided a deeper understanding of how the plate responded to the blast loading. It was found that cracks initiate in holes closest to the clamped corners, and propagate toward them. If a hole is positioned with equal distance to multiple corners, a crack will form towards each of the corresponding corners. In configurations with multiple holes, the study revealed that localization of stress and plastic strains concentrate between the holes. Consequently, cracks were more frequently observed between the holes. Also, the cracks seemed to form more frequently between the holes which to a greater extent aligned with yield lines produced in square plates exposed to blast loading.

Acknowledgements

This thesis is written in relation to the Center for Advanced Structural Analysis (SFI CASA), housed by the Structural Impact Laboratory (SIMLab) at the Department of Structural Engineering – Norwegian University of Science and Technology (NTNU). SFI CASA is a Center for Research-Based Innovation (SFI), as appointed by the Research Council of Norway. SFI CASA was opened on July 1st, 2015, and has a vision to establish a world-leading center for multi-scale testing, modeling, and simulations of materials and structures for industrial applications. This thesis serves as a continuation of previous work on blast-loaded plates at SIMLab, NTNU.

The topic of blast-loading and protective structures has been subject to several research projects at SIMLab in recent years. I am very grateful to have had the opportunity to work on such an interesting topic. The knowledge and experience obtained from the work have thought me a lot of valuable lessons that I hope to use in my career as an engineer.

I would like to give a special thanks to my supervisors; Associate Professor Vegard Aune and Postdoctoral Researcher Lars Edvard Blystad Dæhli. They were always able to answer my questions and to have weekly meetings. In addition, they really helped my motivation when times were tough during this extraordinary time. Vegard's insight and dedication on the matter of blast loaded structures has been nothing else then inspiring. Lars's insight in material modelling and numerical computational tools has been an invaluable resource to learn from.

I would also like to thank Mr. Trond Auestad for your help during the shock tube and the gas gun experiments.

Lastly, I would like to thank Sigurd Aune, Alex Cao, Philipe Schell, Håkon Johansen, Ingrid Aadnesen, Nora Fjøsne, and Anna Tetzmann for all discussions and weekly meetings.

Contents

1 Introduction

1.1 Motivation

During the past two decades, there has been an increased focus on protective structures and measures in response to the increase in the number of terrorist attacks targeting civilians[1]. In addition to man-made loads, blast loading may occur in accidental events in industrial applications. The top priority for an engineer should be to ensure the structural integrity and the security and safety of the people and critical infrastructure. Plated structures are frequently used in engineering structures and it is, therefore, an interest to investigate the performance of plated structures exposed to blast loading. To see if the structural integrity is maintained and if one can predict how the structure will respond to improve the design against such extreme loading conditions.

Aluminum alloys have become increasingly more attractive for structural applications, particularly due to its relatively high strength to weight ratio. Aluminum is also considered an architectural and environmentally friendly material with the potential for cost-effective designs to increase performance through a combination of safety and low weight. Consequently, aluminum has the potential to be a sustainable material in structural and industrial applications. Aluminum has also received increased attention due to its favorable recycling properties. Since only 5% of the energy required to produce primary aluminum is needed to recycle aluminum waste[2]. Moreover, different types of aluminum alloys and manufacturing methods allow for a huge variety of mechanical properties for different engineering applications. This in combination with architectural design results in plated aluminum structures already being used in urban environments.

Large scale testing of protective structures is rather expensive, and detailed measurements of the dynamic response are quite difficult to produce because of the complexity in these types of tests. Small scale, repeatable and controlled studies are therefore favorable since these allow for a deeper insight on the performance of the structure when exposed to blast loading.

In the event of a close-range explosion, one can imagine that the plated structure can be exposed to perforation due to fragments or projectiles prior to the blast loading. This is expected to reduce the capacity for the protective structure and should be considered when evaluating the capacity of the structure.

Computational methods are now available to predict both the loading and structural response in these extreme loading situations, and experimental validation of such methods is necessary in the development of safe and cost-effective protective structures. In this thesis blast experiments will be performed to obtain more insight into the blast-resistance of perforated plates, and the data will be used for validation and verification of some frequently used computational methods involving blast loading.

1.2 Previous work

In recent years there has been an increased effort to investigate the performance of blast-loaded structures with and without perforated holes. The use of shock tube facilities [3], [4], [5], to produce repeatable and controlled blast waves allows for a better understanding of the structural response under such extreme conditions.

In the research of ductile materials exposed to blast loading, the main focus in the literature has mainly been on steel plates. This is due to steels high strength and history of applications in protective structures. On the other hand, there have been some studies on aluminum plates with pre-made defects. Granum et al. [6] studied the effect of different heat-treated AA6016 aluminum plates with pre-cut slits. This was a continuation of the study done in the master thesis by Stensjøen and Thorgeirsson [7]. The number of slits, placement, and the orientation of the slits were varied and exposed to two different blast intensities. A numerical sensitivity study was also conducted to see if the numerical models were able to reproduce the dynamic response and failure mode of the plates. It was concluded that the number and orientation of pre-cut slits had a significant effect on the failure mode and the capacity of the plate. The ability to reproduce failure and crack initiation was good for most tests, but some deviated from the experimental results.

Other studies of perforated aluminum plates are rather scarce. Some studies like Li et al. [8] test sandwich panels with aluminum foam or aluminum as a ductile intermediate layer exposed to blast loading. To take advantage of the high strength to weight ratio of aluminum.

Rakvåg et al. [9] studied the effect of perforated Docol 600DL steel plates where the perforation was idealized through premade holes in the shapes of slits, diamond, square and circular holes. The applied pressure was produced by a pulse pressure loading facility that allowed for similar pressure to be applied to the different geometries. In addition, a purely uncoupled Lagrangian numerical study was conducted before a fully coupled model was produced to investigate the influence of fluid-structure interaction (FSI) effects. The study concluded that the non-circular perforations produced higher stress concentrations in the plate. The uncoupled model showed in general good agreement with experimental results but failed to give an accurate description of the deflection around pre-formed holes. The fully coupled model showed there was significant spatial variation in the pressure load and how it affected the deflection profile, especially in the vicinity of the holes.

With the establishment of the SIMLab shock tube facility (SSFT) and its ability to create planar shock waves in a safe and controlled environment [3], Granum and Løken [10] investigated the response of 0.8 mm thick Docol 600DL steel plates, with and without holes, exposed to blast loading. The SSFT allowed for higher pressure levels to be reached in the experiments. The study found that there was a significant reduction in capacity for the perforated plates, resulting in crack initiation and complete failure. An extensive numerical study looked into uncoupled and coupled numerical formulations. This showed that FSI effects could be simulated at a higher computational cost compared to a pure Lagrangian formulation.

Another study on 0.8 mm thick Docol 600DL steel plates with and without premade holes was studied by Aune et al. [11]. The experimental work took place in the SSTF. One of the perforated plates fractured and a numerical study was conducted to look at the adaptive mesh refinement (AMR) algorithm in the finite element software EUROPLEXUS. The study showed that a fine mesh was needed to predict the crack propagation. Instead of applying the fine mesh to the entire plate, they applied the AMR algorithm to their model.

The algorithm refines the mesh around critical elements during simulation to better capture crack initiation and propagation in the numerical model. This minimized the eroded mass of the plate when using element erosion and saved 50-70 % of the computational time based on user-specified criterion.

1.3 Objectives and scope

The main objective of this research project is to determine how perforated aluminum plates behave under blast loading, and to validate to which extent this can be predicted using computational tools. Special focus will be placed on 625 mm x 625 mm AA6082-T6 aluminum plates with and without holes exposed to blast loading. All plates have the same thickness of 2 mm. Four different geometries have been chosen with pre-cut holes, where the number of holes and their position varies among the four geometries. The idea behind the perforated plates is to investigate the effect of holes when the plates are exposed to blast loading, in order to obtain more insight into the blast-resistant design of aluminum structures. Six plates will also be exposed to ballistic impact prior to the blast loading, using projectiles with the same diameter as the pre-cut holes. This enables investigations on the effect of damage caused by fragment penetration prior to the blast loading. The SIMLab Gas Gun will be used for the ballistic impact testing and the SSTF will be used to generate blast loading.

A numerical study will be conducted to evaluate the capability to reproduce the experimental observations. A constitutive relation for the aluminum alloy will be calibrated to represent the highly non-linear material behavior. A series of quasi-static tensile tests will be used to calibrate such a model.

This work will involve several aspects of material modelling and impact mechanics. It is, therefore, necessary to limit the scope of this thesis, where the limitations are stated as follows:

- All plates are made of the same batch of aluminum alloy AA6082 tempered to peak strength T6.
- All plates will have the same thickness of 2 mm. This limits the behavior of the plates to membrane-dominated response.
- Quasi-static tensile tests in room temperature allow for the evaluation of yield stress and work hardening properties of the material. Other necessary parameters will be taken from the literature.
- The geometries of the pre-cut holes will be the same in all perforated plates.
- Combined effects of perforation by ballistic impacts and blast loading will be a purely experimental study.
- Numerical simulations will only consider an uncoupled Lagrangian approach. This neglects the possible FSI effects that may influence the response of thin deformable plates exposed to blast loading.

2 Test specimens and theory

This section presents the geometry of the target plates and the test specimens used to identify material parameters in the uniaxial tension test. A presentation of the constitutive relation used in this thesis is also presented.

2.1 Aluminum plates

All 625 mm x 625 mm aluminum plates were produced and delivered by Alnan Aluminium Co. Ltd. The aluminum alloy under consideration is AA6082 tempered to peak strength T6. The choice of material was due to its easy accessibility and frequent use in engineering applications. The chemical composition is given in Table 1. The plates were cold rolled down to the desired thickness of 2 mm.

In Figure 1 the different geometries of the plates are shown. The circular, pre-cut holes at the center of the plates have the same diameter of 20 mm. To calibrate a constitutive relation for the material, one plate was used to cut out fifteen dog bone specimens used for the tensile tests. Three specimens for each orientation 0°, 22.5°, 45°, 67.5° and 90° with respect to the rolling direction were produced. 0° refers to the orientation parallel to the rolled direction.

Table 1 - Chemical composition of aluminum alloy 6082 in this thesis (in weight-%)

Si	Fe	Cu	Mn	Mg	Cr	Zn	Ti	Zr	Ni	Al
1.2	0.22	0.05	0.65	0.7	0.04	0.06	0.02	-	-	Balance

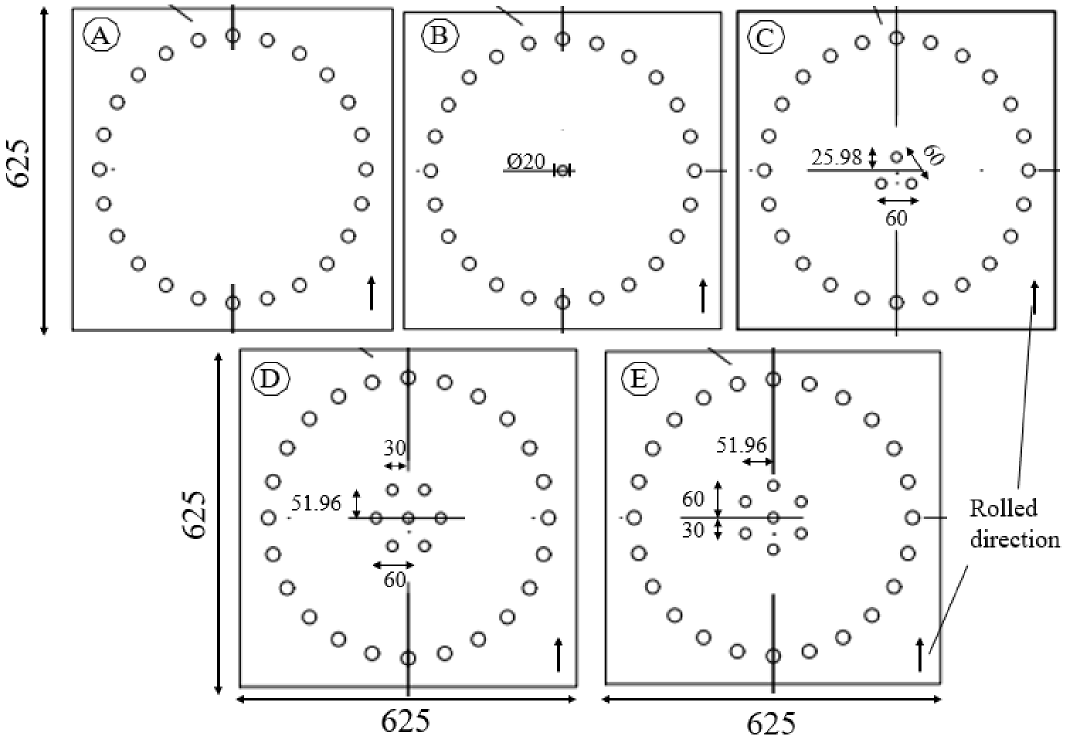

Figure 1 - Geometries of the five plate configurations. a) A full plate with no pre-cut holes. b) A single hole in the center of the plate. c) Three holes placed with the same distance from the center. d) One hole in the center and six holes in a hexagon pattern. e) Same geometry of holes as in d), rotated 90 degrees.

2.2 Constitutive relation

Aluminum exhibits a linear elastic behavior until a certain stress level where the material yields, and irreversible plastic deformations occur beyond this point [12]. The constitutive relation needs to capture this transition and represent the behavior during plastic deformation. For ductile materials, the increase in dislocation density leads to a work hardening during plastic deformation. This is known as isotropic hardening in the literature, resulting in an increase of the elastic domain. For materials that experience rapid loading, the material can experience hardening due to high strain rates and softening due to adiabatic heating where the heat does not have time to dissipate.

A well-established material model that accounts for these phenomena is the modified Johnson-Cook constitutive model [13]. This model will, therefore, be used in this thesis, combined with the von Mises yield criterion and its associated flow rule [12]. The constitutive relation that describes the plastic domain then reads.

$$\sigma_{eq} = \left(\sigma_0 + R(p)\right)\left(1 + \frac{\dot{p}}{\dot{p_0}}\right)^C \left(1 - \left(\frac{T - T_r}{T_m - T_r}\right)^m\right) \tag{1}$$

Here σ_{eq} represent the equivalent stress. The first term describes yield stress that is given by σ_0 and $R(p)$ is the isotropic work hardening variable dependent on the plastic strains p. Second term controls the viscoplastic behavior of the material and contains $\dot{p}$ which is the strain rate and $\dot{p_0}$ which is a user-specified reference strain rate. The variable C defines the rate sensitivity in the material. The third term is described by the absolute temperature T, reference temperature T_r, melting temperature T_m, and m governs the thermal softening.

The work hardening variable $R(p)$ is represented by a three-term Voce hardening rule,

$$R(p) = \sum_{i=1}^{3} R_i(p) = \sum_{i=1}^{3} Q_{Ri}(1 - e^{-c_{Ri}\,p}) \tag{2}$$

where Q_{Ri} and c_{Ri} represent the hardening parameters of each term where all the terms are assumed to be $Q_{Ri}, c_{Ri} > 0$. An alternative representation of the hardening parameters is $\theta_{Ri} = Q_{Ri} \cdot c_{Ri}$. The value of θ_{Ri} is a good illustration of how each term affect the hardening. Large θ_{Ri} indicates that the term reaches the value of Q_{Ri} for low strains. Intermediate values of θ_{Ri} implies that the term comes into effect as the plastic strains develop. While a small value of θ_{Ri} indicate that the term comes into effect for larger plastic strains. A common way to organize the terms is $\theta_{R1} > \theta_{R2} > \theta_{R3}$. The sum of all three terms R_i gives a representation of the total work hardening in the material. The application of Voce hardening is well established for aluminum in blast and impact environments and allows for calibration by a simple uniaxial tensile test.

The strain rate sensitivity of the AA6082 was not examined in this study, but the sensitivity of the AA6xxx series has been extensively examined in the literature. Chen et al. [14] studied two AA6xxx alloys, 6060 and 6082 respectively, tempered to T6 with strain rates up to 1000 s^{-1}. The study showed that the AA6xxx alloys were rather insensitive to the strain rate and the strain rate sensitivity parameter C was calibrated to be 0.0015 and 0.0038, respectively, for the two alloys. Vilamosa et al. [15] also reported a low strain rate sensitivity for three AA6xxx alloys when investigating the combined effect of strain-rates and elevated temperatures. Which substantiates the findings from Chen et al. Based on these results the strain-rate effect was neglected and the parameter C was set to 0. No investigation into thermal effects was conducted in this thesis, but its effects have been studied. Baglo and Dybvik [16] investigated 2 mm thick EN AW-1050-H14 plates subject to blast loading, and conducted a numerical parametric study on the effect of applying adiabatic or isothermal conditions. The study showed there was a negligible difference in the response when including adiabatic effects to the simulation. This finding is substantiated by the work done by Granum et al. [6] on AA6016 plates with pre-cut slits, where the effect of applying isothermal or adiabatic conditions was negligible. From these observations, the decision to apply isothermal conditions was taken, and the parameter governing thermal softening m was set to 0. This reduced Equation 1 to a simplified model for equivalent stress that is applied in the numerical simulations in this thesis, i.e.,

$$\sigma_{eq} = \sigma_0 + R(p) = \sigma_0 + \sum_{i=1}^{3} Q_{Ri}(1 - e^{-C_{Ri}\,p}) \tag{3}$$

The simplified model is then limited to an elastic-plastic material behavior with isotropic hardening. This model is rate-independent and does not consider the softening due to alteration in temperature.

An uncoupled fracture criterion is chosen to evaluate the evolution of damage in the numerical models. The criterion chosen was proposed by Cockcroft and Latham (CL) [17] and is given as.

$$\omega = \frac{W}{W_c} = \frac{1}{W_c}\int_0^p \langle \sigma_I \rangle dp \tag{4}$$

The CL damage criterion varies between $\omega \in [0,1]$, where $\omega = 1$ indicates that the element has reached its critical value of damage. The CL parameter W is obtained by integrating the positive parts of major principle strain σ_I as a function of plastic strain p. The failure criterion W_c can be found through integration by setting the damage parameter $\omega = 1$, such that $W_c = W = \int_0^{p_f} \langle \sigma_I \rangle dp$. The result from a uniaxial tension test gives the boundaries to the integral from zero to failure strain p_f.

There is an underlying assumption in this section that the AA6082-T6 plates can be assumed to be isotropic. For a cold-rolled plate, the orientation of the grains on a microscopic level can lead to a significant anisotropy. To establish a complete anisotropic model is beyond the scope of this thesis and there are numerous examples of literature applying isotropic properties to aluminum that show some anisotropic tendencies [6], [18], [19]. The anisotropy of the material used in this thesis will only be addressed in the presentation of the results for the uniaxial tension tests in Section 3.

3 Material testing and calibration

This section contains the experimental testing and calibration of a material model for the AA6082-T6 aluminum alloy. A total of 15 uniaxial tension tests were conducted with different orientations as described in section 2.1. The results were then processed in MATLAB [20] and the material parameters were calibrated based on this data. From the experiments, the yield stress, hardening, and possible anisotropy in the material were evaluated. A three-term Voce was then calibrated and used to describe the plastic behavior in the numerical model. The calibrated model was used in simulations that verified its predictability. Finally, a Cockcroft-Latham criterion was calibrated for different characteristic mesh sizes.

3.1 Uniaxial tension test

Flat dog bones of the specimen type UT70 were used in the uniaxial tension tests. It has a gauge length of 20 mm and a width of 5 mm. A complete overview of the geometry to the UT70 specimens can be seen in Figure 2. The uniaxial tension tests were carried out in an Instron 5982 100 kN load cell. The axial strain rate was $\dot{\varepsilon} = 5 \cdot 10^{-4}\ s^{-1}$. The displacement field was tracked by a camera and was later processed in a Digital Image Correlation (DIC) software eCorr[21]. All the specimens were sprayed with a speckle pattern to enable tracking of the displacement field. Before every test, the width and thickness were measured at three separate points along the gauge on the UT70 specimens to ensure that the precise geometry would be used when the tests were post-processed.

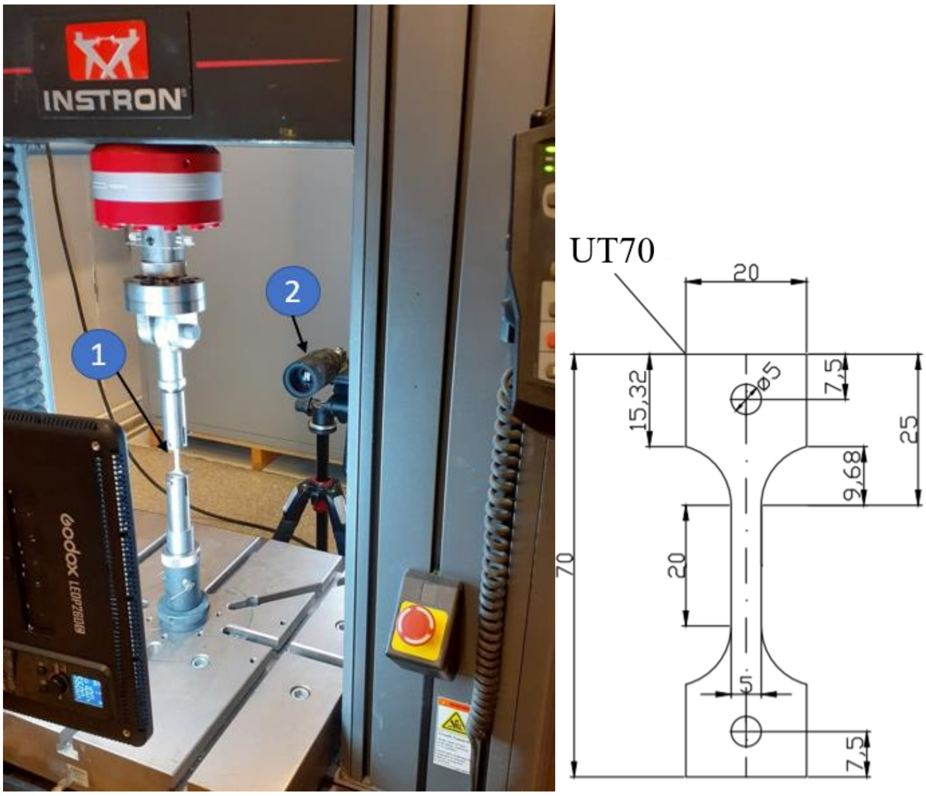

Figure 2 – left) setup for the uniaxial tension experiment. 1 shows a UT70 specimen placed in the test rig. 2 shows the camera used for capturing the displacement field. Right) Shows the geometry of a UT70 specimen. All dimensions are given in mm.

The force applied to each test was extracted directly from the load cell. Post-processing of the displacement field in eCorr was done to avoid any sliding or self-straining measured by the load cell. A horizontal vector was defined to calculate a unique pixel to mm conversion ratio for each specimen, which was then used to establish a virtual extensometer in eCorr. All the data were then exported to MATLAB for post-processing. The setup for the experiment can be seen in Figure 2.

The results from the DIC analyses were extracted and used to obtain engineering stress-strain and true stress-strain curves. The engineering stress and strain quantities were obtained from

$$e_x = \frac{L - L_0}{L_0} = \frac{\Delta L}{L_0} \tag{5}$$

$$s_x = \frac{F}{A_0} \tag{6}$$

Where Equation 5 refers to the engineering strain and Equation 6 refers to engineering stress. Here, L_0 is the initial length of the virtual extensometer, while L is the actual length at any given time through the test. F is the force retrieved from the load cell and A_0 is the reference area from the middle of the gauge section. The true strain and true stress are then calculated from the engineering values via

$$\varepsilon_x = \ln\left(\frac{L}{L_0}\right) = \ln(1 + e_x) \tag{7}$$

$$\sigma_x = \frac{FL}{A_0 L_0} \rightarrow \sigma_x = s_x \frac{L}{L_0} \rightarrow \sigma_x = s_x(1 + e_x) \tag{8}$$

One important thing to note is that the true stress and true strain calculated this way are only valid up to necking of the specimen, since they assume a uniaxial stress state to be present in the specimen. During necking the influence of triaxial stress state invalids the assumption of a uniaxial stress state, such that the true stress-strain calculated this way is only valid up to necking.

To evaluate whether the material exhibits plastic anisotropy the strain ratio can be calculated through

$$R_x = \frac{d\varepsilon_y}{d\varepsilon_z} \tag{9}$$

where $d\varepsilon_y$ and $d\varepsilon_z$ are the strain increments in the width and thickness direction, respectively. For isotropic materials, the strain ratio should be unity, while a ratio different from unity indicates that there is an anisotropy in the material. For a flat specimen, the strains in the width direction can be found similarly to the strains in the longitudinal direction by applying a transversal extensometer over the width of the specimen. However, with a 2D-DIC there is no way to trace the change in the thickness direction.

One possible way to determine the strain in the thickness direction is to assume plastic incompressibility. Bebeshko and Shechenko [22] used this approach for an aluminum alloy D16T and concluded that the assumption of plastic incompressibility was fulfilled. The plastic incompressibility assumes $\varepsilon_v = 0$, which gives the following expression for the strain in thickness direction

$$\varepsilon_z = -(\varepsilon_x + \varepsilon_y) \tag{10}$$

The same method was employed by Tryland et al. [23] when investigating material properties for three different aluminum alloys of AA6082-T6. Where the strength was considerably dependent on the orientation to the extrusion direction for all three alloys. The R-values from their experiments indicated that there was a significant anisotropy, i.e., R not close to unity, in all the three alloys which could explain the difference in strength.

3.2 Experimental data

The stress-strain curves for all the uniaxial tensile tests are shown in Figure 3. Note that one test did not pass the DIC analysis and is therefore not shown. This was due to an error when applying the speckle pattern such that the tracking algorithm in eCorr had problems tracking the displacement field through the entire experiment.

We observe that there is little spread between the different orientations with regards to the stress-strain curves in general. The failure strain shows some spread, but the stress at failure, σ_f, are similar for the different orientations. The results from the uniaxial tension test substantiate the assumption that the material could be approximated as an isotropic material.

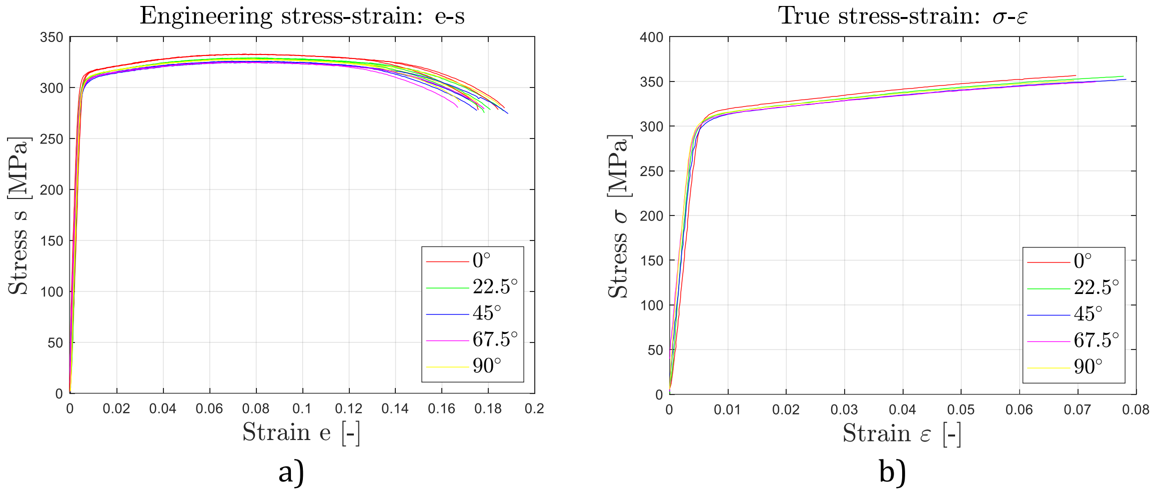

a) b)

Figure 3- a) Shows the engineering stress-strain for the experimental tensile tests. b) shows the true stress-strain curves for all the tests up to necking. All orientations 0° (red), 22.5° (green), 45° (blue), 67.5° (cyan) and 90° (yellow) with respect to the rolled direction.

However, even though the stress level is not significantly affected by the material orientation, the material can still be plastically anisotropic. This would reveal itself through differences in the plastic flow, which is visible to some extent in the stress-strain curves in Figure 3. Consequently, the strain ratios (R-values) are used to evaluate the plastic anisotropy of the material and assess the assumption of isotropic material behavior in the numerical simulations.

A problem arose when trying to evaluate the development of R-values as they are described in incremental form in Equation 9. The reason behind this is assumed to be that the high logging frequency tracking the displacement field was so high that it led to large oscillations in the R-values. To circumvent this problem plastic strains were found in width and thickness direction and plotted against each other on the form $(\varepsilon_y^p, \varepsilon_z^p)$. Plastic strains were found through Equation 11.

$$\varepsilon_i^p = \varepsilon_i^{tot} - \varepsilon_i^{el} \tag{11}$$

The result of this procedure can be seen in Figure 4. The R-values for each orientation are determined by the slope of the curves. Observe that the slope is nearly constant for most of the orientations. Since the scatter in results was negligible within each orientation only one representative test from each orientation were plotted. The slope was evaluated in two ways; (i) by the built-in interpolation tool in MATLAB and (ii) through evaluation of the slope between two points on the curve, indicating the average slope between the two selected points.

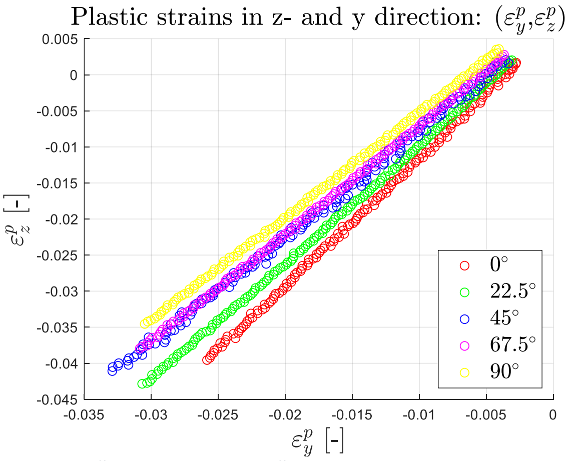

Figure 4 - The plastic strains in width, ε_y^p, and thickness, ε_z^p, direction plotted. A representative test for each orientation is plotted. Orientation 0° (red), 22.5° (green), 45° (blue), 67.5° (cyan) and 90° (yellow) with respect to the rolled direction.

From Table 2 it is apparent that there is some anisotropy in the plastic flow since none of the orientations are close to unity. However, to establish a complete anisotropic model is out of the scope of this thesis, and based on the results in Figure 3 the material will be regarded as isotropic for the rest of this thesis.

Table 2 - R-values for given orientations. Interpolated values from curve fitting and calculated values.

Orientation	R - interpolated [−]	R - calculated [−]
0°	1.777	1.775
22.5°	1.616	1.637
45°	1.448	1.478
67.5°	1.520	1.500
90°	1.459	1.443

3.3 Identification of material parameters

To represent the work hardening of the material a three-term Voce hardening rule, as described in section 2.2, was calibrated. The plastic strain, ε_x^p, and true stresses up to necking was extracted from all tests, and the curve fitting tool in MATLAB was applied to calibrate the terms.

The work hardening model was then calibrated by a trial and error approach. The method consists of using the true stress-strain curve data up to necking and an additional data point which is based on artificial data. The strain for this artificial point was chosen to be at a plastic strain of $\varepsilon^p = 0.5$ and the stress was the true stress at necking multiplied by a scaling term $(1 + X)$, where X is the percentage increase in stress after necking. Illustrated in Equation 12.

$$\sigma_{guess} = \sigma_{necking} \cdot (1 + X\%) \tag{12}$$

The idea is to "shoot" toward the right solution. An illustration of how the guesses look like for a 10%, 20%, and 30% increase is depicted in Figure 5. The work hardening terms Q_i and c_i was calibrated for different values of the scaling term. Finally, each of the calibrated work hardening models were assigned in a numerical simulation and compared to the experimental data, from which the best fit was found by manual inspection. By repeating the procedure a couple of times, one should be able to obtain a suitable fit for the work hardening terms.

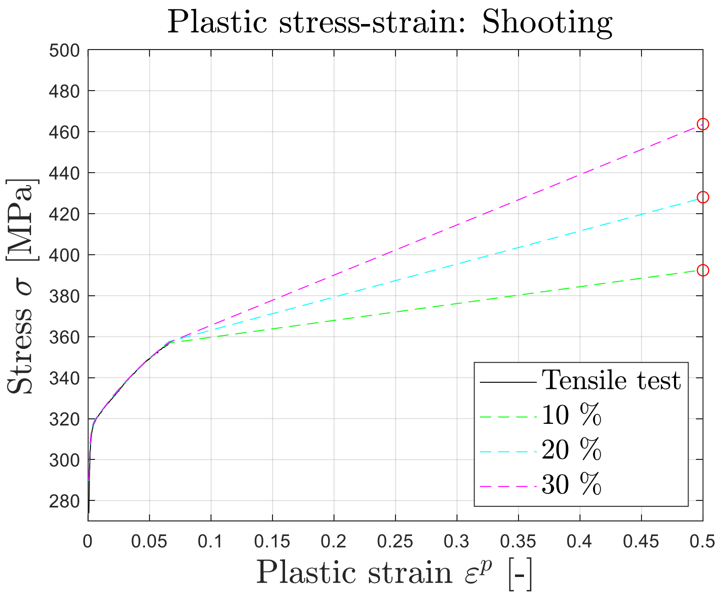

Figure 5 - Illustration of shooting method for inverse modeling. The black curve illustrates the experimental data. While the dotted lines illustrate the shooting toward artificial points illustrated a red circle, with values of 10%, 20%, and 30% increase of stress at necking and strain $\varepsilon^p = 0.5$.

3.3.1 Numerical model

The uniaxial tension tests were simulated in the finite element method program Abaqus/Explicit[23]. Since an isotropic model is employed in this work, we utilize the symmetry of the test specimen to reduce the computational time by modelling only a quarter of the UT70 specimen. A 3D deformable solid was made, and a linear brick element with reduced integration C3D8R was chosen as element type from the Abaqus element library. With element size $L_e = 0.25x0.13$ mm on the symmetry plane in the longitudinal direction where necking occur, and then increasing in size as one moves further away from the longitudinal symmetry plane. Elastic properties for aluminum were taken from literature and are given in Table 3.

Table 3 - Elastic parameters used in the numerical model [6].

E [GPa]	ν [-]	ρ [kg/m^3]
70	0.33	2700

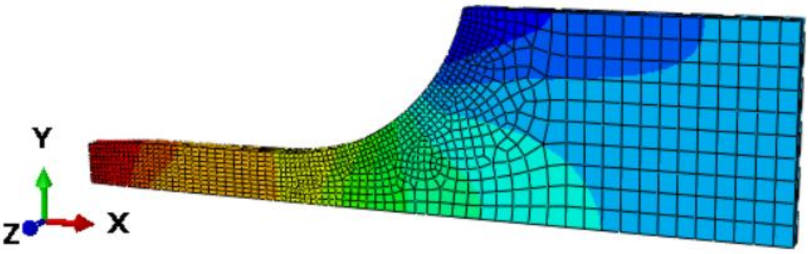

Figure 6 - Abaqus model of a quarter piece of the UT70 specimen used for simulations of the uniaxial tension test. The picture shows the specimen at an arbitrary stress state where the material starts to yield. Red colors indicate an area of large stress.

The plasticity of the material was introduced by a SIMLab metal model through a VUHARD subroutine that allowed an input of the three-term Voce, and a user-specified field to include a CL-criterion to allow damage to develop through element erosion. The load was applied through a dynamic explicit step which included nonlinear effects, as a velocity with the load speed of 150 mm/s at the end of the specimen. To mimic the quasi-static load from the uniaxial tension test over the duration of $t = 0.02\ s$. To avoid that numerically induced stress waves were produced, due to a sudden loading, the load was ramped up at the beginning of the simulation. The time used to ramp up the load was 10% of the total simulation time.

An identical specimen was also created with 3D deformable shell elements. Where the element type chosen was S4R.

3.4 Calibrated terms

The experimental data from the 0° orientation was used as a reference curve to calibrate the work hardening parameters. The spread between the different orientations was almost negligible prior to the onset of necking, but as previously mentioned the fracture strain had some spread that could affect the fit in the post necking domain.

In Figure 7a, the plastic strains and stresses after yielding are plotted for all orientations. The red curve represents the 0° orientation which the Voce model is calibrated against. In Figure 7b the Voce model is calibrated against the experimental data and an artificial point as described in section 3.3. An interesting feature from this figure is how the different terms in the Voce model effects the result. An example is how Q1 rises rapidly and then saturates very quickly, while the Q3 term starts slow and then rises in effect as the plastic strains become larger.

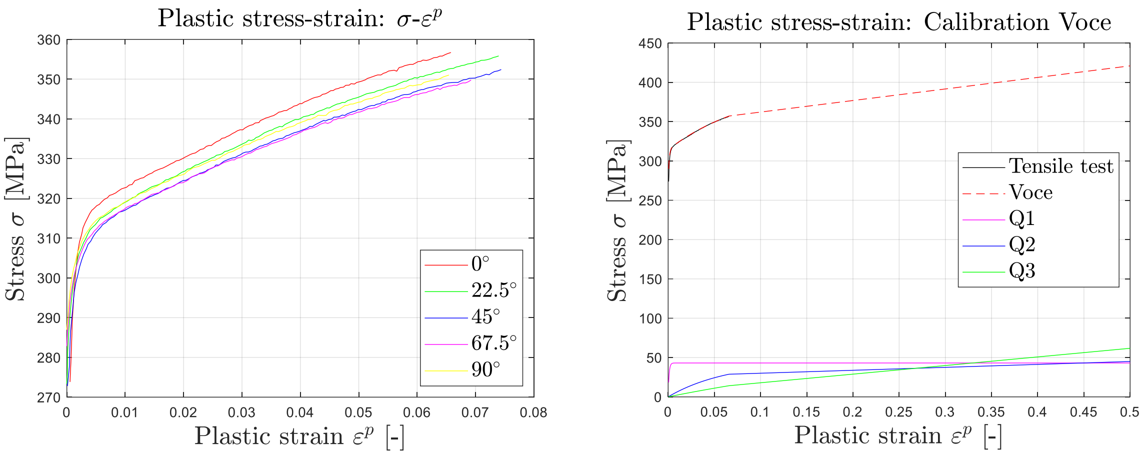

a) b)

Figure 7 - a) Shows the plastic strains and stresses after yielding for all orientations. b) Shows the experimental data (for 0°) plotted from the tensile test (black) and the curve fit for the Voce model (red) as a function of the plastic strains as a result of the shooting method. In addition, to the individual contribution of each term in the model. First-term (magenta), second term (blue), and third term (green).

Figure 8 shows the results from the numerical simulations of the uniaxial tension test with different values for the additional stress-strain point. In Figure 8a the result from the calibrated guesses shown in Figure 5 seems to give a reasonably good fit compared to the experimental data. It became clear that a better fit could be found somewhere in the domain between $X \in [10\%, 20\%]$ and gave motivation to continue the study. Three more iterations were done, and the results can be seen in Figure 8b. From this study, the calibrated terms for the artificial data point with an 18% increase in stress was used in further investigations of the material as it showed to be the best fit. The calibrated terms for the Voce model can be seen in Table 4.

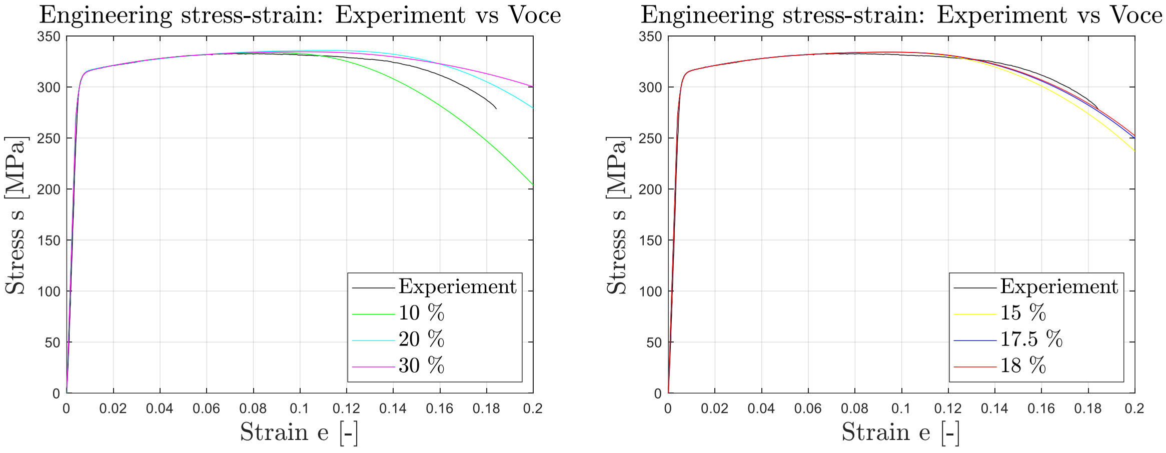

a) b)

Figure 8 - a) shows the result of the uniaxial tensile test for 0° orientation and numerical simulations of the tensile test with calibrated Voce for guesses 10% (green), 20% (cyan) and 30% (magenta). b) Shows the result of the uniaxial tensile test for 0° orientation and numerical simulations of the tensile test with calibrated Voce for guesses 15% (yellow), 17.5% (blue), and 18% (red).

Table 4 - Calibrated terms for the Voce model to represent work hardening.

σ_0 [MPa]	Q_{R1}[MPa]	θ_{R1} [MPa]	Q_{R2} [MPa]	θ_{R2} [MPa]	Q_{R3} [MPa]	θ_{R3} [MPa]
271.10	43.07	43716.00	45.00	697.50	79.90	236.82

3.5 Fracture criterion

After suitable work hardening parameters were found, a fracture criterion had to be added to mimic the fracture observed in the experiment. The fracture criterion chosen was the CL criterion as described in section 2.2. The fracture criterion W_c in the CL criterion is dependent on the characteristic element size in the FE model. Hence, a study of different values for W_c based on characteristic elements sizes was conducted where the size of the solid elements was based on the number of elements through the thickness of the aluminum plate.

Since the average thickness of the all tensile specimens were $t = 2.08$ mm, this thickness was used as the basis for choosing the number of solid elements that was used through the thickness. With the idea of having a full 300 mm x 300 mm plate modeled with the characteristic element size of the thickness over the entire plate, the number of elements over the thickness that were investigated were 2, 3, 4, and 16 elements. For 3 elements over the thickness, a new numerical model had to be made where the full thickness of the specimen was modeled and the symmetry in z-direction had to be discarded.

For the shell model, a problem occurred when trying to calibrate the CL-criterion for shell elements larger than 5 mm, because of the geometry of the UT70 specimen. This was solved by using the calibrated data from another activity, where they used AA6082-T6 and UT200 specimens. Their procedure can be seen in Morin et al. [19], and gave the CL fracture criterion for some characteristic dimensions for shell elements.

The work hardening parameters listed in Table 4 were used in the numerical simulations, while the mesh was edited to have 2, 3, 4, or 16 elements over the thickness where the fracture was expected to occur. Then the engineering stress-strain curves for the simulations were extracted and compared to the experimental data up to the point of fracture. The CL parameter W was monitored up to fracture and the appropriate W_c value could be determined from the value of W in the critical element at the point of fracture in the experiments. The test with 16 elements was done to give a point of reference to what an optimal CL-criterion for solids would be if one were not limited by the number of elements through the thickness in simulations of blast loaded plates.

3.6 Fracture criterion result

The result from the failure criterion study can be observed in Figure 9. The plot shows the development of the CL parameter W for the simulations with different number of elements over the thickness. Also, the engineering stress-strain curve from the chosen uniaxial tension test and the numerical simulation with the best possible Voce fit are presented. It becomes clear from the W-strain curves that the fracture parameter rises rapidly as the strain moves toward the fracture strain. The CL-criterion W_c is then extracted at the fracture strain to the experiment at $e_f = 0.184$, where $W = W_c$. Table 5 shows the values for the different CL criterion based on the number of elements through the thickness.

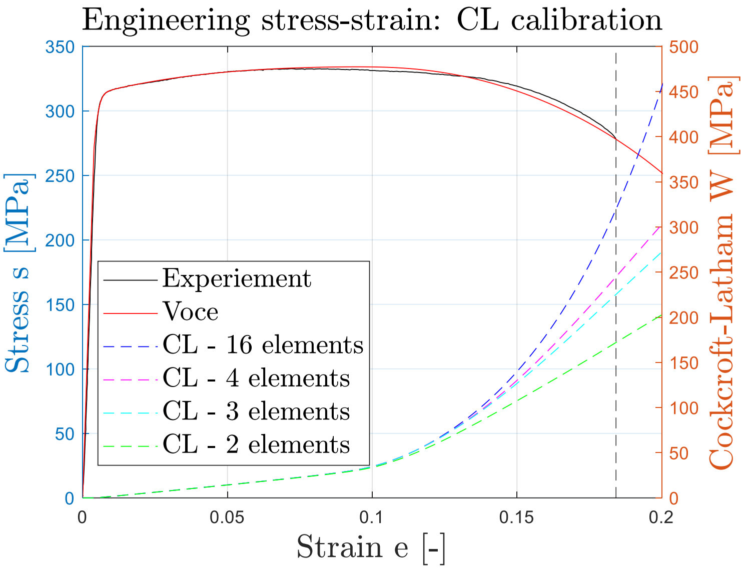

Figure 9 - shows the engineering stress-strain curve of the experiment and the numerical simulation with the calibrated Voce. And the development of W for different number of elements over the thickness. The vertical line indicates the where the value for W_c is extracted from the different simulations.

Table 5 - Number of elements through the thickness of the specimen, their element size, and the corresponding CL criterion.

# of elements	Element size [mm]	W_c [MPa]
2	1.04x1.04	172.203
3	0.69x0.69	225.442
4	0.52x0.52	244.442
16	0.13x0.13	319.943

3.7 Results

Fifteen uniaxial tension tests were conducted, which establish the basis for the calibration of the material model. The model was made up by a three-term Voce hardening rule, and a CL failure criterion to evaluate damage and mimic fracture in the model through element erosion. This material model will be the material input to the numerical analyses of plates exposed to blast loading. From the manually inverse modelling, the best fit for the Voce model was when the true stress at necking was increased with 18%.

Figure 10a shows the engineering stress-strain curve from the experiment and the corresponding numerical predictions, while Figure 10b shows the spread in experimental data in addition to the numerical predictions with CL failure added. From Figure 10a we can observe that the model can capture most of the behavior in the experiment. The hardening after yielding is rather limited, but there is a considerable amount of elongation needed before the specimen fractures. The plot in Figure 10b shows the best fit against all the uniaxial test. The fit can be regarded as an “upper” limit for all the orientations. Again, there is some spread in the fracture strain for the different orientations. Here the fit is somewhat of an intermediate value such that the model should hopefully be able to capture fracture independent of which direction in fractures initiate in the plates.

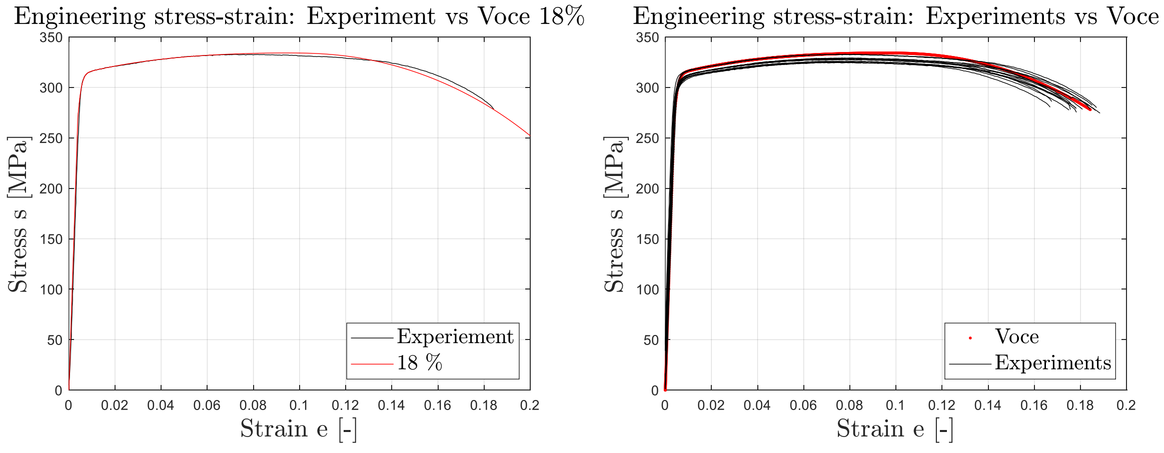

a) b)

Figure 10 – a) Shows the engineering stress-strain curve to the selected uniaxial tension test (black) and the best fit from the calibration (red). b) All uniaxial tension tests (black) plotted against the best fit with the CL criterion included (red).

Figure 11 shows how the numerical simulations behave when the CL fracture criterion is implemented in the model. All the simulations give fracture at the same time, which gives confidence in the reliability of the model. Observe that for smaller elements, i.e., more elements through the thickness, the closer one moves toward the best fit for the Voce model. This is consistent with the established theory in FEM modeling, as one moves closer to toward the exact solution as the characteristic element $h_e \rightarrow 0$.

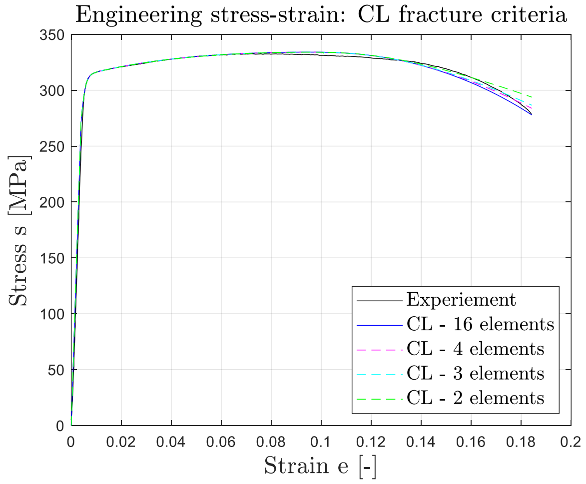

Figure 11 - Shows the uniaxial tension test (black) and the best fit with a CL-criterion implemented for the different number of elements through the thickness.

When simulating plates exposed to blast loading numerically one must consider the balance between obtaining more accurate results and the computational cost of having more elements through the thickness over the entire plate. The result in Figure 11 suggests there is flexibility in choosing the number of elements since they are in fairly good agreement with each other.

The results in Figure 11 indicate that the numerical simulations are in good agreement with the experimental data. However, we note that the material is inherently anisotropic, as indicated by the R-values in Table 2, and we do not expect the numerical predictions to be as close to the experimental data for other orientations. This might influence the numerical analyses of the blast loaded plates to some extent, but a study of these effects is out of the scope of this work.

4 Blast loaded plates

This section covers the experimental work on aluminum plates exposed to blast loading. First, the experimental setup is described with the experimental program and the post-processing of the results using 3D-DIC. Then, the results from full plates (plates with no holes) and perforated plates with pre-cut circular holes are presented. Finally, an experimental study on plates subjected to combined ballistic impact and blast loading is presented. That is, the plates are first perforated by blunt and ogival projectiles before exposed to blast loading using a shock tube.

4.1 Experimental setup

The blast experiments were carried out in the SIMLab Shock Tube Facility (SSFT) at the Department of Structural Engineering, NTNU. A detailed presentation of the SSTF is given by Aune et al. [3], discussing the reliability of the SSTF to produce repeatable planer blast waves. However, a brief presentation of the overall principle of the SSTF is given in the following for the completeness of this thesis.

A schematic presentation of the SSTF is given in Figure 12. Each test starts by filling the driver section with compressed air, increasing the pressure to its desired level. The driver and driven sections are separated by the firing section where several intermediate chambers are separated by diaphragms. Each of these chambers are filled with compressed air and the diaphragms are used to maintain equilibrium with the pressure that builds up in the driver. When the pressure reaches the desired level, the intermediate chamber closest to the driver section is rapidly vented resulting in a sudden drop in pressure. The diaphragms are not able to withstand this pressure difference and undergo complete failure resulting in a shock wave propagating into the driven section and a series of rarefaction waves propagation into the driven section.

The ratio of the length between the driver and driven part is designed such that the reflected rarefaction waves catch up with the shock wave before reaching the test specimen. Resulting in a pressure profile similar to what is observed in far-field explosive detonations[3]. The length of the driven also allows the shock wave to develop such that the wave is a planer as it interacts with the test specimen. The blast intensity was varied by using different initial firing pressures in the driver section.

The pressure is recorded by using piezoelectric sensors (Kistler 603B), corresponding charge amplifiers (Kistler5064), and data acquisition system from National Instruments (NI USB-6356) with a logging frequency of 500 kHz. The sensors are placed 34.5 cm (Sensor 1) and 24.5 cm (Sensor 2) away from the test specimen (Figure 12).

The test specimen is clamped at the end of the driven section between the end flange and a massive steel frame with 12 M24 bolts (Figure 13b). The opening in the steel frame has the same dimensions as the driven section, i.e., a square cross-section with the dimension 300 mm x 300 mm. Two Phantom v2511 high-speed cameras were placed outside the tank and used to monitor the displacement of the plates. A two-layered transparent plexiglass allowed the cameras to see the mounted plate. The camera views are shown in Figure 13a and Figure 13c.

All plates were scanned using a laser scanner (Romer Absolute Arm 75255SI) to produce a point cloud of the plate geometry. The same applied for the plates still intact after being exposed to the blast loading, to provide an accurate reference for the permanent displacement.

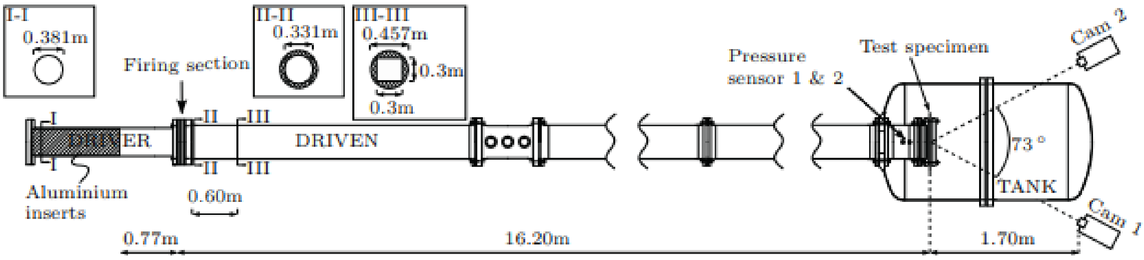

Figure 12 - Illustration of the experimental setup for blast loading experiments [3].

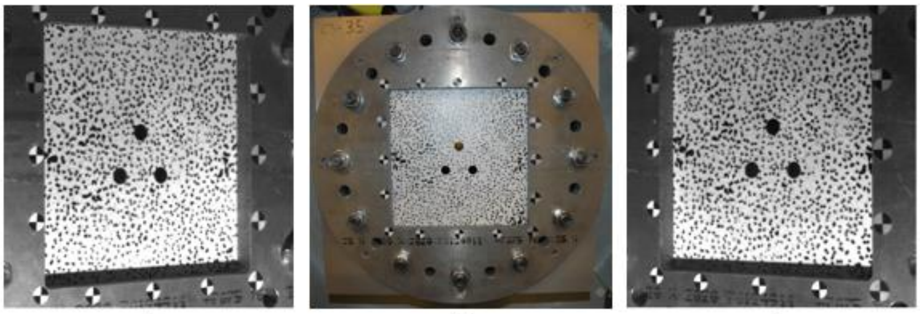
a) b) c)

Figure 13 - shows the aluminum plates clamped up pre-firing the shock tube. a) Shows the view from camera 1. c) Shows the view from camera 2. b) Shows the plate clamped between the massive steel plate fastened by 12 bolts.

4.1.1 Experimental program

The main objective is to investigate the effect of pre-formed holes in the aluminum plates. Special focus is placed on the influence of the number and position of these holes on the capacity of the plates.

The geometries considered in this thesis are already presented in Figure 1, while Table 6 shows the test matrix used for the experimental program. The numbering of each test XY-Z represents the different plates geometries and initial firing pressures in the driver. X denotes a full ductile plate with no holes (D), plates with pre-cut circular holes (C), plates perforated by a blunt projectile (B), and plates perforated by an ogival projectiles (O). Y denotes the different hole configurations with a hole in the center (1), three holes (3), and the hexagonal hole pattern (5). For the hexagonal configurations 5-1 represent the geometry shown in Figure 1d and 5-2 the geometry shown in Figure 1e. Z denotes the different firing overpressures stated in bar.

Table 6 – Experimental program.

Test	Firing pressure in driver [kPa]	Atmospheric pressure [kPa]	Initial temperature [°C]
D-05	517.3	100.1	19.9
D-10	973.2	100.1	19.8
D-15	1481.1	100.1	20.0
D-20	2050.2	99.9	20.4
D-35	3705.0	97.1	20.8
D-60	5876.6	97.2	20.8
C5-1-15	1512.8	99.9	20.3
C5-1-25	2425.0	99.3	20.2
C5-1-35	3804.7	99.3	20.5
C5-1-60	6049.4	99.2	20.8
C1-35	3674.4	99.2	20.6
C1-60	5906.6	99.6	20.4
C3-35	3707.4	98.9	20.2
C3-60	6064.9	98.9	19.7
C5-2-35	3723.0	99.1	20.2
C5-2-60	5904.7	97.3	21.0
B1-35	3660.1	98.6	20.1
B1-20	2009.6	98.2	20.5
O1-35	3642.7	98.4	20.5
O1-20	2013.0	98.0	20.7
C1-20	2057.0	97.1	20.5

An important part of the experimental work was to determine two blast intensities close to the capacity of the plates. These pressures could then be used to investigate the effect of hole configurations on the capacity of the blast-loaded plates. It was therefore decided to use the C5-1 configuration to progressively increase the pressure until complete failure was observed in the plates. Previous activities in the shock tube indicated that plates could fracture at relatively low pressures (i.e., a firing pressure of 10 to 15 bar), however, an experimental iteration showed that the firing overpressures had to be ramped up to 35 and 60 bar before the C5-1 configuration failed. The remaining hole configurations were therefore limited to experiments at these pressure levels, while the full plates were performed at the entire range of pressures for completeness.

A detailed description of the ballistic impact tests (B1 and O1) is presented at the end of this chapter. These plates were exposed to blast intensities resulting from firing overpressure of 20 and 35 bar, since these intensities were close to the capacity of these plates.

4.1.2 DIC measurements

To track the out of plane displacement in the plates during the experiment two high-speed cameras were placed on each side of the tank. This stereovision setup of the cameras allowed for a 3D-DIC analysis for each test. The recording rate for the cameras were 37 kHz with a corresponding exposure time of 30 μs and image resolution of 768x800 pixel. In addition, some pressure sensors were synchronized with the cameras using a sampling rate identical to the recording rate of the camera, allowing the pressure data to be synchronized with the picture series for all tests.

Before each experiment, the plates were sprayed with a black and white speckled pattern. This was done to enable the DIC-analysis to compare the greyscale-value fields of the speckle pattern for an image at the deformed configuration to an image at the undeformed configuration[3]. The cameras were calibrated prior to each test, and the DIC analysis was carried out using an in-house FE-based DIC code (eCorr)[24]. A structured Q4 mesh was used for each test and correlated, between the two cameras to obtain a 3D view of the plate. Before each analysis, the residual between the camera calibration and synchronized mesh was calculated and if this residual showed sufficient low values the analysis was run [21]. Figure 14 illustrates the use of the 3D-DIC, where Figure 14a and Figure 14b shows the mesh applied to one of the C5-2 specimens, and Figure 14c and Figure 14d shows the specimen at maximum displacement. The 2x2 checkerboards around the steel frame were used to track the axial movement of the entire facility that was a result of the sudden release of momentum when the gas was released.

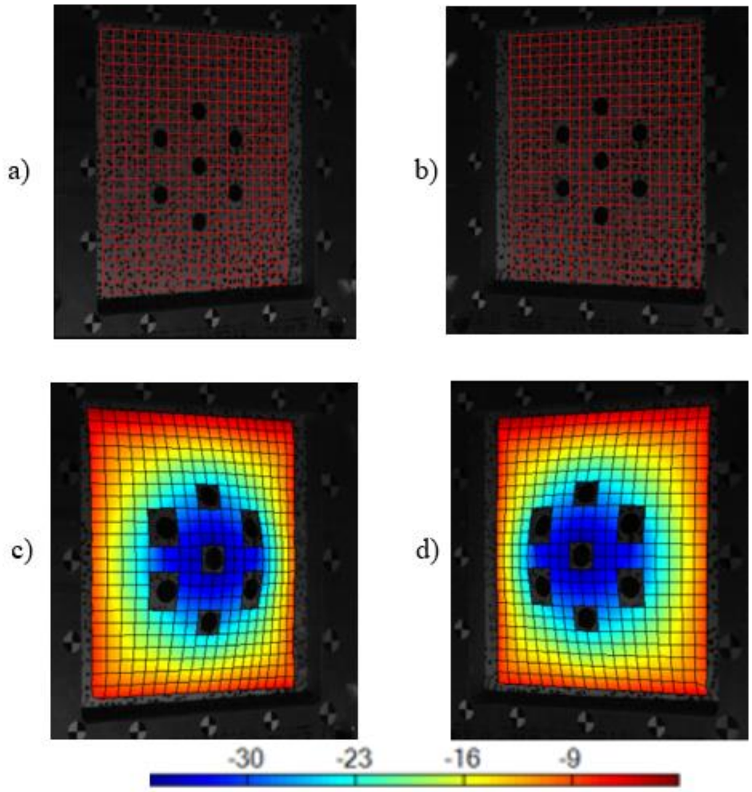

Figure 14 - Show the use of the 3D-DIC software in eCorr. a) Shows the mesh applied to a C5-2 plate for camera 1 and b) for camera 2. c) Shows an out of plane displacement filed and for camera 1 and d) for camera 2. The displacement field is shown at maximum displacement for test C5-2-35.

From the DIC analysis, the midpoint deflection was extracted for the plates with no holes in the center of the plates. Deformation profiles along selected cross-sections could also be extracted for each test at the times recorded by the high-speed cameras.

4.2 Pressure measurements

After the diaphragms burst the incident overpressure travels down the driven section, eventually passing by Sensors 1 and 2 upstream the target plates (see Figure 12), immediately before the blast wave impacts the test specimen. The best estimate of the reflected overpressure acting on the plates in each test is therefore the recording at Sensor 2 and Sensor 1. These pressures behavior can be seen in Figure 15a where the pressure curves for Sensors 1 and 2 from the experiment D35 are plotted. The scope of this work is to look at the dynamic response of the plate and not the permanent response, limiting the time-window of interest in each test to the positive phase of the pressure histories.

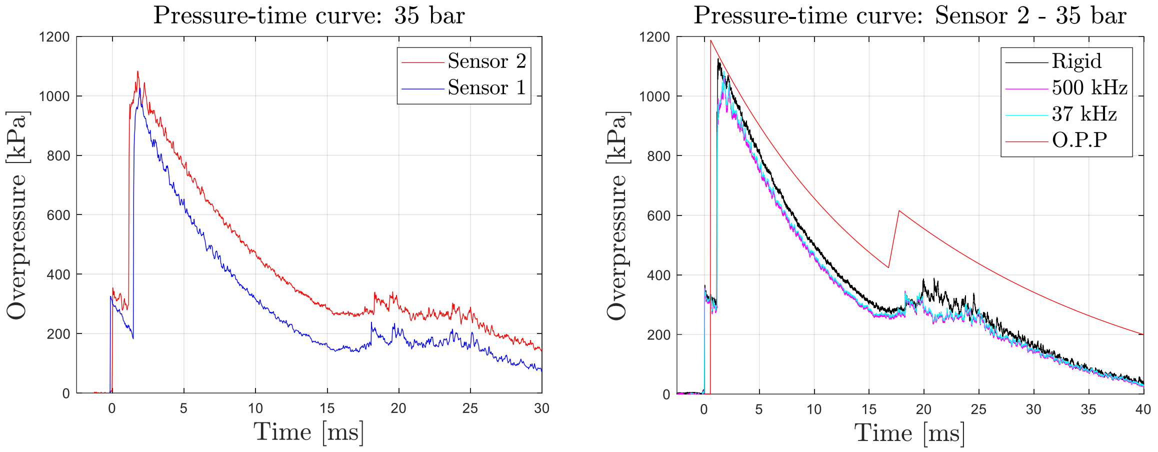

a) b)

Figure 15 - a) pressure-time curves from Sensor 1 (blue) and sensor 2 (red) in test D35. b) Pressure-time curves for Sensor 2 with sampling frequency 37 kHz (cyan), and 500 kHz (magenta) for D35 plotted against the pressure-time curve at sensor 2 from the experiment (black) used to calibrate the idealized on plate pressure curve (red) in Ref. [3].

In Figure 15b the pressure measurement from Sensor 2 is plotted for the data synchronized with the high-speed cameras (37 kHz) and the data logged at 500 kHz. In the same graph, the pressure data from a 35 bar test on a massive plate is plotted; referred to as “Rigid”. The red curve illustrates the on plate pressure (O.P.P) that was obtained from tests on massive plates equipped with pressure sensors in Ref. [3]. Thus, the idealized on-plate pressure curve represents the reflected overpressure acting on a non-deformable plate.

The difference between the idealized on-plate pressure curve and the measurements at Sensor 2 is seen in Figure 15b, i.e., the on plate pressure curve experience one distinct jump in pressure from zero to peak reflected overpressure, p_r, while Sensor 1 and 2 measure both the incident and reflected upstream the target plate. To build confidence that these idealized on-plate pressure curves could be applied in the numerical study, one had to ensure that the incident pressure was similar at sensor 2 (or 1) for similar magnitudes of firing pressure used to calibrate the idealized on-plate pressure curves. From Figure 15b and Figure 16, the incident pressure curves are almost identical to the curves used to calibrate the on-plate pressure curve. This trend was observed for all the pressure levels used in this work. Based on these observations, the idealized on-plate pressure curves will be used to represent the loading on the plates in the numerical simulations in this thesis.

It is noted that the peak reflected overpressure is slightly reduced in the test with deformable plates compared to the “Rigid” curves obtained from non-deformable plates in Ref. [3]. This observation can be a result of fluid-structure interaction (FSI) effects between the blast wave and the deformable aluminum plates. Aune et al. [3] argued that these types of FSI effects may be due to the imposed velocity in the deformable plates and the deformation of the plate itself which absorbs some of the energy through plastic work.

For the configurations with pre-formed holes, it is also reasonable to assume that some of the pressure will travel through the holes and into the tank and therefore slightly reducing the reflected pressure in from of the plates.

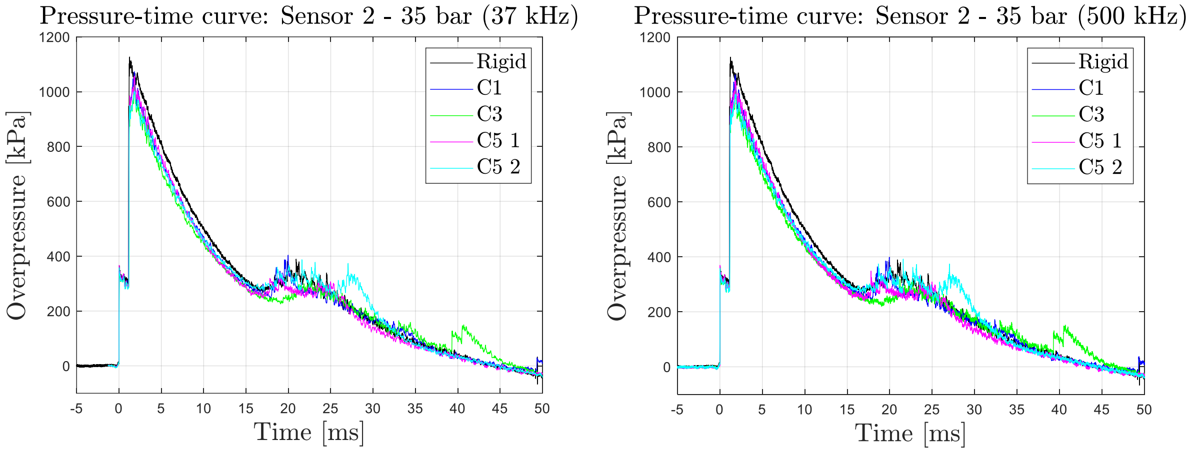

a)   b)

Figure 16 - a) shows the pressure-time curve for the holed configurations with a sampling rate of 37 kHz compared to the curve from the experiment used for calibrating the on-plate pressure for a firing overpressure of 35 bar. b) shows the pressure-time curve for the holed configurations with a sampling rate of 500 kHz compared to the curve from the experiment used for calibrating the on-plate pressure in Ref. [3], a firing overpressure of 35 bar. Rigid (black), holed configuration C1 (blue), C3 (green), C5-1 (magenta), and C5-2(cyan).

4.3 Full plates – experimental results

The full plates with no pre-formed holes showed good resistance against blast loading for all tests considered in this work. Even at the highest pressure there was no indication of failure or crack initiation. Figure 17 shows the D60 test in its initial configuration, at maximum displacement, and the final configuration after the entire facility had come to rest.

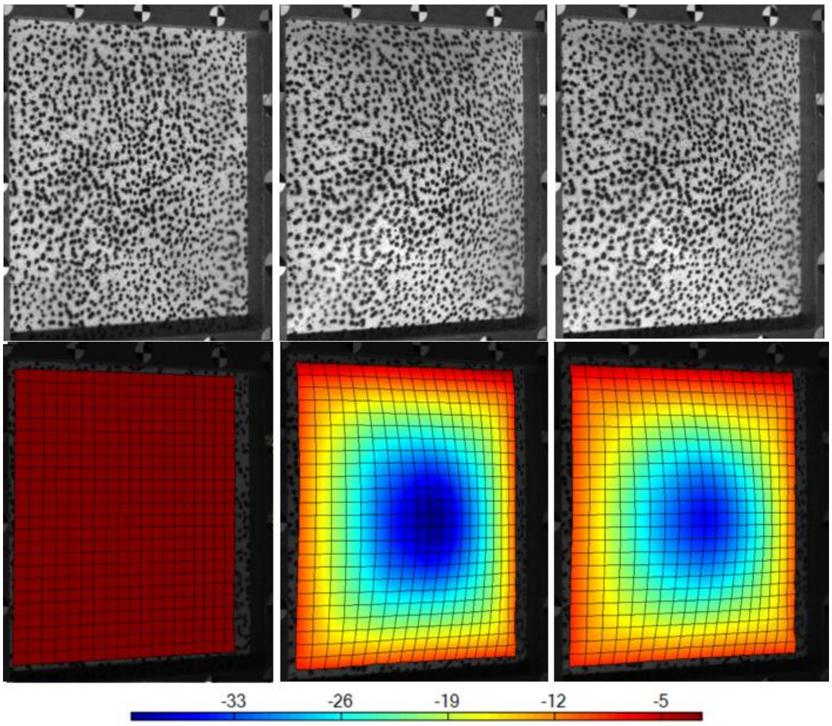

Figure 17 - shows the D60 test viewed from camera 1. The upper row is pictures from high- speed camera 1 and the lower row is the 3D-DIC analysis of the out of plane displacement. The color bar shows displacement in mm. From left to right the figure shows the plate in its initial configuration (left), maximum displacement (middle), and final deformation when the facility has come to rest (right).

From the 3D-DIC analysis, the midpoint deflection and axial movement were found. An accurate description of the plate deformation was obtained by subtracting the axial movement of the SSTF from the midpoint deflection from eCorr. The midpoint deflection for the D20, D35, and D60 test are illustrated in Figure 18a. These results indicate that the maximum displacement of the plates occurs immediately after the blast wave impacts the plate. After the initial impact, the deformation decreases and oscillates around a permanent deformation state as the blast wave is reflected. As expected, increasing blast intensities results in a larger deformation of the plate. The cross-section of the full plates at maximum displacement is shown in Figure 18b. Here there is a clear indication that the largest displacement occurs in the center of the plates and moves toward zero at the clamped boundaries.

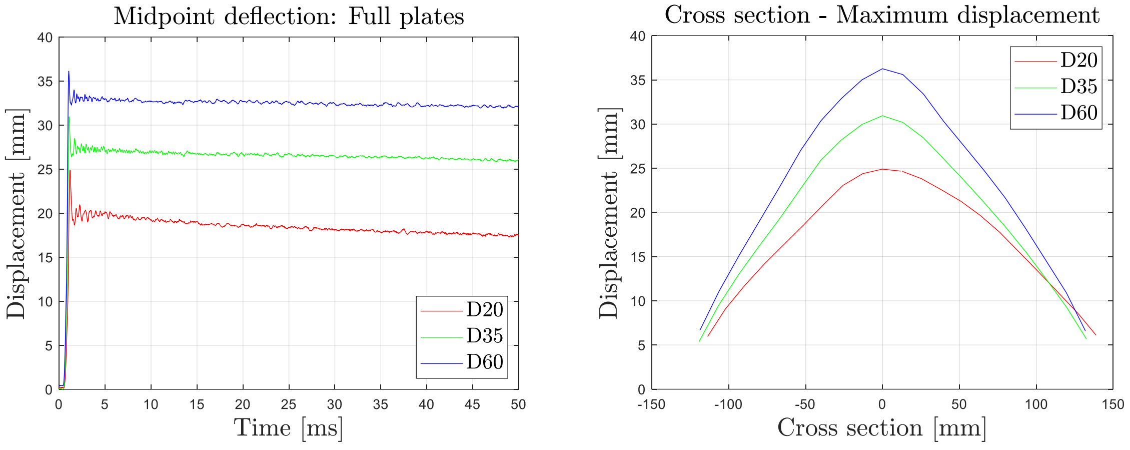

a) b)

Figure 18 - a) Midpoint deflection of the plate for test D20 (red), D35 (green), and D60 (blue). b) shows the cross-section of the plate for the test D20 (red), D35 (green), and D60 (blue) at maximum displacement.

Note that only tests D20, D35, and D60 are presented in Figure 18. This was done simply because these were the pressures used in the study of perforated plates. Figure 19 shows how the cross-section develops as it is impacted by the shock wave for the D60 test. The development shows deformed shapes that are typical for blast loaded plates, i.e. plastic hinges starting from the supports and travels along the diagonals toward the center of the plate. It is also seen that the deformed shape resembles a global dome at the final deformed configuration.

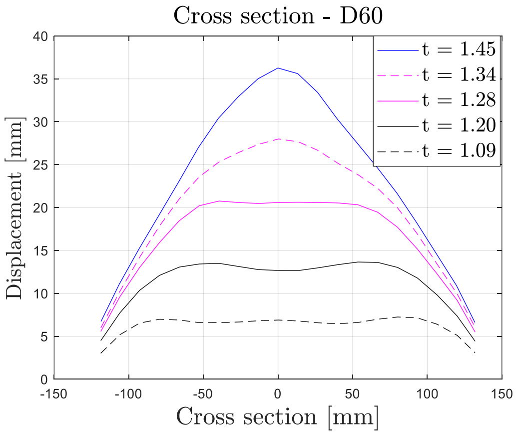

Figure 19 - show how the cross-section change for a full plate exposed to firing overpressure of 60 bar. t denotes the time, in ms, after the blast wave passes sensor 1 (where $t_a = 0$ ms).

4.4 Plates with pre-formed holes – experimental results

The major part of the experimental work is focused on the performance of perforated plates exposed to blast loading. Figure 20 shows the plates with pre-cut holes exposed to a firing overpressure of 35 bar. The figure shows from left to right the initial configuration, maximum displacement, and the final configuration of the plate.

For C1 the plate did not rupture (Figure 20a), but there was some expansion of the center hole and permanent displacement due to plastic deformation in the plate. For C3 an interesting deformation pattern occurred (Figure 20b). Two cracks initiated in the diagonals between the upper hole and the two lower holes. No fracture occurred between the two lower holes, but a considerable plastic deformation occurred due to rotation of the triangle area in-between the holes.

The C5-1 (Figure 20c) test observed no visible damage except for the permanent deformation due to global, plastic deformations, while C5-2 (Figure 20d), experienced vertical cracks on both sides of the hexagon structure of holes. This was a very interesting observation since C5-1 and C5-2 have the same hexagon hole configuration, except that C5-2 is rotated 90° with respect to C5-1. All the plates were still in place in their clamped position since none of the plates experienced collapsed after being exposed to the blast loading. Note that the final picture of both C5 configurations show pieces of failed diaphragms bundled up in front of the plate. These results in less evident views of the pre-formed holes in these pictures.

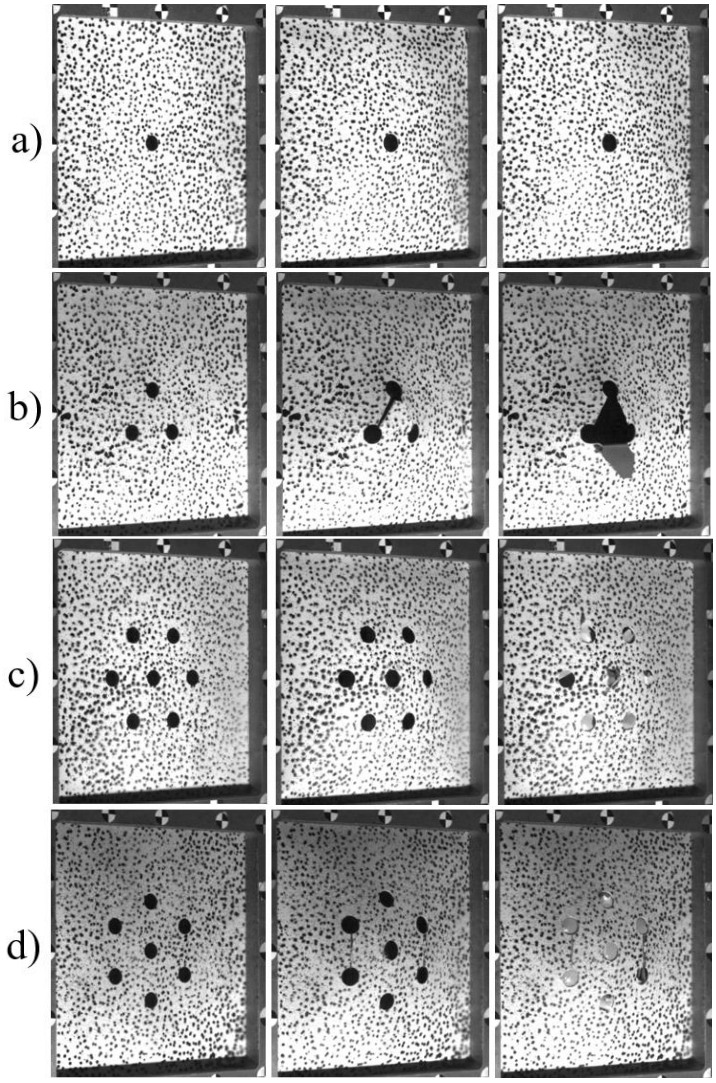

Figure 20 - show the perforated plates with pre-cut holes exposed to firing overpressure of 35 bar. From left to right the initial configuration, maximum displacement, and final deformation state. a) C1-35, b) C3-35, c) C5-1-35, and d) C5-2-35.

For the tests with firing overpressures of 60 bar, the effect of the pre-formed holes became even more evident. Figure 21 shows from left to right the configurations in the initial configuration, when cracks started to initiate, and crack propagation. Three cracks initiated from the center hole and propagated toward the corners for the C1 (Figure 21a). The cracks propagated to their respective corner until the entire plate was torn away from its clamped position. The crack propagation did not follow the straightest path toward the corners, but as the cracks closed in on the clamped boundary the cracks turned toward the corners.

For C3 (Figure 21b) the same deformation pattern as in C3-35 was initiated with cracks developing in the diagonals between the upper hole the two lower holes. Then, two cracks were formed from the upper hole propagating in the direction of the upper corners. After the cracks in the diagonals between the holes have fully formed, one crack from each of the lower holes are initiated toward their respective corner. The triangle is still in one piece as the cracks propagate to the corners.

The C5-1(Figure 21c) had an interesting deformation pattern where cracks initiate between the holes in the outer part of the hexagon. The propagation of cracks between these outer holes occurred more or less symmetrically, resulting in a near-complete separation of the hexagon before cracks propagated toward the corners of the plate from their respective closest hole. It was interesting to note that no crack initiation was observed inside the hexagon itself.

As in the 35 bar test, the C5-2 configuration (Figure 21d) experienced a different failure pattern where cracks formed vertically in the outer hexagon of holes. Then, instead of propagating around the hexagon as in C5-1, two cracks were initiated from the center hole propagating out toward the outer circle in a diagonal pattern. Finally, when these two cracks reach the hexagon structure. Cracks initiated from the holes closest to the corners and propagated until the complete failure. Note that all plates exposed to firing overpressure of 60 bar collapsed.

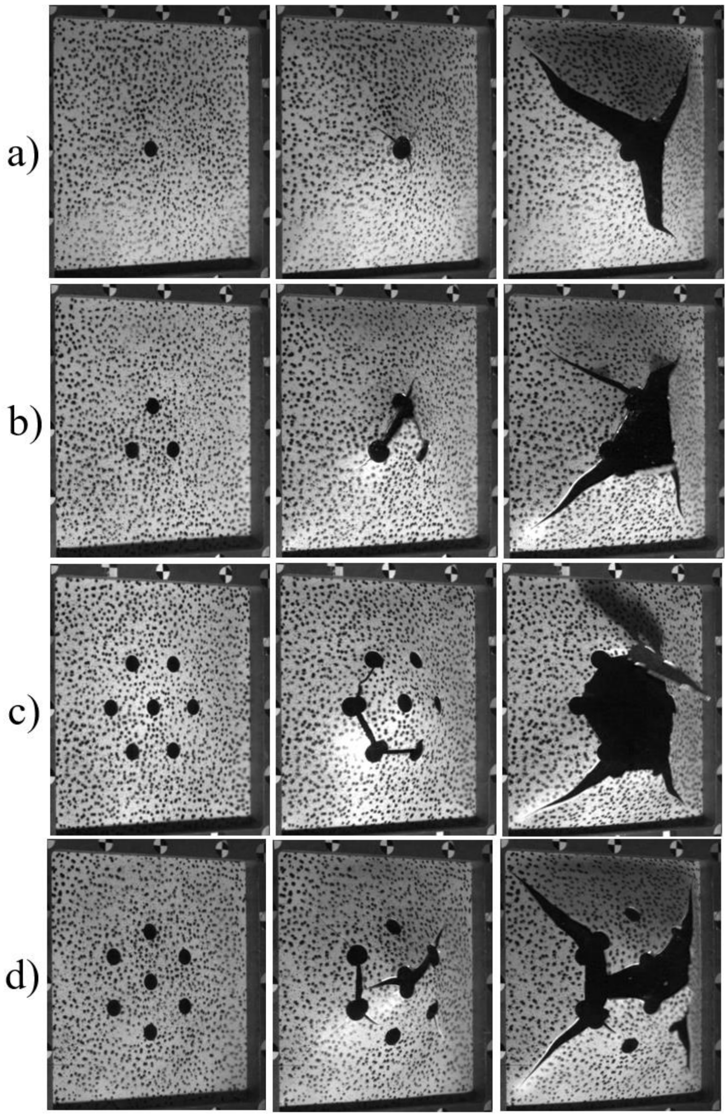

Figure 21 - show the perforated plates with pre-cut holes plates exposed to firing overpressure of 60 bar. From left to right the initial configuration, maximum displacement, and final deformation state. a) C1-60, b) C3-60, c) C5-1-60, and d) C5-2-60.

4.5 Plates perforated by projectiles – experimental results

4.5.1 Ballistic impact test

In addition to the plates with perfectly pre-cut holes presented in Section 4.4, it was decided to investigate the combined effect of plates perforated by projectiles prior to the blast loading. Special focus was placed on the influence of projectile geometry on the capacity during subsequent blast loading. Six full plates were therefor exposed to ballistic impact in the SIMLab gas gun, where three plates were perforated by a blunt projectile and the remaining three plates by an ogival projectile. The diameter of the projectiles was 20 mm and was intended to create holes with the same position as the pre-cut holes in the C1 configuration as in Figure 1b. To ensure that the damage localized around the impact hole the initial velocity had to be significantly higher than the ballistic limit of the plates. Rodriguez-Millan et al. [25] found the ballistic limit for 4 mm thick AA6082-T6 for blunt, conical and hemispherical projectiles to be around 150 m/s. Our plates are only 2 mm thick, which lowers the ballistic limit even further and an initial velocity over 300 m/s was expected to be sufficient. Precise values for initial and residual velocities are given in Table 7. The experimental setup was similar to that of Dey et al. [26] and is shown in Figure 22. An image series showing the blunt and ogival projectile perforating a plate, and the dimension of the projectiles can be seen in Figure 23.

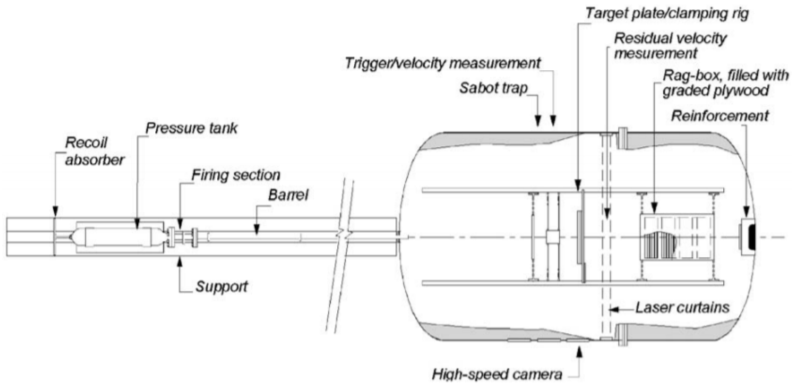

Figure 22 - Illustration of the experimental setup for ballistic impact experiments [26].

Table 7 – initial velocity (v_i) and residual velocity (v_r) for the gas gun experiments with blunt and ogival projectiles

Blunt	v_i [m/s]	v_r [m/s]	Ogival	v_i [m/s]	v_r [m/s]
Test 1	331.1	323.1	Test 1	331.7	325.8
Test 2	332.8	321.3	Test 2	331.6	325.9
Test 3	334.6	323.3	Test 3	328.8	321.8

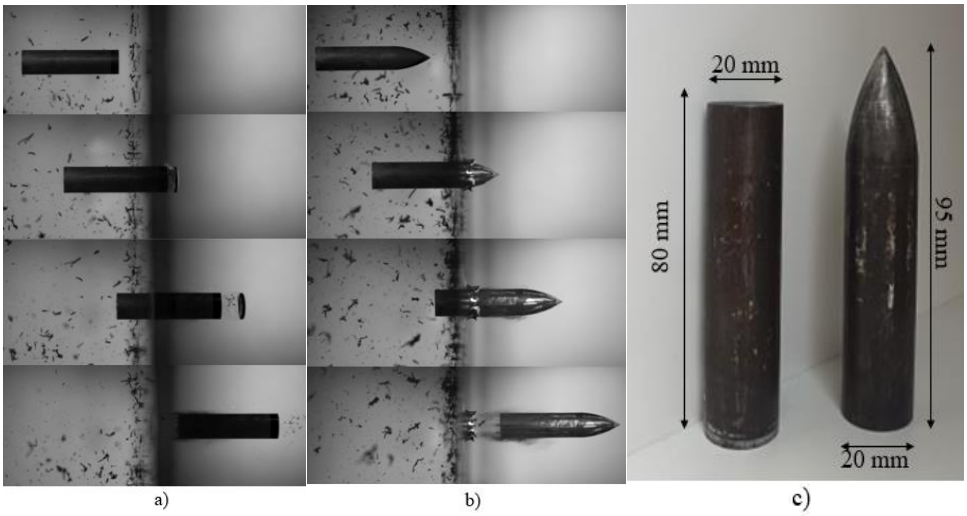

Figure 23 - a) shows a time series of a plate perforated by a blunt projectile. b) Shows a time series of a plate perforated by an ogival projectile. c) Show the dimensions of the blunt and the ogival projectile.

Four plates were chosen from the gas gun experiments to be exposed to blast loading in the shock tube, i.e., two plates perforated by a blunt projectile and two plates by an ogival projectile, respectively. The choice of plates were based on their similarities in geometry and cracks around the perforated hole. For the plates exposed to blunt projectile the failure phenomenon was plugging for all plates (Figure 24b). Which left an almost clean cut in the plate, except for some minor cracks spread around the hole due to the plugging[27].

The damage caused due to ogival projectiles was more severe than that of the blunt projectiles (Figure 24c). The failure mode due to ballistic impact from an ogival projectile was petaling, where it is well known that the projectile causes a high radial and circumferential stress after the initial stress wave occurring at the tip of the projectile. Petaling is characterized by the star-shaped cracks and the local permanent deformation in the plate [27]. This fracture pattern was very interesting in view of the subsequent blast test on the same plates since several cracks initiated around the perforated hole (see Figure 24c).

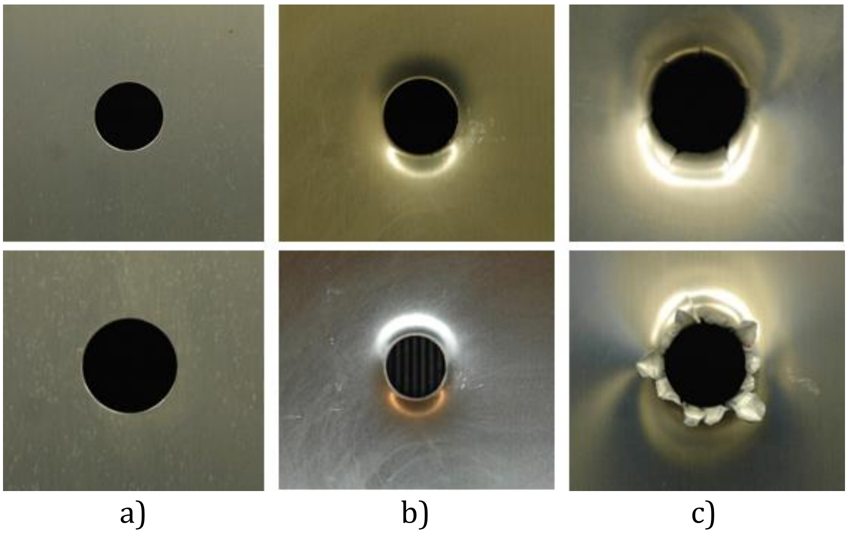

Figure 24 - a) Show pre-cut a C1 configuration. b) Show a plate exposed to blunt projectile. c) Show the plate exposed to an ogival projectile. Upper row show the side of the plate hit by the incoming projectile. Lower row shows the side where the projectile ejected.

4.5.2 Shock tube tests

The perforated plates were then moved to the SSTF and exposed to blast loading. The tests for the C1 configuration were used as the basis of comparison for the plates perforated by blunt and ogival projectiles, since they shared most similarities in geometry. Since C1-35 did not fracture, a firing overpressure of 35 bar was chosen for the perforated plates, because the small cracks around the perforated hole were expected to affect the capacity of the plate.

For B1-35 four cracks started to develop from the perforated hole (Figure 25a). The cracks initiating in the upper half of the plate were almost aimed directly for the corners, while one of the "lower" cracks started to propagate toward the lower boundary, before it suddenly made a sharp turn toward the corner. It is suspected that the initial crack pattern was initiated by microscopic cracks in the perforated hole. The O1-35 test showed the same behavior except that the cracks had a more direct path toward the corners (Figure 25b). Both plates experienced total collapse.

Since both the B1-35 test and O1-35 collapsed it was clear that the capacity of the plates was reached for a firing overpressure of 35 bar. It was therefore decided to reduce the firing overpressure to 20 bar in the two remaining tests, in an attempt to avoid complete failure of the plates. The results from the B1-20 and O1-20 test can in Figure 26. The B1-20 showed no visible crack formation (Figure 26a), but a more detailed investigation showed that one small crack initiated from the hole. There was also some considerable global, plastic deformation in the form of permanent out of plane deformation. The O1-20 test displayed visible cracks initiating from the perforated hole (Figure 26b). However, the crack propagation stopped before reaching the plate boundary. Thus, the plate was intact after the experiment. By initiating damage and not having the plates experience total collapse. The conclusion was that the test had been close to the capacity limit of the perforated plates.

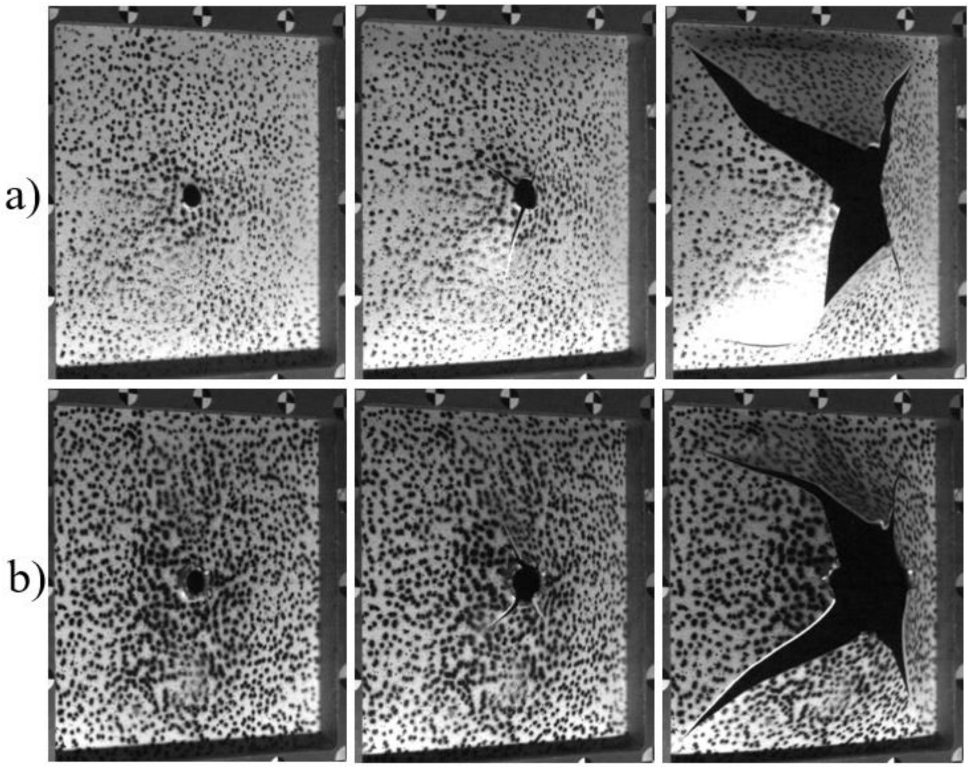

Figure 25 - show the plates perforated by projectiles exposed to firing overpressure of 35 bar. From left to right the initial configuration, crack initiation, and developed crack. a) B1-35 and b) O1-35.

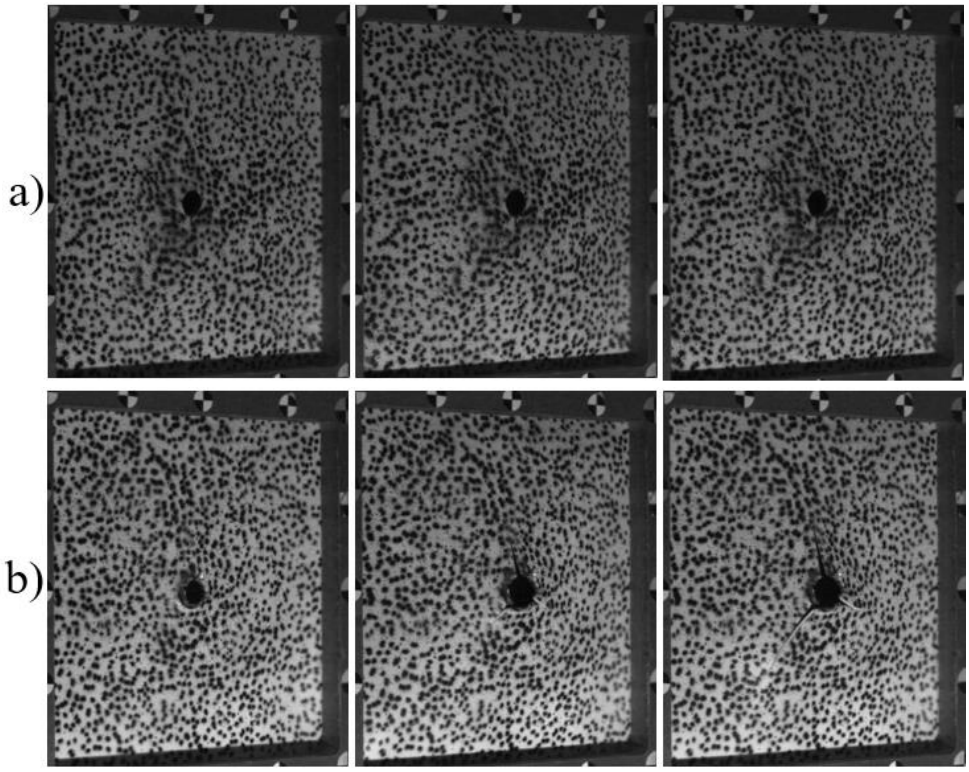

Figure 26 – show plates perforated by projectiles exposed to firing overpressure of 20 bar. From left to right the initial configuration, maximum displacement, and final deformation state. a) B1-20 and b) O1-20.

4.6 Discussion

In the context of investigating the effect of plates perforated with circular holes, that are either pre-cut or produced by projectiles, it is clear that it has a significant effect on the capacity of the plates under investigation in this thesis. None of the full plates experienced failure for any of the pressure levels used in this thesis, whereas several of the perforated plates experienced crack initiation and complete failure.

The main differences between the different configurations in this experimental program were the number of circular holes, their placement, and if the holes were pre-cut or made by projectiles. For the tests exposed to a firing overpressure of 35 bar, the C1 configuration showed no sign of cracks or damage except for the global out of plane deformation, while the C3 and C5-2 configuration both showed cracks at this blast intensity. To state that there is a direct correlation between the number of holes and decreases in the capacity based on these results are somewhat contradicted by the result in the C5-1 test, where no cracks were initiated. As previously stated, the only difference between the C5-1 and C5-2 configurations is that the geometry of the holes is rotated 90°. This means that if the number of holes had been the only parameter causing the capacity of the perforated plates to be reduced, the C5-1 should have showed cracks at this loading intensity.

This last point indicates that the position and orientation of the pre-cut circular holes may have a considerable effect on the behavior of the plates. This is even more evident at a firing overpressure of 60 bar where all perforated plates experience collapse. There is a tendency that cracks initiate in the holes closest to the corners of the plate (see Figure 21). Furthermore, in configurations where one hole is equally distanced from two or more corners, more cracks initiate in that hole (see Figure 21a and Figure 21b). In the C1-60 test three cracks started to propagate toward their closest corner. For C3-60 two cracks start in the "upper" hole while one crack is initiated in the two lower holes toward their closest corner, after the diagonal cracks between the upper hole and lower holes are fully developed. This indicates that the position of the holes will affect the crack initiation. Both the C5-1 and the C5-2 configuration seem to behave in a similar way when it comes to the crack initiation, i.e., one crack initiate in the holes closest to their respective corner after the cracks in the middle are developed.

However, C5-1 and C5-2 that are the same geometry, except for the 90° rotation, have quite different evolution of the crack propagation resulting in different failure modes. Both configurations begin their failure in the outer hexagon structure of holes, then C5-2 fractures in the center hole while C5-1 fails around the hexagon The observation that the C5-2 configuration fracture diagonally in the center while the C5-1 fails between the holes in the hexagon very interesting. However, it is difficult to reason and conclude on the governing phenomena for this difference based on the experiments. Possible explanations will, therefore, be investigated in the numerical study in chapter 5.

Finally, the plates that were perforated by projectiles showed a significant reduction in the capacity against blast loading compared to the plates with perfectly cut holes. The petaling failure mode produced by ogival projectiles induced large cracks in the geometry around the exit hole. One can expect a lower capacity for plates with preexisting damage since the cracks creates a stress concentration and have already accumulated some damage at the crack tip. This allows the cracks to be propagated more easily and for smaller blast load intensities. The plates exposed to the blunt projectiles showed less crack initiation around the hole compared to the ogival ones. Nevertheless, some damage was observed in the holes where plugging occurred, and this could be enough to significantly reduce the capacity of the plates. Since both B1-35 and O1-35 failed it is fair to say that the combined effect of a projectile and blast loading drastically reduces the capacity of the plate.

It is challenging to conclude on what is most critical of blunt or ogival projectiles combined with blast loading. Both failed at initial driver pressure at 35 bar and both showed signs of crack development at 20 bar. The cracks were more severe for the plate perforated by the ogival projectile at 20 bar compared to the blunt perforated plate. Nevertheless, both plates were more or less intact after the tests and more experiments should be carried out for further investigations on the influence of the projectile geometries on the capacity of perforated plates. Still, this study shows a clear trend that ogival projectiles introduce petaling cracks around the exit hole of the projectile. Such cracks are expected to be more crucial for the capacity with respect to subsequent blast loading, compared to the plugging failure mode observed with blunt projectiles. It is reasonable to assume that larger pre-existing cracks in the plate will reduce the capacity of the plate in resisting a blast load. But how the length, shape, or position of the crack influence the capacity are difficult to state based on the limited number of experiments.

The issue with the combined effect of ballistic impact and blast loading is that it is difficult to reproduce the exact same damage caused by the projectiles. In this thesis, the plates chosen to be used in the shock tube were based on which plates showed similar damage concerning the number of cracks and their length. This leaves an initial variability between the plates before the shock tube experiment, resulting in an uncertainty on how the plates will respond to the blast loading. One should, therefore, be careful to conclude based on just four tests. Note that this is regarding the effect of what is most critical between ogival and blunt projectiles. Since it clear that the plates perforated by projectiles show a reduced capacity compared to the plates with pre-cut circular holes, as both B1-35 and C1-35 collapsed while C1-35 did not show any damage other than then permanent plastic deformation.

One final point to observe from the shock tube experiments with pre-cut holes are the non-symmetric failure modes. C3-60 is the only test at 60 bar that show symmetry in the crack propagation. While all the other show a non-symmetric crack pattern. This is important to have in mind when assessing the plates numerically, since symmetry is often used in numerical models to save computational time and storage space.

5 Numerical study

This section covers the numerical models that are used to investigate the plate response at different blast intensities, as seen in section 4. First, a description of the numerical models is presented. Second, the results for the full plates will be compared to the experimental results. Then, a numerical study of the perforated configurations is presented and lastly an investigation of the perforated plates concerning the damage parameter W and its field variables $\dot{p}$ and σ_I. Although we performed experiments on the combined effect of ballistic impact and blast loading, we will leave this out of the numerical study. This is because ballistic impact is a local problem [27], while blast loading is a global problem[28]. In numerical FE analysis these two problems have opposite mesh distribution requirements, which imposes a need for extreme computational resources and a complexity in the simulation that is outside the scope of this thesis.

5.1 Numerical models

The numerical simulations of the plates were all carried out in Abaqus/Explicit CAE 2019. Numerical models with shell elements and solid elements were made, and there were only some minor changes between the models generated with these two element types. This description is based on the solid models and at the end of this section, the changes done to create the shell models are mentioned. A 3D deformable homogeneous solid was created with dimensions 300 mm x 300 mm, which represented the area of the plate exposed to blast loading in the shock tube experiments. The plate was extruded with a thickness of 2.08 mm to represent the average thickness of all specimens from the tensile test. For the perforated configurations, circular sections were cut out from the plate with the geometries given in Figure 1.

To circumvent mesh convergence issues with the models, the same characteristic element sizes and element type used to calibrate the material parameters found in chapter 3 were utilized. This method is known in the literature as computational cell approach [29]. The element type selected was the linear brick element with reduced integration C3D8R element, and two elements through the thickness was chosen with the characteristic element size shown in Table 5 with the corresponding failure parameter. An effort was made to make the entire mesh structured, which means to make the mesh regular with similar element geometry and in this case square elements. For the full plate, this is an easy procedure, while for the perforated plates the holes created an irregularity that did not allow for a regular mesh all over the entire plate. This problem was surpassed by creating partition cells around each hole, such that the mesh generation algorithm could create structured mesh for all configurations.

The material was assumed to be isotropic and the elastic parameters in Table 3 were used. The calibrated Voce model (see Section 3) was used to describe the plastic behavior and the CL failure criterion was used to account for material failure through the same VUHARD subroutine as described in section 3.3.1. A dynamic explicit loading step was applied with isothermal conditions. The duration of the step varied depending upon the blast intensity and the plate configurations. For the full plates, a longer time step was chosen to see the effect over time. When evaluating the perforated models only the initial response with fracture and deformation pattern was interesting, and therefore a smaller time step was used to save storage space and computational time.

The entire plate boundary was fixed against any displacement and rotation in all directions to simulate the clamped behavior seen in the experiment. This is a simplified way to treat the boundary conditions in the simulations, but is rather efficient concerning computational time. The alternative is to model the entire clamped assembly shown in Figure 13b and formulate a contact condition between the plate, clamping assembly, and the bolts. This was done by Aune et al. [11] and showed that it can be done at a computational cost compared to fixing the entire boundary.

The blast load was applied as a uniform pressure over the entire plate, which implies that the plates in the simulation get exposed to a planar shock wave. The investigation of pressure measurements in section 4.2 showed that there was good agreement between the experiments in this thesis and the experiments used to calibrate the idealized on-plate pressure curves (referred to as "Friedlander fit" in Aune et al. [3]), regarding the incoming blast pressure. Consequently, these idealized on-plate pressure curves were used to represent the blast loading in the simulations. This way of implementing the blast loading assumes that the pressure is unaltered during the deformation of the plate, i.e., there is no coupling between the pressure applied to the plate and the plate deformation. This is referred to as an uncoupled approach[28]. This may not precisely represent the actual behavior since the deformation of the plate is quite significant in some of the experiments. However, the objective of this study is to look at the response of the plates exposed to the initial shock wave and assess if the models can capture the deformation and fracture patterns observed in the experiments. The uncoupled approach is simple and computationally efficient, without having to use a lot of resources to accurately describe the altering pressure as the plates deform.

The on-plate pressure curves were calibrated from the pressure-time histories extracted from sensors mounted on a rigid plate. The pressure-time history was used to calibrate the terms in the modified Friedlander equation seen in Equation 13.

$$P_r(t) = P_{r,max}\left(1 - \frac{t - t_a}{t_{d+}}\right)\exp\left(\frac{-b(t - t_a)}{t_{d+}}\right) \tag{13}$$

The equation is limited by $t_a \leq t \leq t_a + t_{d+}$. Here $P_{r,max}$ is the peak reflected overpressure, t_a is the time of arrival as the blast wave hits the plate, t_{d+} is the duration of the positive phase, and b is the exponential decay coefficient. The parameters of the Friedlander equation were obtained from Aune et al.[3] and can be found in Table 8. With these idealized on-plate pressure curves the pressure was applied in a tabulated manner in the FE models.

Table 8 - Parameters for the Friedlander equation calibrated from pressure measurements on a rigid plate test [3].

Test	$P_{r,max}$ [kPa]	t_{d+} [ms]	b [-]
XY-20	756.8	50.9	2.666
XY-35	1105.2	73.9	1.904
XY-60	1446.1	75.3	1.768

The shell models of the plates were modelled as a 3D deformable homogenous shell. The section assignment allowed for the specification of the shell element to have a thickness of 2.08 mm and 5 integration points through the element thickness. The element type chosen was the S4R element. The size of the characteristic element was set to 3 mm x 3 mm and with CL failure criterion $W_c = 120$ MPa obtained from another activity (see section 3.5).

Figure 27 illustrates the different models with their characteristic element size. The upper row (a-e) shows the models with shell elements and the lower row (f-j) shows models with solid elements. All plates have a structured mesh with quadrilaterals elements, even though it does not appear like that in the figure. This is only an illustration problem because of the number of lines per pixel. Which produces these strange patterns. As one zooms in on the plates it is clear that they all have a structured mesh with quadrilateral elements.

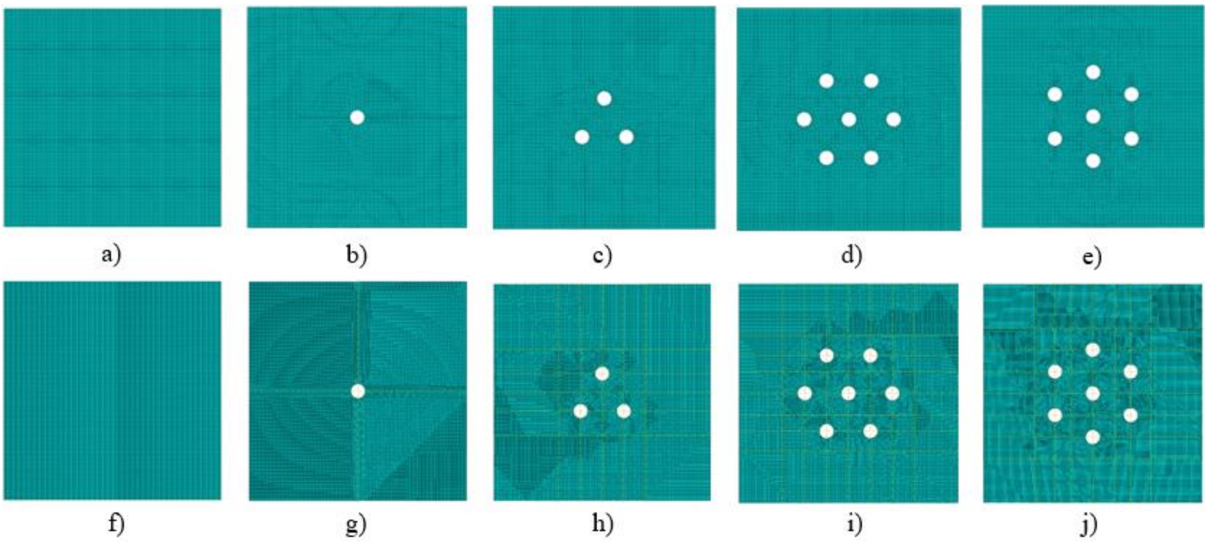

Figure 27- a-e) shows the shell models with characteristic element size 3x3 mm. f-j) shows the solid models with characteristic element size 1.04x1.04 mm that gives two elements through the thickness. Here a) Full plate, b) C1, c) C3, d) C5-1, e) C5-2 is modelled with shell elements and f) Full plate, g) C1, h) C3, i) C5-1, j) C5-2 are modelled with solid elements.

5.2 Full plates results

Since none of the full plates experienced failure in the experiments, they were a good point of reference to test the accuracy of the numerical models. The firing overpressures that were interesting to investigate was 20 bar, 35 bar and 60 bar. In Figure 28 the simulation of full plates with shell elements 3 mm x 3 mm in dimension (Figure 28a) and solid elements with 1.04 mm x 1.04 mm in dimension (Figure 28b) exposed to firing overpressure at 60 bar are shown. From left to right the initial configuration, maximum displacement, and final point of the analysis are shown. In the solid model, we utilized symmetry of the plate and modelled only one-quarter of the plate, which saved storage space and drastically reduced the computational time for the model. In the figure, the mirror option in Abaqus across the symmetry axes are used to show a full plate.

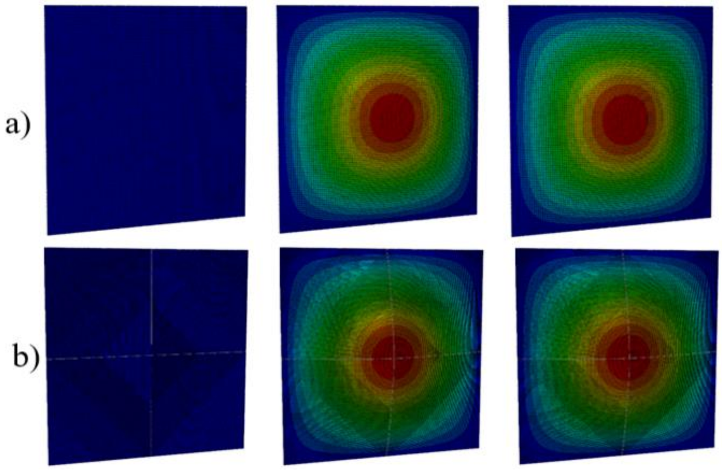

Figure 28 - show the numerical simulation of the full plate exposed to a firing overpressure of 60 bar for a) shell elements and b) solid elements. The colors indicate out of plane displacement. From left to right the initial configuration (left), maximum displacement (middle), and the final point of the analysis (right).

The first thing to notice from the numerical model is that there were no cracks or failures in any of the simulations of the full plate, which is in accordance with the experiments. Figure 29 shows the midpoint deflection for the numerical simulation with shell elements (Figure 29a) and with solid elements (Figure 29b) compared to the experiments. The graphs show the simulations of D20 in red, D35 in green, and D60 in blue. The bold lines indicate a numerical simulation and the thin lines indicate the corresponding experiment. In general, both models seem to capture the general behavior of the experiment rather well. Where maximum deformation occurs as the blast loading impacts the plate before the plate retracts to a permanent deformation state. The tabulated pressure causes the plate to oscillate around this permanent deformation.

Even though the models seem to capture the general behavior quite well there is some discrepancy. For the D20 (red curves) the numerical models seem to underestimate the maximum displacement. This becomes even more apparent in Figure 30 where the cross-section of the full plates is plotted at maximum displacement. There is some discrepancy between the measurements in the shock tube and the numerical model for out of plane displacement and the nonsymmetric displacement for the D20 test (Figure 30a). But after the maximum displacement, both numerical models and the experiment are in good agreement with the permanent deformation for D20.

For D35 (green) the results in both Figure 29 and Figure 30b are in good agreement with each other. The numerical models capture the maximum displacement at impact and slightly overestimates the permanent deformation in the plate. For D60 (blue) the trends are opposite compared to D20. Here the maximum displacement is well represented (Figure 30c), however slightly overestimated in some parts of the cross-section. However, when it comes to the midpoint deflection over time, the permanent deformation in both the shell and solid model is larger than what we observed in the experiment.

From Figure 29 and Figure 30 there are only minor differences between the numerical models with shell elements and with solid elements. They both capture the general behavior of the plates and both display similar discrepancies compared to the experiments.

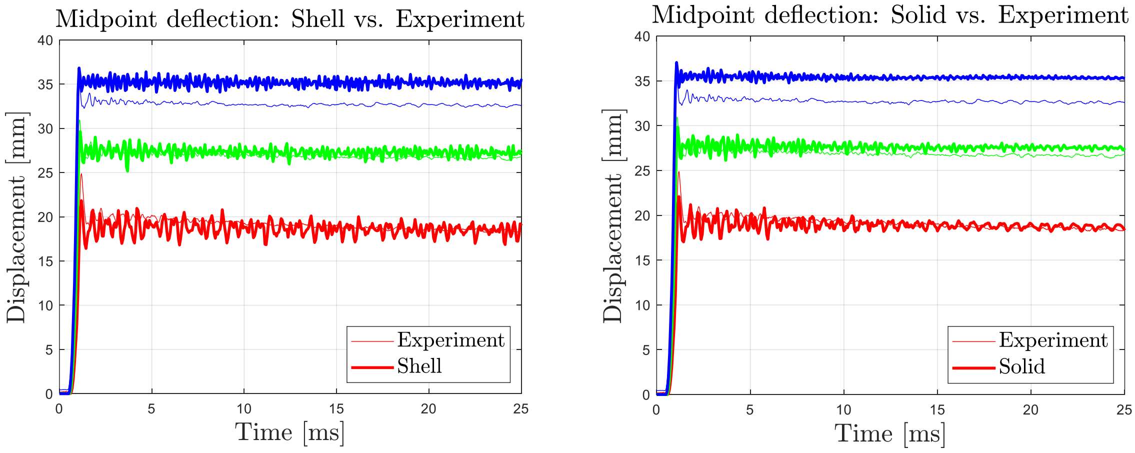

a) b)

Figure 29 - show the midpoint deflection for the experiment and numerical simulations exposed to firing overpressure of 20 bar (red), 35 bar (green), and 60 bar(blue). a) show the simulations with shell elements. b) shows the simulations with solid elements. Here the bold lines indicate simulations and thin lines the corresponding experiment.

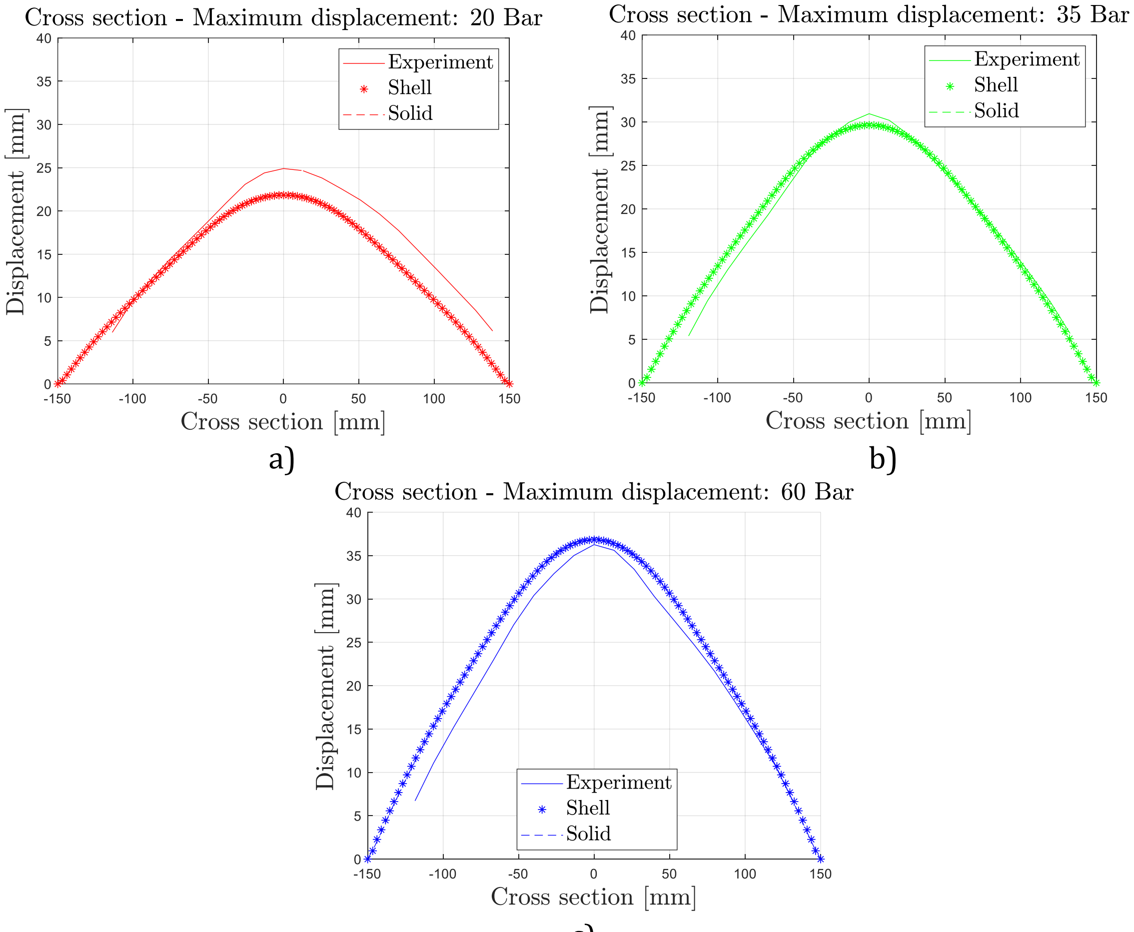

c)

*Figure 30 - shows the cross-section of the plate exposed to blast loading at the point of maximum displacement. Solid curves indicate the experiment, doted curves the simulation with solid elements and * indicate simulation with shell elements. Here a) is D20 (red), b) is D35 (green), and c) is D60 (blue).*

The numerical models are generally able to capture the deformation seen in the experiments and how the plates behave during to blast loading. Based on this study, the major difference between choosing shell or solid elements for future analysis is the computational time. The S4R elements allow the shell model to have just one element over the thickness because of the shell formulation. The solid model with multiple elements over the thickness is considerably more computationally expensive, even when the symmetry of the problem is utilized. Apart from the computation time, there are negligible differences in the results using either solids or shells in the numerical models.

Finally, the results in Figure 29 and Figure 30 give confidence to the simplified material model with Voce hardening, which was calibrated in chapter 3. The numerical simulations seem to capture the behavior of the aluminum plates that were observed in the experiments.

5.3 Perforated configurations results

Fracture propagation in the numerical simulations was enabled through element erosion. This means that when the damage inside an element reaches a critical value, i.e. $W = W_{cr}$, the element is removed from the model [29]. By using element erosion one can mimic crack propagation through a material. Since damage in ductile materials may occur due to different mechanisms, e.g. void nucleation, growth, and coalescence [30], on a microscopic level, this way of describing the damage is a rough approximation. The numerical analyses presented in this thesis apply the Cockcroft-Latham criterion to accumulate ductile damage and govern element erosion. As previously mentioned, this criterion is inherently mesh-dependent and must be calibrated for given element size.

In this section, only the results from the numerical models using solid elements are presented. The models with shell elements were computational efficient compared to the solid models. However, several of the numerical simulations using shell elements were not able to capture the crack propagation observed in the experiment, while the models with solid elements did. This is thought to be caused by the relatively coarse mesh with shell elements. Because of these observations, the choice to only present the solid results in this section was taken. For the interested reader, the results from the shell models can be viewed in the appendix.

The perforated plates with circular holes modeled with solid elements introduced some difficulties. The asymmetric nature of slant fracture expected to occur in ductile plates, which Lan et al. [31] studied to identify a fracture criterion for in thin Al 2024-T3 specimens, did not allow for symmetry in the thickness direction. Besides, some of the perforated configurations were non-symmetric and symmetry over holes concerning failure was an uncertainty when making the models. This means that the entire plate with pre-cut holes had to be modeled with solid elements, which is also regarded as the norm in numerical analyses involving fracture and crack propagation. Such a large model with small elements has a large impact on the computational time. The measure taken to circumvent this problem was to reduce the simulation time in half to $t = 12.5$ ms, this ensured that the point of maximum displacement had time to occur for all simulations since the time of impact seems to occur around $t_i \approx 1.5$ ms (see Figure 29). This halved the storage space needed to complete each simulation and was found to provide sufficient time for the cracks to propagate completely.

Figure 31 shows the numerical simulation of different hole configurations exposed to a firing overpressure of 35 bar. From left to right it shows the initial configuration, maximum displacement/crack initiation, the same point in the experiment, and the final point of the simulation. The picture from the experiment is here to aid the comparison between the numerical simulation and the experiments. Both C1 (Figure 31a) and C5-1 (Figure 31c) configurations show no indication of crack initiation, while for the C5-2 (Figure 31d) two cracks were initiated at the point of maximum displacement between the vertical holes in the outer hexagon structure. These cracks also occurred in the shock tube experiment.

The C3 (Figure 31b) simulation was the only simulation that was stopped midway. Firstly, two cracks developed in the diagonals between the upper hole and the two lower holes. Followed by two cracks that were initiated from each of the lower holes toward their respective corner. The cracks propagated for some distance before they eventually stopped, and the triangular part bent out. When the triangular part had rotated 90° out of the plane, the piece started to tear through the plate vertically. The explanation for this odd behavior is the way the pressure loading is implemented in the numerical model, since the pressure is uniformly distributed and always stays normal on the plate. Obviously, the pressure loading upon the bent-out triangle was enough to tear through the material. This was regarded as a nonphysical behavior of the simulation since the pressure in the shock tube will just flow through the hole and expand into the tank behind the plate. For this reason, the last picture in time series for C3-35 is the moment before the plate tear down vertically (see Figure 31b right). The rest of the simulation is in rather good agreement with what was observed in the experiment.

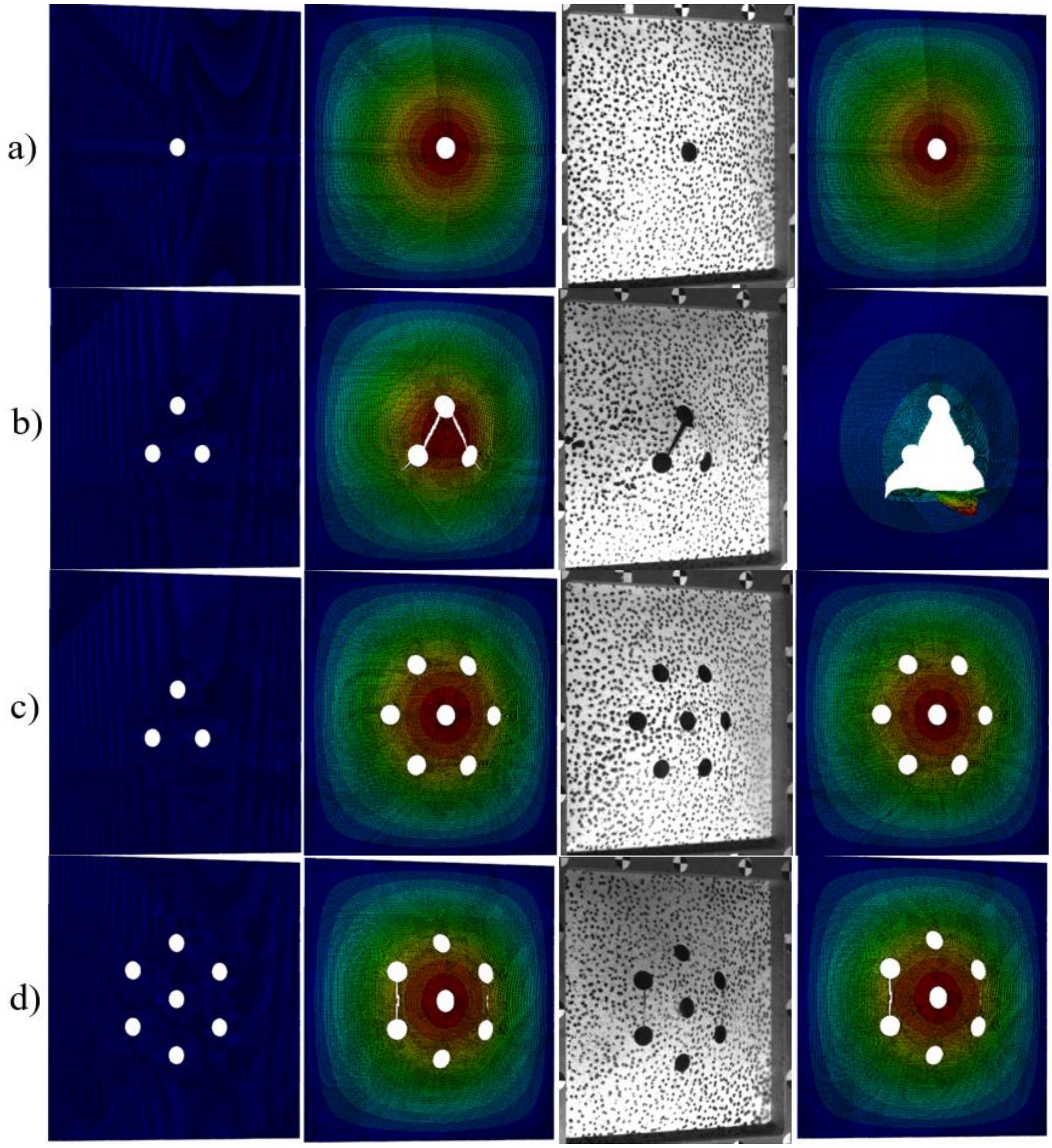

Figure 31 - show the solid models with perforated plates with circular holes exposed to firing overpressure of 35 bar. The colors indicate out of plane displacement. From left to right initial configuration (left), maximum displacement/crack initiation, experiment at maximum displacement, and final point of simulation (right). a) C1-35, b) C3-35, c) C5-1-35, and d) C5-2-35.

The results from the numerical simulations for perforated plates exposed to blast loading with firing overpressure of 60 bar are presented in Figure 32. From left to right it shows the initial configuration, after fracture initiation, the same point in their respective experiment, and developed fracture pattern. For C1 (Figure 32a) four cracks initiated in a star pattern, where each crack propagated towards its respective corner. The C1-60 simulation is different from the other simulations at this pressure level. The crack propagation stopped and the last picture in Figure 32a shows the last point of the simulation, while all the other simulations show a developed crack. The C3 (Figure 32b) test showed a deformation pattern where fracture initiated diagonally between the holes and one crack in each of the lower holes in the direction of their respective corner. After these cracks were initiated, two cracks started to propagate from the upper hole toward their corner. The triangular part was intact through the simulation which is consistent with what was observed in the experiment. For the C5-1 (Figure 32c) and C5-2 (Figure 32d) simulations, the initial behavior was quite similar. Cracks initiated in the holes closest to their respective corners. Followed by cracks between the holes that were placed in straight lines between each other horizontally for C5-1 and vertically for C5-2 respectively in the outer hexagon structure. After this the behavior deviated slightly; C5-2 formed four cracks toward holes placed diagonally with respect to the center hole, while the C5-1 formed two cracks diagonally in the direction of two holes from the center hole. This non-symmetric fracture pattern in the C5-1 is thought to be a numerical effect since the material is modelled as isotropic with symmetrical loading and boundary conditions.

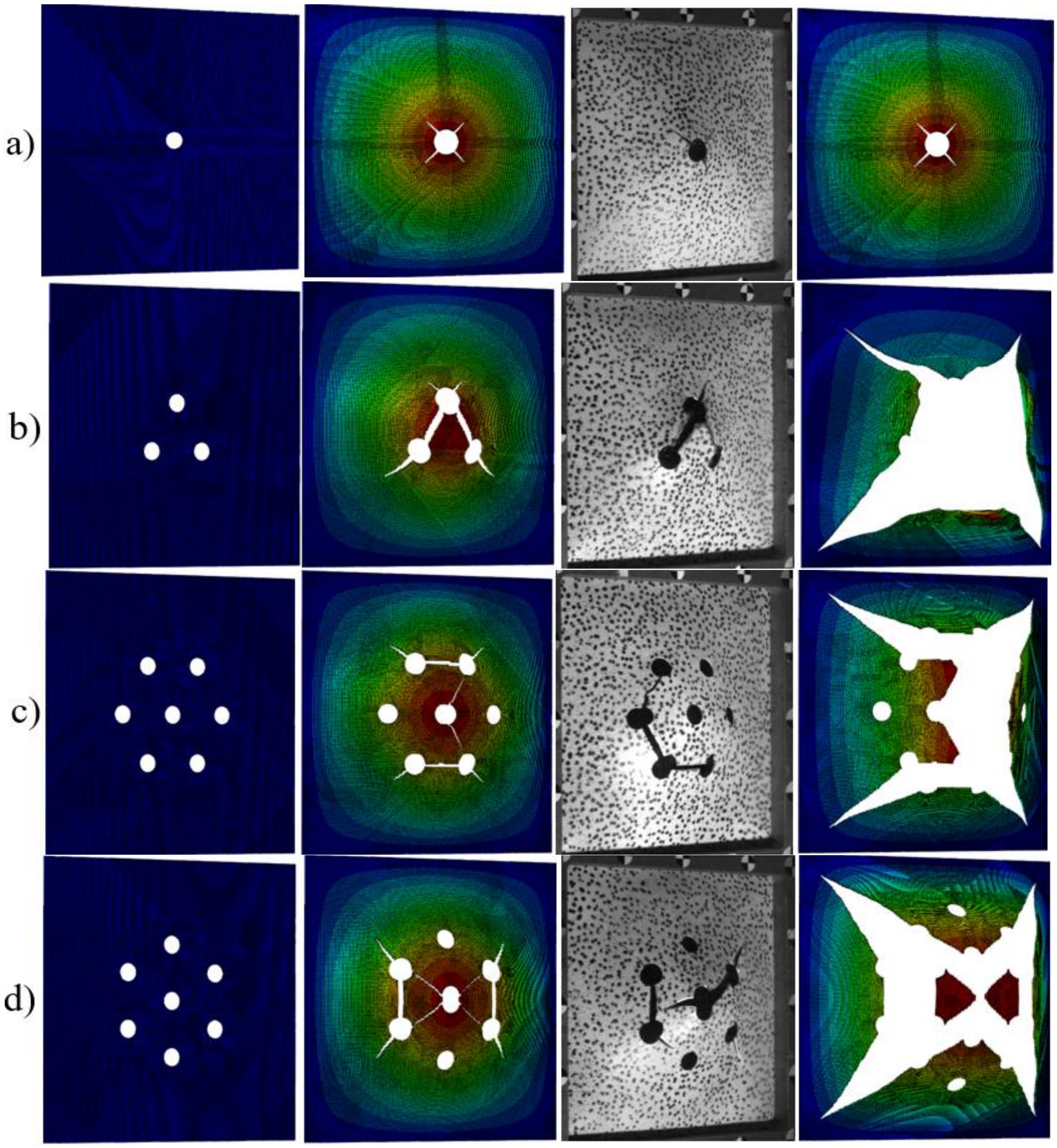

Figure 32 - show the solid models with perforated plates with circular holes exposed to firing overpressure of 60 bar. The colors indicate out of plane displacement. From left to right initial configuration (left), fracture starts, fracture starts in experiment, and developed cracks (right). a) C1-60, b) C3-60, c) C5-1-60, and d) C5-2-60.

5.4 Investigation of perforated plate response

Based on the numerical simulations of perforated plates, it was interesting to look at how the different configurations performed when exposed to blast loading. Most of the numerical simulations displayed a similar fracture and deformation pattern as observed in their corresponding shock tube experiment (see Figure 30 and Figure 31), except for C5-1-60. In the numerical model the fracture criterion is represented by the CL criterion (see Equation 4). In the CL criterion, two field variables are important for the damage accumulation, and thus the description of material failure. These are the equivalent plastic strain rate $\dot{p}$ and the major principle stress component σ_I. The product of these two parameters gives us an understanding how ductile damage accumulates in the plate due to the loading through the CL parameter W. It its therefore of interest to examine how these field variables vary through the plates during blast loading.

In Figure 33 the plastic strain rate, major principal stress, and the damage accumulation are shown for the simulations exposed to a firing overpressure of 35 bar. These are the same simulations that were shown in Figure 31. For C1 (Figure 33a) and C5-1 (Figure 33c), the deformed configuration is taken from the increment right before maximum displacement, while C3 (Figure 33b) and C5-2 (Figure 33d) the deformed configuration is taken from the increment before cracks initiation take place. For C1-35 four directions stand out as critical zones. These are the points around the perforated hole that are closest to their respective corner. The plate did not fracture at this pressure level but the field plots suggest where cracks would initiate for larger pressure. For C3-35 it seems that the plastic strains and the largest stress magnitudes localize in the diagonals between the holes. In addition, to some stress concentration in the lower holes that are directed toward their closest corner. The damage parameter W seems to be largest in the zones around the lower holes, and fracture initiates first in the region close to the lower holes and on the diagonals between the holes in the numerical simulations.

The C5-1-35 and C5-2-35 seems to have a very similar behavior. Plastic strains seem to localize along the straight lines between the holes in the outer hexagon structure of holes either horizontally (C5-1) or vertically (C5-2). The trends for the major principal stress component are similar. The product of this is that both configurations accumulate damage in the straight lines between holes in the outer hexagon. From the plots it seems that there is a more pronounced strain- and stress concentration for the C5-2 configuration than for the C5-1 configuration. This is also indicated in Figure 31 where C5-2 fractures while C5-1 does not. Another observation pertaining C5-1 and C5-2 is that $\dot{p}$ and σ_I tends to localize along the diagonals toward the outer holes from the center hole.

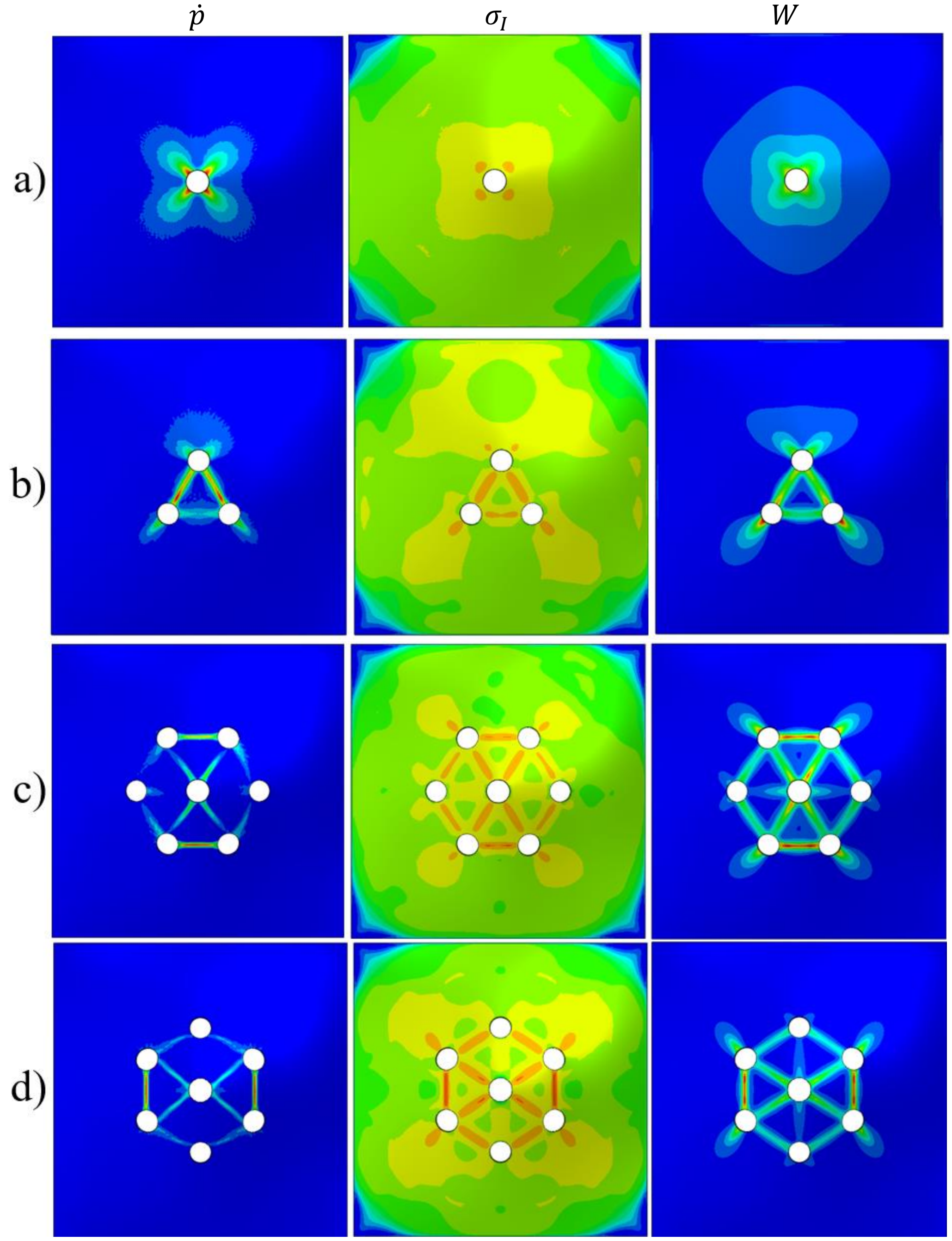

Figure 33- show the numerical simulations exposed to firing overpressure of 35 bar. From left to right $\dot{p}$, σ_I, *and the damage parameter* W. *Where the a) C1-35, b) C3-35, c) C5-1-35, and d) C5-2-35. For a) C1 and c) C5-1 the plot shows the increment right before maximum displacement, while b) C3 and d) C5-2 the plot shows the increment right before fracture occurs.*

Figure 34 shows the same plates as Figure 33, however for a firing overpressure of 60 bar. The most apparent difference is that all the plots illustrate the behavior in the increment before fracture. For C1-60 (Figure 34a) the trend is similar to the C1-35 simulation, where the localization occurs in four areas closest to their respective corner around the center hole. For C3-60 (Figure 34b) the only difference to observe is that there are larger changes in plastic strain around the lower holes. This results in fracture initiation close to the lower holes, with cracks propagating towards their respective corner, before the diagonals between the holes fracture. A similar trend is observed for

C5-1-60 (Figure 34c) and C5-2-60 (Figure 34d) where crack initiates at the holes closest to their respective corner before the straight lines, followed by fractures around the center hole.

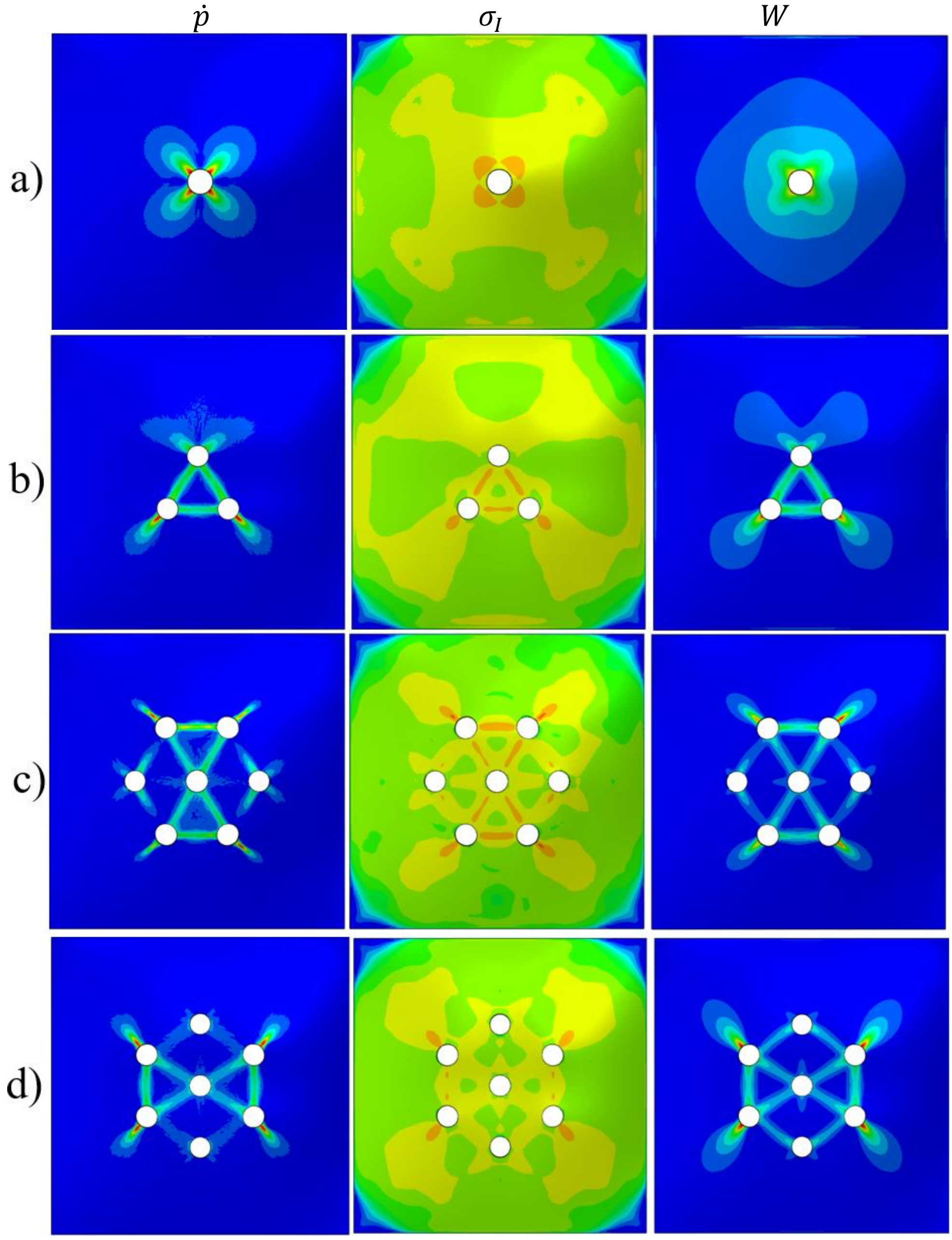

Figure 34 - show the numerical simulations exposed to firing overpressure of 60 bar. From left to right $\dot{p}$, σ_I, *and the damage parameter* W. *Where the a) C1-60, b) C3-60, c) C5-1-60, and d) C5-2-60. All plots show the increment right before fracture occurs.*

5.5 Discussion

The overall trend was that the numerical study was consistent with shock tube experiments. That is, the capacity of the perforated plates was significantly reduced compared to the full plates. Also, no fracture or collapse was observed in the numerical study of full plates.

In the study of full plates, the numerical analyses reproduced the general behavior of the aluminum plates. The maximum displacement occurs as the initial blast wave impacts the plate and withdraws to a permanent deformation and oscillates around this deformation state. Figure 30 shows the cross-section of the plates at maximum displacement for the different tests. From these results, it is apparent that the numerical analyses underestimate the maximum displacement deformation in the cross-section for D20 (Figure 30a). However, the behavior is accurately captured for D35 (Figure 30b) and D60 (Figure 30c). A possible explanation for the discrepancy in the D20 test could be the assumption that maximum displacement occurs in the center of the plate. The mesh in the 3D-DIC analysis is not symmetrically placed over the center and the cross-section data had to be shifted for this reason. This could lead to some discrepancies in comparison to the perfectly symmetric numerical analyses.

Another possible explanation could be that (i) the boundary conditions in the numerical model are too stiff, and (ii) the load applied to the plate are too large. By fixing the boundaries against any displacement and rotation, the plate cannot undergo in-plane sliding that most likely occurs in the experiment. When these simplified boundary conditions are imposed, this may underestimate the response for the plate in the simulation. Aune et al. [11] looked into this by also modelling the entire clamping assembly of the plate. The simplified conditions showed a consistent reduction in response with respect to the modelling of the complete assembly. If the load applied to the plate is too large, this may lead to a larger deformation than what is observed in the experiment. The pressure loading is considered unaffected by fluid-structure interaction. Consequently, the pressure loading may be higher in the numerical analyses than in the experiment. A combination of the simplifications in the boundary conditions and the applied loading may explain some of the discrepancies that are observed between the simulations and experiments.

In Section 5.3, the numerical simulations with perforated plates of perfect circular holes exposed to blast loading were presented. At an applied pressure of 35 bar, the C1 (Figure 31a) and C5-1 (Figure 31c) configurations showed no signs of cracks, which is in agreement with the experimental observations. For C3 (Figure 31b) the characteristic triangle from the shock tube experiment (see Figure 20b) is observed. The numerical analyses exhibit a limitation in the formulation of the blast pressure, which always stays normal to the plate. This resulted in a collapse of the plate that is unphysical. This emphasizes the importance of knowing the limits of the numerical simulations and what they are supposed to examine. Then there is C5-2 (Figure 31d) where cracks initiate in straight lines between the holes placed vertically to each other in the outer hexagon. The same observation was seen in the corresponding experiment.

The thought of anisotropy affecting the result between the C5-1-35 and C5-2-35 in the shock tube experiments was taken into consideration. Nevertheless, in the numerical models, the plates are treated as isotropic and still predict the same deformations patterns that were observed in the experiments. Since the numerical model does not account for plastic anisotropy, and still initiate cracks for C5-2 and not for C5-1, this indicates that the position of the holes affects the behavior of the plate. In Figure 33, it was observed that larger amounts of $\dot{p}$ and σ_I are localized in the C5-2-35 (Figure 33d) test than in the C5-1-35 (Figure 33c) test, which further substantiates this finding.

In the simulations with 60 bar, the C3 (Figure 33b) simulation showed the same crack initiation and propagation as in the experiment, while the other simulations showed some deviation from the experimental result. In the C1-60 (Figure 32a) simulation four cracks were initiated toward their respective corner. This deviates slightly from the experimental result where only three cracks were observed. Why only three cracks initiated in the experiment is hard to say based on a single test, therefore more tests are needed to see if this is only an experimental deviation or if it always occurs.

For the C5-2-60 (Figure 33d) the similarities between the experiment and the simulation are that cracks initiate in the holes closest to the corners. Followed by the initial cracking of the vertical lines between the holes in the outer hexagon structure, before they propagate to collapse of the plate. Consequently, the deformation pattern deviates slightly between these two events. Only two cracks develop from the center hole in the experiment, while four develop in the simulation. Figure 34d shows that the zones between the holes placed diagonally from the center hole are the critical areas where cracks could potentially initiate. So, the numerical model is in rather good agreement with the experimental results.

On the other hand, we have the C5-1-60 (Figure 32c) where the crack pattern is similar to C5-2-60 in the numerical simulation. With cracks forming at the holes closest to the corners and then along the horizontal lines, followed by two cracks that form diagonally between the center hole and surrounding holes before the total collapse occurs. This is not the fracture pattern observed in the experiment (see Figure 21c). This deviation could be a coincidence, and more experiments are needed to see if the deformation observed in the experiment is an exception or the norm for such configurations. An interesting observation from the numerical simulation is the non-symmetrical fracture pattern. From the investigation of plate response (Figure 34c), it looks like none of the diagonals from the center hole are any more critical than the others. Anyhow only two cracks form, which is thought to be a numerical effect from either slight non-symmetries in the mesh or that the FE solver rounds off a numerical value such that an asymmetric crack propagation develops.

From these results, the numerical models seem to be an adequate representation of the perforated plates exposed to blast loading. They capture the general behavior and characteristic crack patterns in most of the plates. Some simulations deviated from the experimental result in the shape of fracture patterns. The most distinct difference was observed in the simulation of C5-1-60.

An interesting observation from the experiment and numerical simulation is that the cracks form diagonally in the C3 configurations, while in the case of C5-2 both experiments and simulations (and C5-1 simulations) cracks initiate in the straight lines in the outer hexagon structure. Subsequently, diagonal fractures patterns develop around the center hole in both C5 configurations. The reason behind these different fracture patterns is thought to be dependent on the distance from the plates geometrical center. The farther away the holes are from the center, the more likely fracture is to occur in vertical or horizontal lines between holes. When holes are positioned closer toward the center of the plate, the damage seems to localize in diagonal paths between them. Figure 33 and Figure 34 confirms this as the accumulation of $\dot{p}$ and σ_I are in the diagonal for C3, where the holes are closer to the center of the plate. While for the C5 configurations (C5-1 numerically) the largest concentration of the parameters, before initial fracture, is in vertical (and horizontal) lines between the holes in the outer hexagon.

This observation could also be linked to the development of yield lines in a deformable plate. Figure 19 shows how the deformation develops for the D60 test and how plastic hinges develop as the plate deform. For the C3 configuration, the diagonals between the holes almost coincides with the yield lines developing in the diagonals for a square plate exposed to blast loading [32]. And may explain the reason for why $\dot{p}$ accumulates here in both Figure 33b and Figure 34b. In addition to the accumulation around the center hole for C1 and both C5-configurations. As the plastic hinges develop from the plate boundary the center of the plate stays planar. Consequently, this may be the reason for why cracks initiate in the outer hexagon structure for the C5 configurations where holes closest to the corners almost coincides with the diagonal yield lines. Followed by cracks in the straight lines as the plastic hinges reaches the outer hexagon structure of holes.

The shell models were discarded in the section regarding numerical simulations with perforated plates. The reason for this decision is stated in section 5.3. However, the simulations with shell elements had a much lower computational time and took around 1/10 of the time compared to the solid simulations. The findings in section 5.2 suggests that shell and solid models give identical result when the plate does not fail. This suggests it is important to have an impression about the aim of the numerical analysis. If the aim is only to investigate the global response of a plate exposed to blast loading, a model with shell elements would be a more computational effective choice compared to solid elements. The shortcomings occur when evaluating crack propagation. Since the shell formulation does not allow for a finer mesh necessary to accurately describe the crack propagation in blast loaded plates.

6 Concluding remarks

The main objective of this thesis was to investigate how perforated aluminum plates behave under blast loading and validate to which extent this can be predicted using computational tools. To investigate this a set of 2 mm thick cold-rolled aluminum plates of the type AA6082-T6 were delivered. This set consisted of full plates and plates with pre-cut holes in four different configurations, varying in the number of holes and spatial distribution. One full plate was sacrificed to produce test specimens for the uniaxial tension tests conducted to calibrate a material model for the aluminum alloy. Six other plates were also taken out of the batch to be perforated by ballistic impacts.

A simplified isotropic material model with a Voce hardening rule was made based on a comprehensive literature study into existing work on aluminum. A total number of fifteen uniaxial tension tests with different orientations to the rolled direction were conducted to evaluate the material properties. These tests showed that the AA6082-T6 material had an isotropic behavior with respect to yield stress, work hardening, and with minor spread in fracture strain. Investigations on anisotropy in the material revealed that there was a considerable anisotropy in the plastic flow. Based on these initial results the decision to move on with an isotropic material model was taken.

The material tests were used to calibrate the Voce hardening terms and the Cockcroft-Latham failure criterion. The method of adding an artificial point on the experimental data and "shoot" toward a correct solution proved to be an effective and rather efficient method. A numerical model of the uniaxial tension test used the calibrated terms as material input. By repeating the process seven times a set of feasible hardening terms was obtained. With this material model, a failure criterion was calibrated for different characteristic mesh sizes. A more extensive experimental study is needed to establish a more complete material model for the aluminum alloy. Anyhow, the 6xxx-series to aluminum is extensively researched in literature and several studies are in good agreement with one another.

The experimental study on the aluminum plates exposed to blast loading was conducted in the SIMLab Shock Tube Facility. Pressure data was logged by multiple sensors along the shock tube and the plate deformation was monitored by two high-speed cameras. The results were later post-processed with an in-house 3D-DIC software that was used to extract midpoint deformation and cross-section data from the experiments. An elaborate experimental program was conducted to obtain two firing overpressure levels, where one would be close to the capacity limit (35 bar) and one resulting in failure (60 bar).

None of the full plates showed any signs of fracture, even at the highest pressure level used in this study. Whereas the perforated plates with pre-cut holes showed cracks developing in some configurations at firing overpressure of 35 bar and all configurations collapsed at 60 bar. This showed that the pre-cut holes significantly reduced the capacity of the plate to withstand blast loading. Another interesting observation was that none of the four configurations had an identical failure pattern in the experiments. For plates with multiple holes, cracks were observed to propagated between holes, but all plates that failed during experiments showed that cracks in the end propagated toward the corners of the clamped boundary. For the plates perforated by ballistic impacts the reduction in capacity was even more significant. Both plates perforated by either a blunt or an ogival projectile nose collapsed at 35 bar and the pressure intensity had to be lowered to 20 bar to find the capacity limit.

Purely Lagrangian simulations were used in numerical studies on the blast-loaded plates. First, simulations with full plates were conducted and showed good agreement with the experimental results. This gave confidence in the simplified material model used in this thesis. Secondly, the perforated plates were simulated. For the simulations with firing overpressure at 35 bar, all the simulations showed similar behavior to that of the experiments. While at 60 bar some deviations were observed in two of the models with respect to their experimental observations. But only one of them showed a different failure pattern. As most of the numerical simulations reproduced the fracture patterns observed in the experiment. A final study investigating the developing damage and its field parameters where conducted and gave insight into how the plates responded to the blast loading.

The most uplifting result from the numerical study was the model's capability to reproduce the fracture patterns observed in the shock tube experiments. Only one simulation deviated from its experimental results. Especially interesting were the models containing seven holes, where cracks initiated between holes in both experiments and simulations. The introduction of circular pre-cut holes does not introduce any sharp corners where stresses can localize. Consequently, the initial response of perforated plates is similar to that of plates without holes. Only when the deformation reaches the holes there seem to be a tendency for damage to localize in the direction of the closest corner in that hole. Where one hole shares the same distance to multiple corners the same number of localizations governing damage occur in that hole. This formation of localization is rather coinciding with dynamic yield line theory for square plates, where yield lines develop from the clamped boundaries and travel along the plates diagonals.

It is therefore concluded that the most important findings obtained through the work in this thesis are as follows:

- Plates of AA6082-T6 aluminum with perforated holes show less capacity in resisting blast loading compared to plates without holes.
- Plates with pre-cut holes show more capacity to resist blast loading then plates perforated by ballistic impacts, because of cracks initiating in the plate due to damage caused in the plate during the ballistic impact.
- Plugging was the failure phenomena caused by blunt projectiles and produced a clean cut in the plates with minor cracks around the perforated hole. For ogival projectiles the failure phenomena observed was petaling, which initiated larger cracks in the plates.
- The numerical simulations were able to predict the general behavior and most characteristic fracture patterns that were observed in the experiments.
- The simplified material model and fracture criterion calibrated for the numerical analysis seems to be a good representation of the plate behavior.

- The capacity of perforated plates appears to be dependent on both the number of holes and their spatial distribution. When fractures occur in the plate, the crack pattern is largely dominated by the position of the holes. Cracks initiate in holes closest to their respective corner. If a hole is positioned with equal distance to multiple corners, the same number of cracks seem to initiate in that hole. In configurations with multiple holes, fractures between holes tend to be dependent on the position of the holes with respect to the plates geometrical center. If the holes are placed around the center, the cracks initiate between holes placed diagonally to each other. While the further away the holes are positioned from the center, cracks initiate vertically or horizontally between holes.

7 Further work

This section covers the suggestions for further work that could be interesting for further investigations into the performance of perforated aluminum plates exposed to blast loading.

In this thesis the AA6082-T6 was assumed to be isotropic, however, the material tests indicate that there are some anisotropy in the plastic flow. Therefore, an anisotropic material model should be considered to better capture the material behavior of the rolled aluminum plate. Moreover, this thesis was limited to a von Mises yield surface. For f.c.c materials, like aluminum, experimental results show that the yield surface lies somewhere in between the Tresca and von Mises yield criterion [33]. Investigations on the effect of yield surface should, therefore, be considered in future simulations of the blast loaded plates.

The results from the experimental and numerical study showed that the number of circular holes and their position had a significant effect on the capacity and fracture pattern of the plates. For further understanding of the perforated aluminum plate the following parametric studies are suggested:

- Changing the geometry of the perforated circular holes.
- Changing the thickness of the rolled plates.
- More pre-cut configurations with circular holes to substantiate the finding that cracks form diagonally when holes are placed close to the center and vertically, or horizontally, as one moves further from the center.
- A similar investigation on 2 mm plates with other aluminum alloys should also be considered.

If more computer resources are available, it should also be considered to increase the number of elements over the thickness of the plate.

Simulations with a complete thermo-viscoplastic constitutive relation, as shown in Equation 1 with material parameters taken from the literature (see Table 9), were also conducted with adiabatic heating included. The results from this investigation are shown in “Appendix: Perforated configurations - modified Johnson-Cook”, showing less predictability than the simplified model used in this thesis. A study investigating why this is the case is suggested.

Lastly, since this thesis was limited to a purely Lagrangian approach in the numerical simulations. An investigation into the FSI effects on deformable aluminum plates with perforated circular holes are suggested. To give a deeper understanding of how the blast load responds to the plate deformation.

8 References

[1] C. A. and M. R. Hannah Ritchie, Joe Hasell, "Terrorism - Our World in Data," *OurWorldInData.org*, 2013. [Online]. Available: https://ourworldindata.org/terrorism. [Accessed: 04-Jun-2020].

[2] Hydro, "Remelting and recycling." [Online]. Available: https://www.hydro.com/en-NO/products-and-services/services/remelting-and-recycling/. [Accessed: 20-May-2020].

[3] V. Aune, E. Fagerholt, M. Langseth, and T. Børvik, "A shock tube facility to generate blast loading on structures," *Int. J. Prot. Struct.*, vol. 7, no. 3, pp. 340–366, 2016, doi: 10.1177/2041419616666236.

[4] M. Stoffel, R. Schmidt, and D. Weichert, "Shock wave-loaded plates," *Int. J. Solids Struct.*, vol. 38, no. 42–43, pp. 7659–7680, Sep. 2001, doi: 10.1016/S0020-7683(01)00038-5.

[5] M. Colombo, M. Di Prisco, and P. Martinelli, "A New Shock Tube Facility for Tunnel Safety," doi: 10.1007/s11340-010-9430-7.

[6] H. Granum, V. Aune, T. Børvik, and O. S. Hopperstad, "Effect of heat-treatment on the structural response of blast-loaded aluminium plates with pre-cut slits," *Int. J. Impact Eng.*, vol. 132, no. May, 2019, doi: 10.1016/j.ijimpeng.2019.05.020.

[7] "NTNU Open: An Experimental and Numerical Investigation of the Blast Response of Pre-damaged Aluminium Plates." [Online]. Available: https://ntnuopen.ntnu.no/ntnu-xmlui/handle/11250/2614883. [Accessed: 21-May-2020].

[8] S. Li, X. Li, Z. Wang, G. Wu, G. Lu, and L. Zhao, "Sandwich panels with layered graded aluminum honeycomb cores under blast loading," *Compos. Struct.*, vol. 173, pp. 242–254, Aug. 2017, doi: 10.1016/j.compstruct.2017.04.037.

[9] K. G. Rakvåg, N. J. Underwood, G. K. Schleyer, T. Børvik, and O. S. Hopperstad, "Transient pressure loading of clamped metallic plates with pre-formed holes," *Int. J. Impact Eng.*, vol. 53, pp. 44–55, Mar. 2013, doi: 10.1016/j.ijimpeng.2012.07.013.

[10] H. M. Granum and L. M. Løken, "Experimental and numerical study on perforated steel plates subjected to blast loading," no. June, 2016.

[11] V. Aune, G. Valsamos, F. Casadei, M. Langseth, and T. Børvik, "On the dynamic response of blast-loaded steel plates with and without pre-formed holes," *Int. J. Impact Eng.*, vol. 108, pp. 27–46, 2017, doi: 10.1016/j.ijimpeng.2017.04.001.

[12] O. Hopperstad and Tore Børvik, "Materials Mechanics 1," 2017.

[13] O. Hopperstad and Tore Børvik, "Materials Mechanics 2," 2017.

[14] Y. Chen, A. H. Clausen, O. S. Hopperstad, and M. Langseth, "Application of a split-Hopkinson tension bar in a mutual assessment of experimental tests and numerical predictions," *Int. J. Impact Eng.*, vol. 38, no. 10, pp. 824–836, Oct. 2011, doi: 10.1016/j.ijimpeng.2011.05.002.

[15] V. Vilamosa, A. H. Clausen, T. Børvik, S. R. Skjervold, and O. S. Hopperstad, "Behaviour of Al-Mg-Si alloys at a wide range of temperatures and strain rates," *Int. J. Impact Eng.*, vol. 86, pp. 223–239, Dec. 2015, doi: 10.1016/j.ijimpeng.2015.08.008.

[16] C. Baglo and T. M. Dybvik, "Experimental and Numerical Study on Plated Structures Subjected to Blast Loading," 2015.

[17] M. G. Cockcroft and D. . Latham, "Ductility and the Workability of metals," *J. Inst. Met.*, p. 400, 1968.

[18] J. K. Holmen, T. Børvik, O. R. Myhr, H. G. Fjær, and O. S. Hopperstad, "Perforation of welded aluminum components: Microstructure-based modeling and experimental

validation," *Int. J. Impact Eng.*, vol. 84, pp. 96–107, 2015, doi: 10.1016/j.ijimpeng.2015.05.016.

[19] D. Morin, B. L. Kaarstad, B. Skajaa, O. S. Hopperstad, and M. Langseth, "Testing and modelling of stiffened aluminium panels subjected to quasi-static and low-velocity impact loading," *Int. J. Impact Eng.*, vol. 110, pp. 97–111, 2017, doi: 10.1016/j.ijimpeng.2017.03.002.

[20] "MathWorks - Makers of MATLAB and Simulink - MATLAB & Simulink." [Online]. Available: https://se.mathworks.com/?s_tid=gn_logo. [Accessed: 23-May-2020].

[21] E. Fagerholt, "Make and Run 3D-DIC Input File — eCorr Digital Image Correlation 4.0 documentation." [Online]. Available: http://folk.ntnu.no/egilf/ecorr/doc/3ddic/makeinput3d.html. [Accessed: 25-May-2020].

[22] M. E. Babeshko and Y. N. Shevchenko, "Plastic incompressibility of anisotropic material," *Prikl. Mekhanika*, vol. 41, no. 3, pp. 38–45, 2005.

[23] T. Tryland, O. S. Hopperstad, and M. Langseth, "Design of experiments to identify material properties," *Mater. Des.*, vol. 21, no. 5, pp. 477–492, 2000, doi: 10.1016/s0261-3069(00)00035-2.

[24] E. Fagerholt, "eCorr v4.0 Documentation — eCorr Digital Image Correlation 4.0 documentation," May-. [Online]. Available: http://folk.ntnu.no/egilf/ecorr/doc/. [Accessed: 05-May-2020].

[25] M. Rodríguez-Millán, · A Vaz-Romero, · A Rusinek, J. A. Rodríguez-Martínez, · A Arias, and A. Rusinek, "Experimental Study on the Perforation Process of 5754-H111 and 6082-T6 Aluminium Plates Subjected to Normal Impact by Conical, Hemispherical and Blunt Projectiles," *Exp. Mech.*, vol. 54, pp. 729–742, 2014, doi: 10.1007/s11340-013-9829-z.

[26] S. Dey, T. Børvik, O. S. Hopperstad, J. R. Leinum, and M. Langseth, "The effect of target strength on the perforation of steel plates using three different projectile nose shapes," in *International Journal of Impact Engineering*, 2004, vol. 30, no. 8–9, pp. 1005–1038, doi: 10.1016/j.ijimpeng.2004.06.004.

[27] T. Børvik, O. S. Hopperstad, and M. Langseth, "Lecture Notes in TKT4128 Impact Mechanics : An Introduction to Penetration and Perforation Mechanics," no. September, pp. 1–87, 2017.

[28] V. Aune, T. Børvik, and M. Langseth, "Lecture Notes in TKT4128 Impact Mechanics : An Introduction to blast Mechanics," no. September, pp. 1–87, 2019.

[29] T. Børvik and O. S. Hopperstad, "Lecture Notes Impact Mechanics – Part 1: Modelling of plasticity and failure with explicit finite element methods," pp. 1–68, 2018.

[30] A. A. Benzerga and J. B. Leblond, *Ductile Fracture by Void Growth to Coalescence*, vol. 44. Elsevier, 2010.

[31] W. Lan *et al.*, "Study of slant fracture in ductile materials," *Int J Fract*, vol. 141, pp. 469–496, 2006, doi: 10.1007/s10704-006-9008-7.

[32] N. Jones, *Structural Impact.* Cambridge University Press, 2012.

[33] W. F. Hosford, "A Generalized Isotropic Yield Criterion," 1972.

9 Appendix

9.1 Appendix: Material testing and calibration

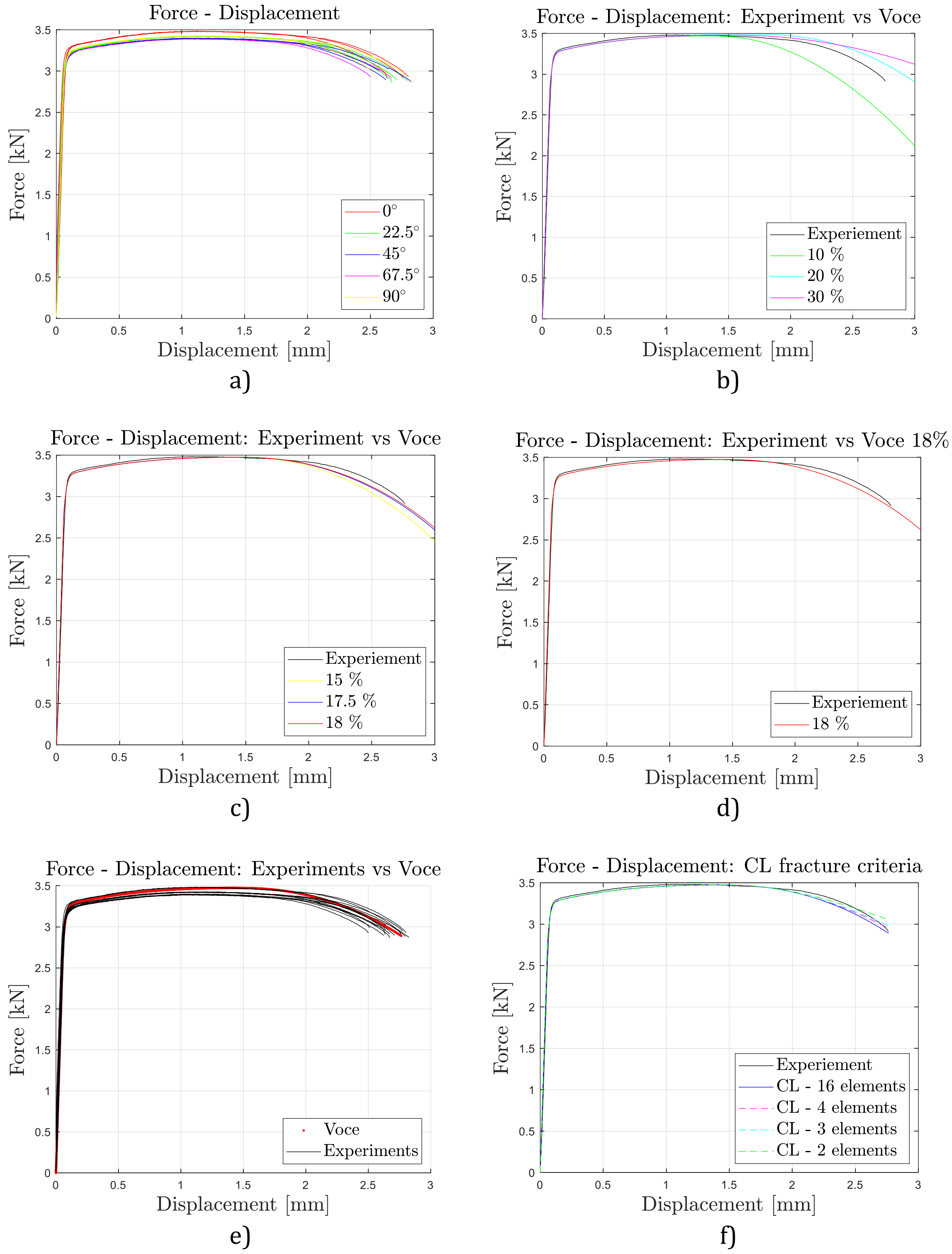

Figure 35 - show force-displacement curves for all engineering stress-strain curve presented in chapter 3.

9.2 Appendix: Shock tube

9.2.1 Appendix: Pressure measurement

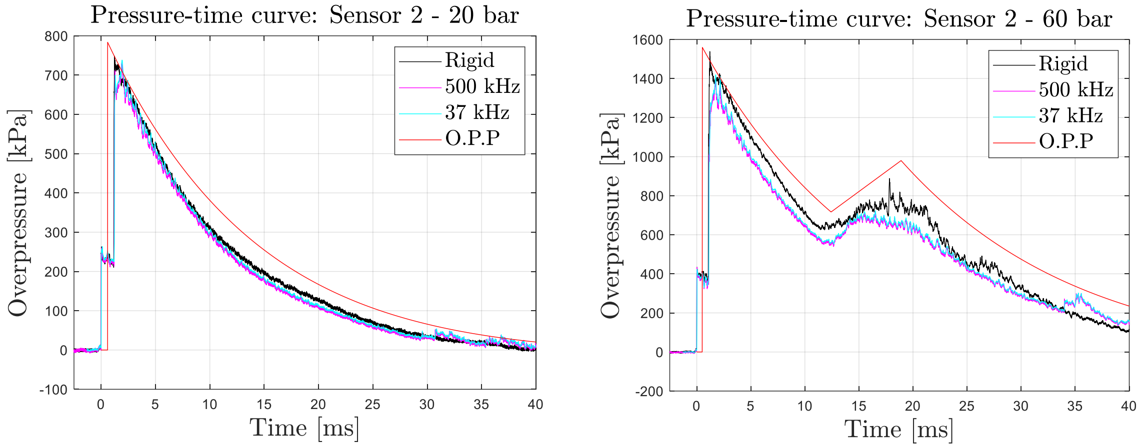

a) b)

Figure 36 - a) Test D20. B) Test D60. Figure shows pressure-time curves for Sensor 2 with sampling frequency 37 kHz (cyan), and 500 kHz (magenta) plotted against the pressure-time data from the experiment (black) used to calibrate the on plate pressure curve (red) in Ref. [3].

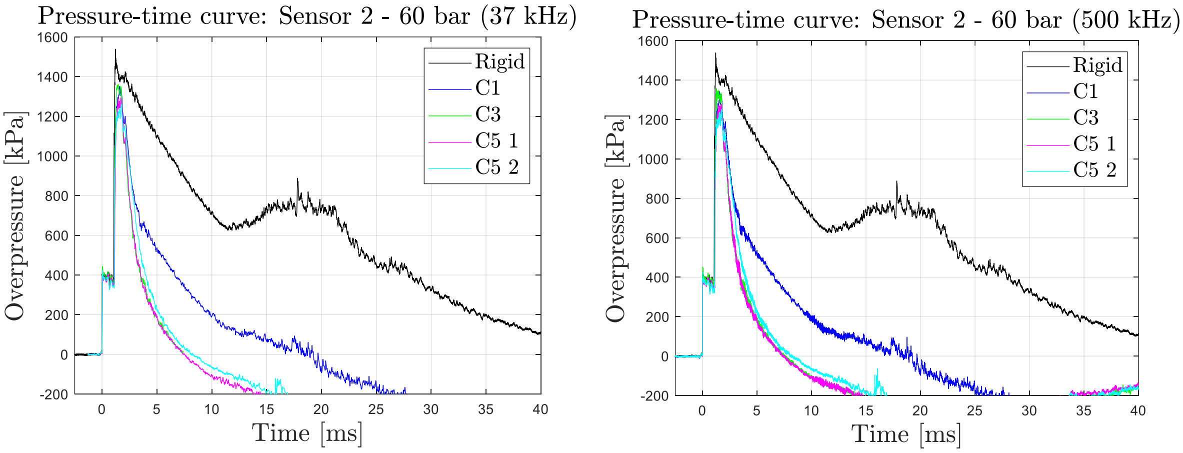

a) b)

Figure 37 - a) shows the pressure-time curve for the holed configurations with a sampling rate of 37 kHz compared to the curve from the experiment used for calibrating the on-plate pressure for a firing overpressure of 60 bar. b) shows the pressure-time curve for the holed configurations with a sampling rate of 500 kHz compared to the curve from the experiment used for calibrating the on-plate pressure in Ref. [3], a firing overpressure of 60 bar. Rigid (black), holed configuration C1 (blue), C3 (green), C5-1 (magenta), and C5-2(cyan).

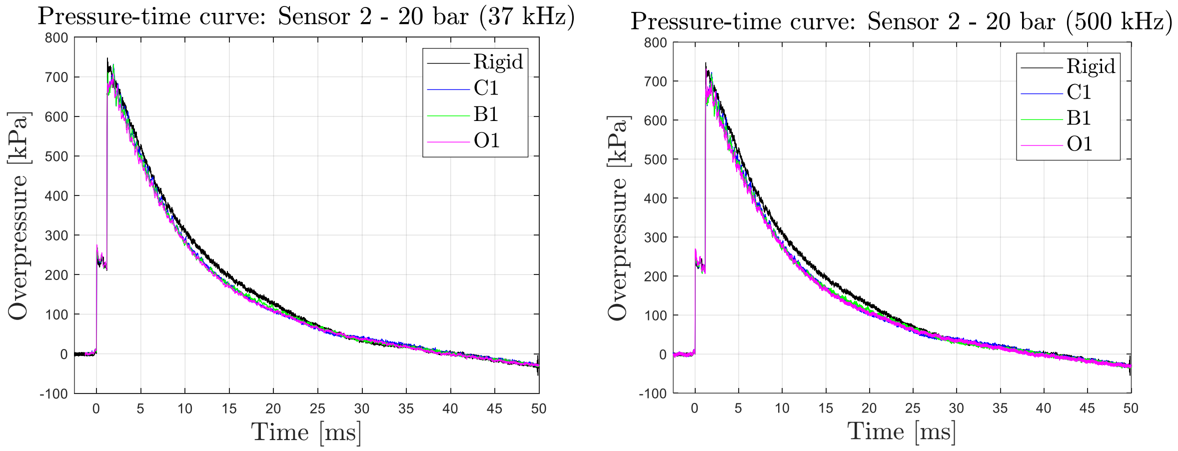

a) b)

Figure 38 - a) shows the pressure-time curve for the perforated configurations with a sampling rate of 37 kHz compared to the curve from the experiment used for calibrating the on-plate pressure for a firing overpressure of 20 bar. b) shows the pressure-time curve for the perforated configurations with a sampling rate of 500 kHz compared to the curve from the experiment used for calibrating the on-plate pressure in Ref. [3], a firing overpressure of 20 bar. Rigid (black), holed configuration C1 (blue), C3 (green), C5-1 (magenta), and C5-2(cyan).

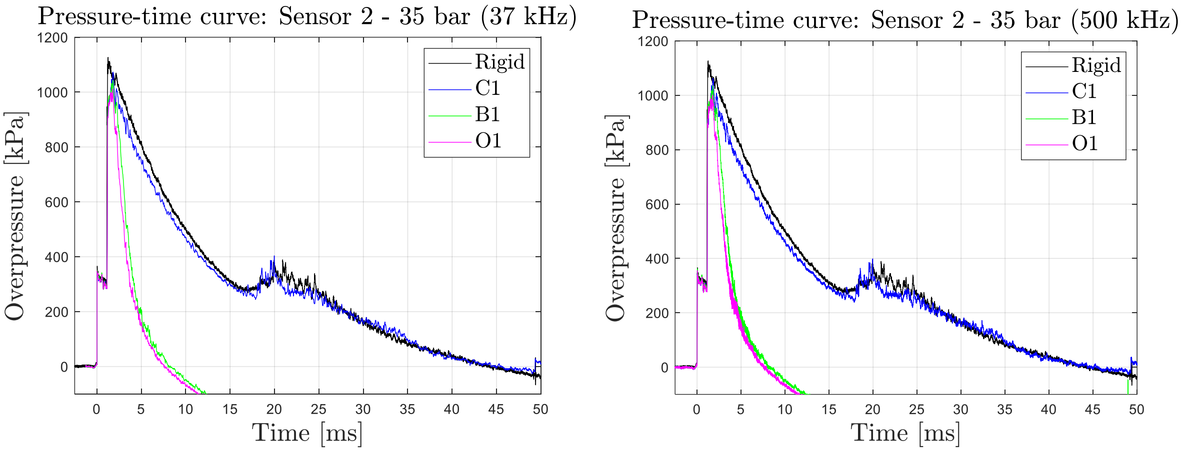

a) b)

Figure 39 - a) shows the pressure-time curve for the perforated configurations with a sampling rate of 37 kHz compared to the curve from the experiment used for calibrating the on-plate pressure for a firing overpressure of 35 bar. b) shows the pressure-time curve for the perforated configurations with a sampling rate of 500 kHz compared to the curve from the experiment used for calibrating the on-plate pressure in Ref. [3], a firing overpressure of 35 bar. Rigid (black), holed configuration C1 (blue), C3 (green), C5-1 (magenta), and C5-2(cyan).

9.2.2 Appendix: Full plate

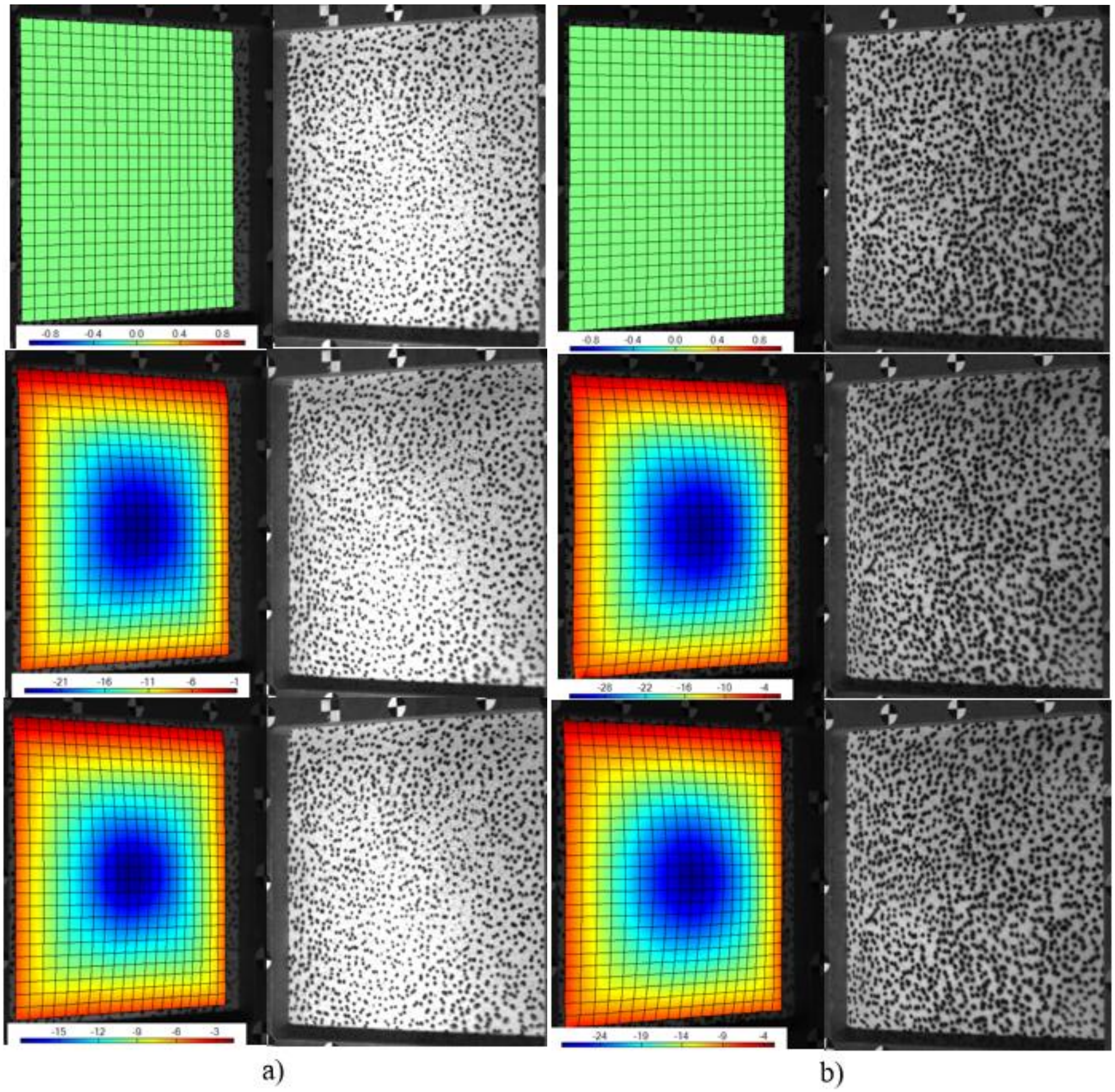

Figure 40 - a) left) shows the D20 test in eCorr viewed from camera 1 with an out of plane displacement field, right) shows the D20 test viewed from camera 2. b) left) shows the D35 test in eCorr viewed from camera 1 with an out of plane displacement field, right) shows the D35 test viewed from camera 2. The colorbar shows displacement in mm.

9.3 Appendix: Numerical study

9.3.1 Appendix: Perforated configurations – shell model

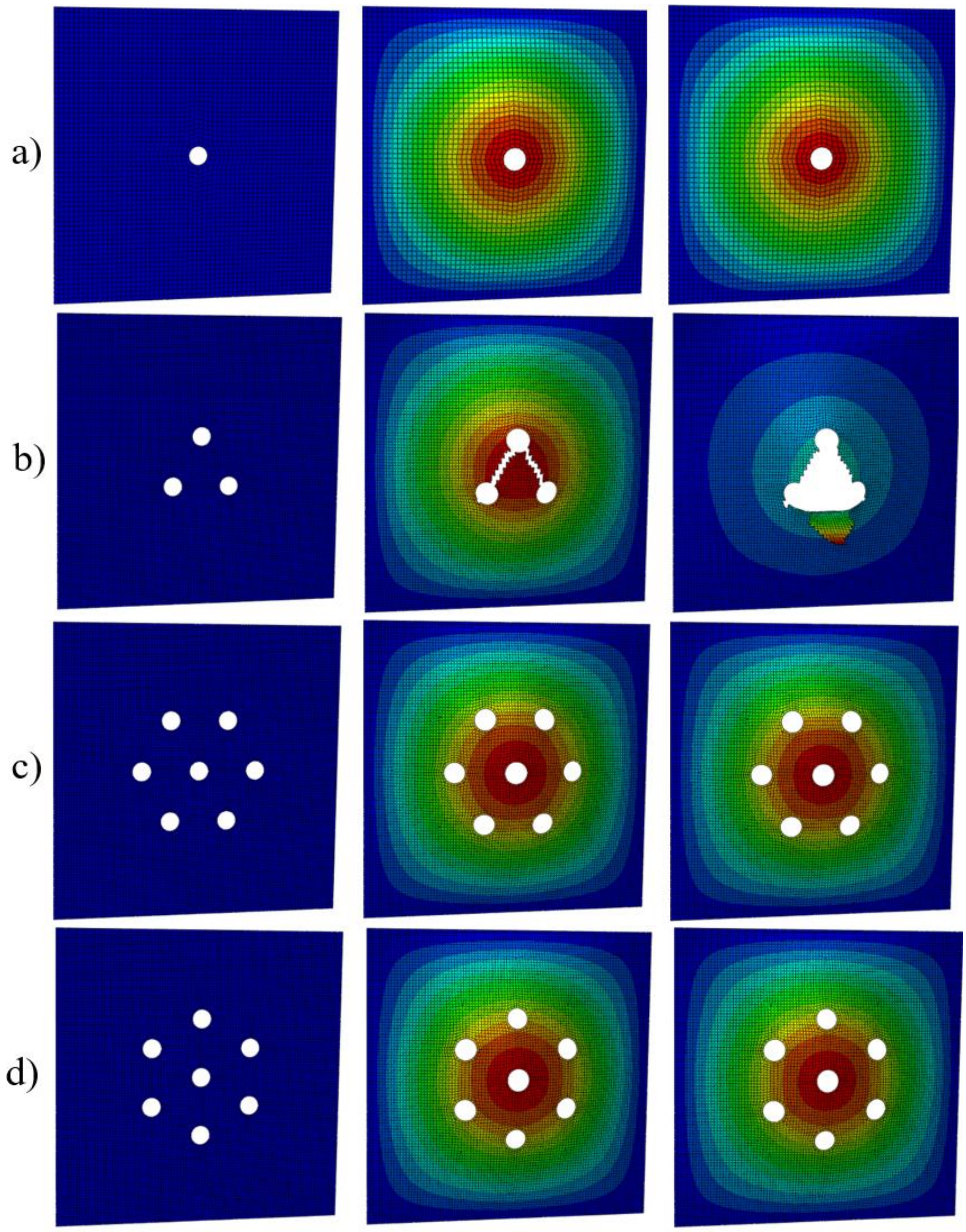

Figure 41 - show the shell models with perforated plates with circular holes exposed to firing overpressure of 35 bar. The colors indicate out of plane displacement. From left to right initial configuration (left), maximum displacement, and final point of simulation (right). a) C1-35, b) C3-35, c) C5-1-35, and d) C5-2-35.

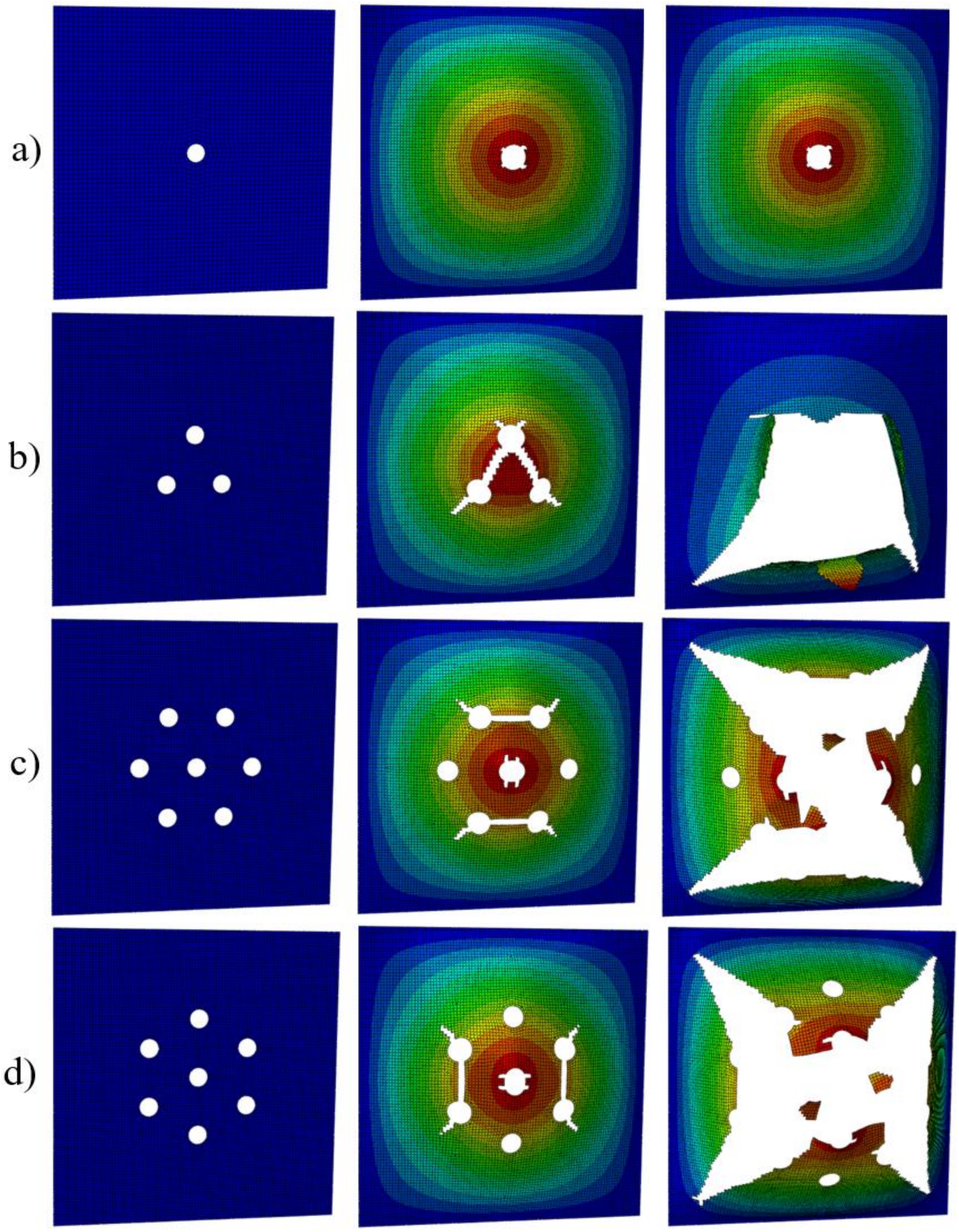

Figure 42 - show the shell models with perforated plates with circular holes exposed to firing overpressure of 60 bar. The colors indicate out of plane displacement. From left to right initial configuration (left), fracture started , and developed cracks (right). a) C1-60, b) C3-60, c) C5-1-60, and d) C5-2-60.

9.3.2 Appendix: Perforated configurations - modified Johnson-Cook

Table 9 - Material constants for a complete modified Johnson-Cook taken from literature.

E [GPa]	ν [-]	ρ [kg/m^3]	$\dot{p}_0$ [s^{-1}]	c [-]	T_r [K]	T_m [K]	m [-]	c_p [J/kgK]	χ [-]
70	0.3	2700	0.0005	0.001	293	923	1.0	910	0.9

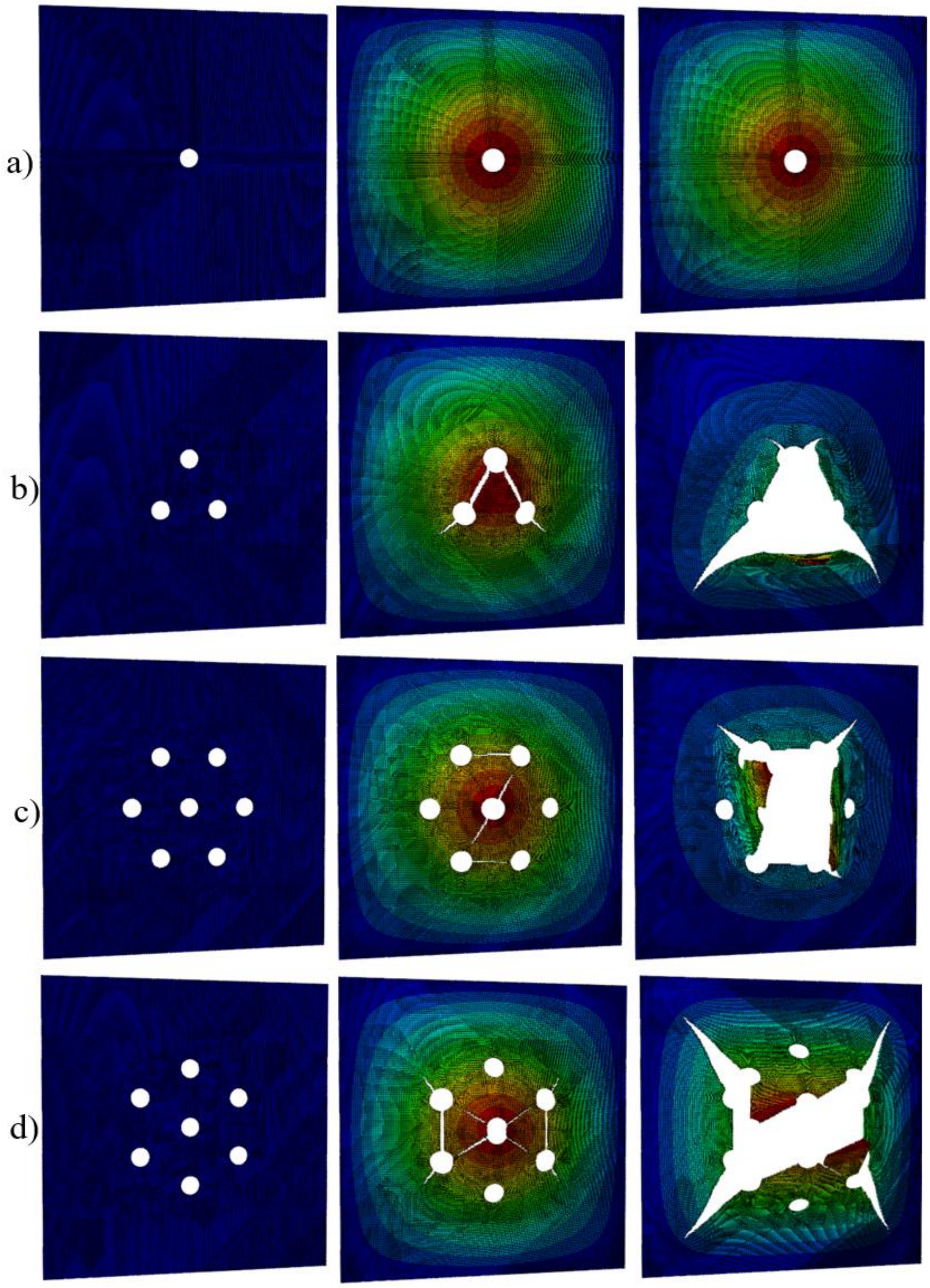

Figure 43 - show the solid models, with full modified Johnson-Cook constitutive relation, perforated plates with circular holes exposed to firing overpressure of 35 bar. The colors indicate out of plane displacement. From left to right initial configuration (left), maximum displacement, experiment at maximum displacement, and final point of simulation (right). a) C1-35, b) C3-35, c) C5-1-35, and d) C5-2-35.

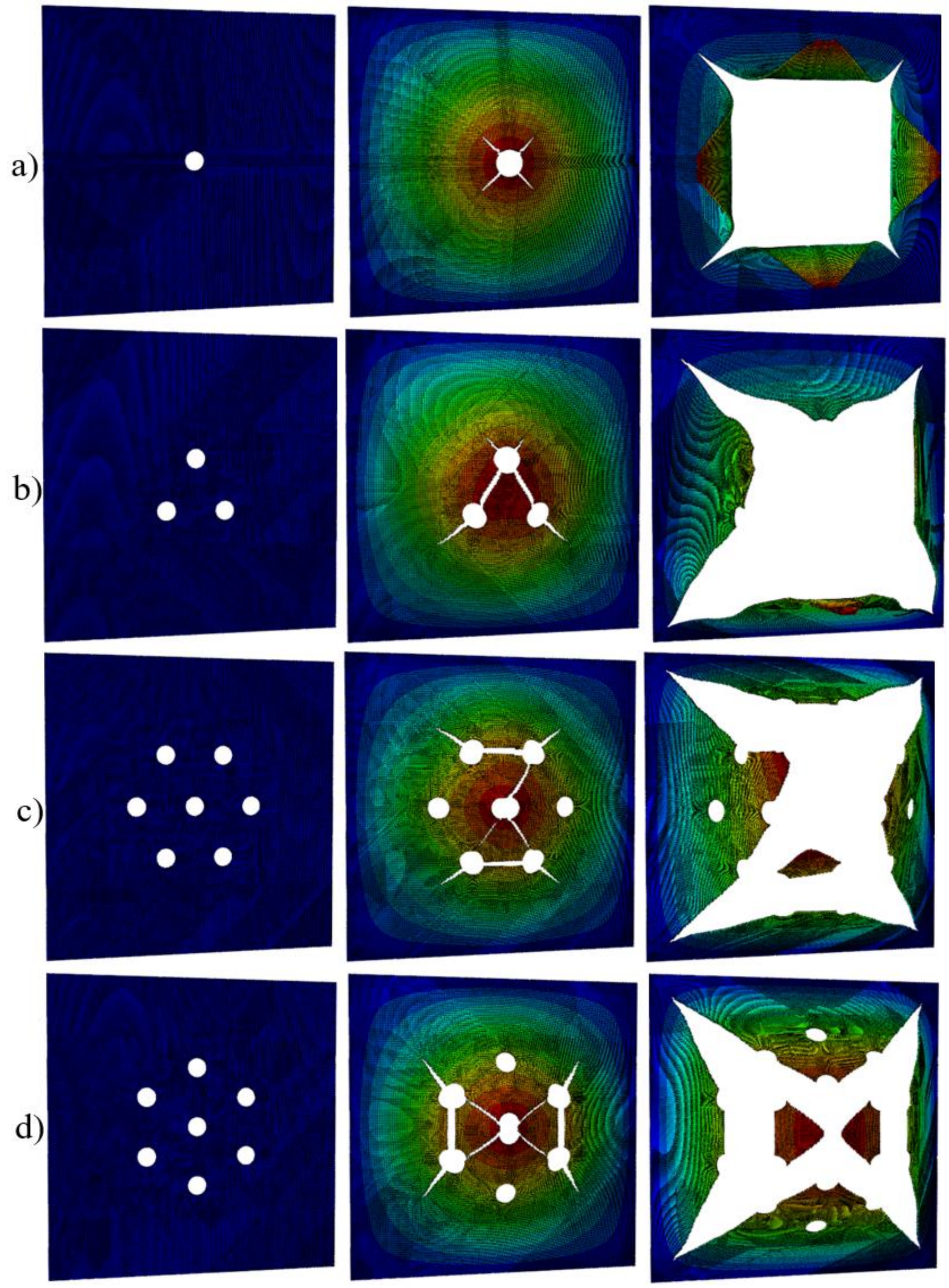

Figure 44 - show the solid models, with full modified Johnson-Cook constitutive relation, perforated plates with circular holes exposed to firing overpressure of 60 bar. The colors indicate out of plane displacement. From left to right initial configuration (left), maximum displacement, experiment at maximum displacement, and final point of simulation (right). a) C1-60, b) C3-60, c) C5-1-60, and d) C5-2-60.

9.3.3 Appendix: Investigation of plate response - modified Johnson-Cock

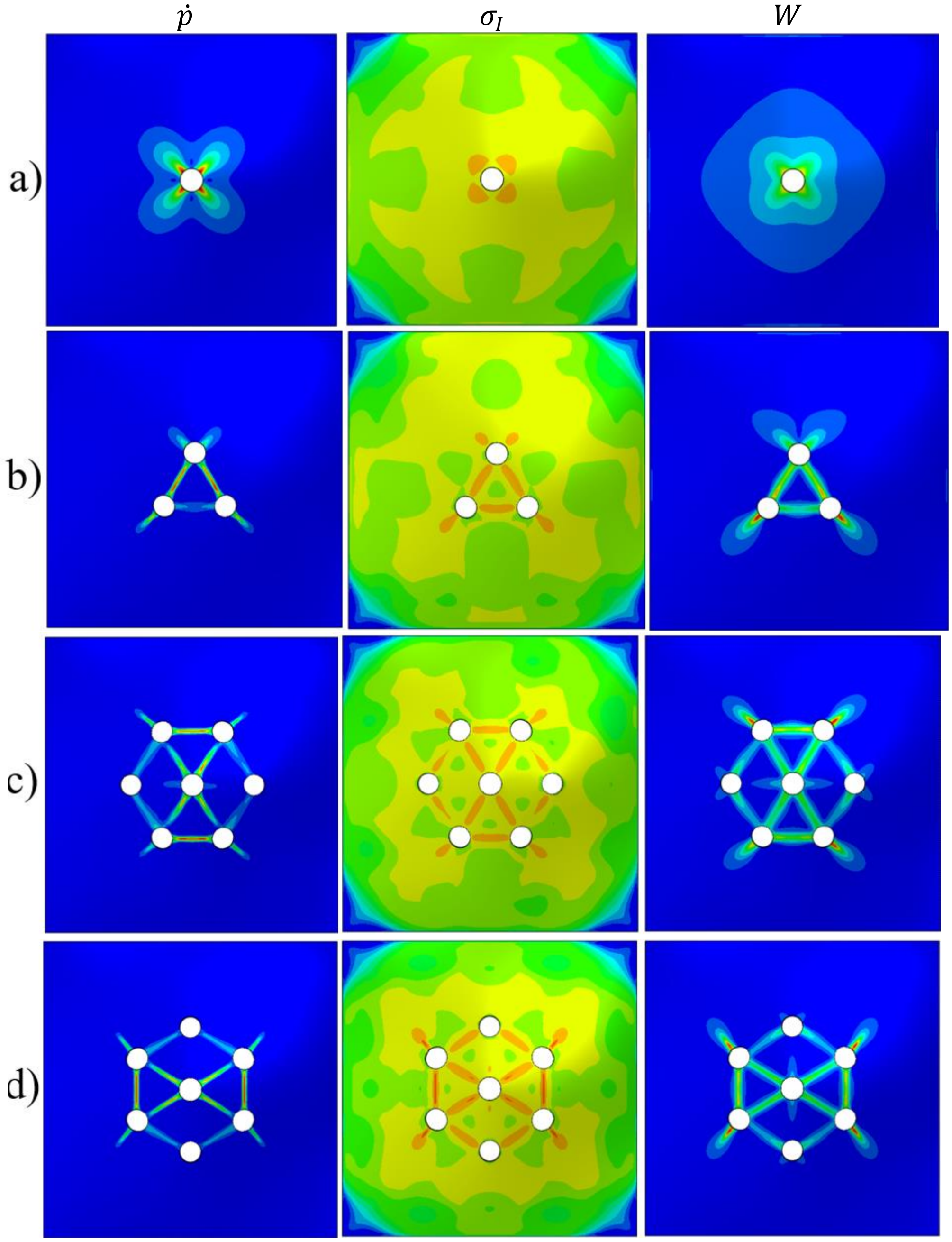

Figure 45 - show the numerical simulations, with full modified Johnson-Cook constitutive relation, exposed to firing overpressure of 35 bar. From left to right $\dot{p}$, σ_I, and the damage parameter W. Where the a) C1-35, b) C3-35, c) C5-1-35, and d) C5-2-35. For a) C1 the plot shows the increment right before maximum displacement, while b) C3, c) C5-1, and d) C5-2 the plot shows the increment right before fracture occur.

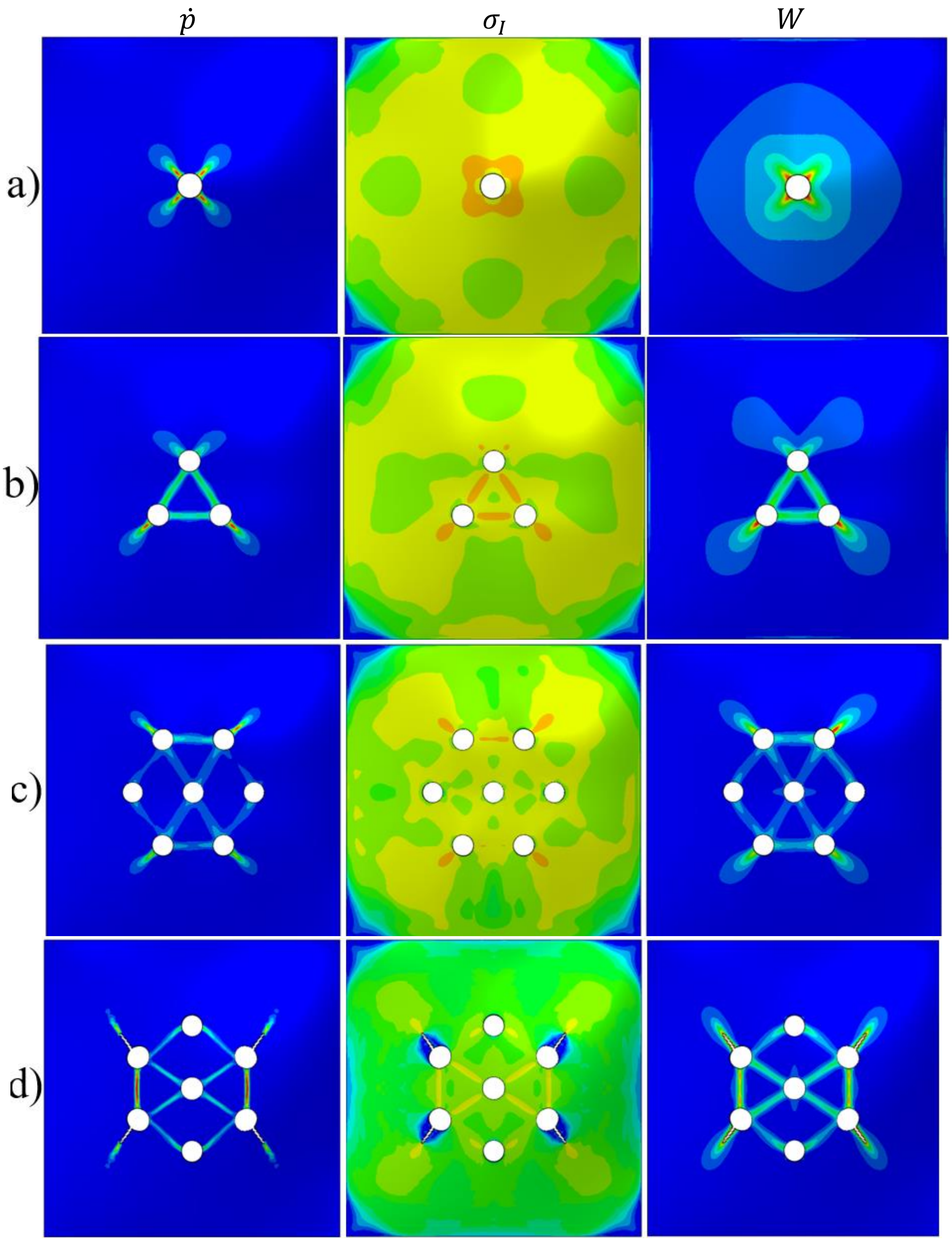

Figure 46 - show the numerical simulations, with full modified Johnson-Cook constitutive relation, exposed to firing overpressure of 60 bar. From left to right $\dot{p}$, σ_I, *and the damage parameter* W. *Where the a) C1-60, b) C3-60, c) C5-1-60, and d) C5-2-60. All plots show the increment right before fracture occur.*

NTNU

Norwegian University of
Science and Technology